DISCRETE ELEMENT METHOD SIMULATION OF WEAR DUE TO SOIL-TOOL INTERACTION

A Thesis Submitted to the College of

Graduate Studies and Research

In Partial Fulfillment of the Requirements

For the Degree of Master of Science

In the Department of Agricultural and Bioresource Engineering

University of Saskatchewan

Saskatoon

By

LYNDON GRAFF

© Copyright Lyndon Graff, 2010. All rights reserved.

Permission to Use

In presenting this thesis in partial fulfilment of the requirements for a Postgraduate degree from the University of Saskatchewan, I agree that the Libraries of this University may make it freely available for inspection. I further agree that permission for copying of this thesis in any manner, in whole or in part, for scholarly purposes may be granted by the professor or professors who supervised my thesis work or, in their absence, by the Head of the Department or the Dean of the College in which my thesis work was done. It is understood that any copying or publication or use of this thesis or parts thereof for financial gain shall not be allowed without my written permission. It is also understood that due recognition shall be given to me and to the University of Saskatchewan in any scholarly use which may be made of any material in my thesis.

Requests for permission to copy or to make other use of material in this thesis in whole or part should be addressed to:

Head of the Department of Agricultural and Bioresource Engineering
University of Saskatchewan
Saskatoon, Saskatchewan S7N 5A9

ABSTRACT

This study considered using a relatively new method to study soil-tool wear which could drastically reduce the time and associated costs of traditional wear studies. The goal was to utilize discrete element method (DEM) simulations to recreate the results of a circular soil bin test in order to develop a relationship that could be used to predict wear under different conditions. Through the application of DEM, simulations could be used to study different materials or designs intended to result in improved wear performance.

Three replications of aluminum cylindrical bars were worn during 400 km of travel in a circular soil bin. Wear was quantified by measuring the change in radius of the cylinders at 18-degree intervals around their circumference. Mass data were also obtained to provide an overall average of wear occurring on the bar and to validate the radii measurements.

The DEM simulations were executed using EDEM software. Conditions present in the physical soil bin trials were simulated by recreating components in the soil bin and incorporating soil properties that were directly measured, using representative soil samples. Forces exerted on the bar by the soil and the relative velocities between the soil and tool were used to generate a relationship to predict wear of the bar. The wear equation was verified using a portion of the experimental data from the soil bin.

The wear model showed promise in predicting the amount of wear recorded in the soil bin through the application of DEM-predicted compressive forces and relative velocities between the tool and soil particles. The Archard equation for wear was modified to create a non-linear equation. Plotting the measured wear against the wear predicted from the fitted equation produced a trendline with a slope of 0.65. Although a

perfect correlation would have produced a slope of 1, the model was able to predict a large portion of the wear that occurred. Refinement of the model could further be achieved with changes in the design of the geometry used in the simulation and through verification of force predictions with experimental data. Because of the variable nature of wear, additional replications of tools in the soil bin would have increased the number of data points available to create the model and reduced the impact of outlying data. With these recommended improvements, the wear model has the ability to very accurately predict the wear of a cylindrical bar.

ACKNOWLEDGEMENTS

I wish to sincerely acknowledge Dr. Trever Crowe, my supervisor, for his guidance and direction in this project. I would also like to acknowledge my industry advisor, Dr. Martin Roberge, for giving me the opportunity to work on this project and for his endless support. Similarly, I would like to thank the third member of my Graduate Advisory Committee, Dr. Scott Noble for his valuable input.

I would like to wish special thanks to Case New Holland (CNH) Ltd for funding, for their technical assistance from the Saskatoon R&D department, and the Saskatoon Quality Assurance Department, particularly Kris Kristjanson, Rick Tenaski, and German Vicencio, for performing the CMM measurements.

Special thanks also to the College of Graduate Studies and Research, University of Saskatchewan Dean's Scholarship and ACCELERATE Saskatchewan for funding support.

I would also like to express my gratitude toward Louis Roth, Mike Miller and Ryan Roberge, Agricultural and Bioresource Engineering and Alex Kozlow, Civil Engineering for their assistance in experiment preparation and data collection.

Finally, I would like to express my deepest thanks to my wife and family for their continued encouragement and reassurance.

TABLE OF CONTENTS

page

LIST OF FIGURES

LIST OF TABLES

LIST OF VARIABLES

A - contact area (m^2)

b,c - weighting constants

c' - cohesion (kPa)

C_u - coefficient of uniformity

C_z - coefficient of curvature

D_{10}, D_{30}, D_{60} - diameter at which 10, 30, and 60 percent of particles pass through, respectively (μm)

E - elastic modulus (Pa)

F - simulated compressive force (N)

F_c - cohesive force (N)

F_i - shear or normal force on ith particle or contact (N)

g_i - acceleration of gravity (m/s^2)

H - material hardness

I - moment of inertia (m^4)

K - shear or normal stiffness (N/m)

k - constant of proportionality

k_e - energy density (J/m^3 or Pa)

k_s - stiffness of each spring (contact stiffness) (N/m)

L - length (m)

m - mass of particle (kg)

t_{crit} - critical timestep (s)

U - overlap (m)

v - simulated relative tangential velocity (m/s)

w - distributed load (N/m)

W - measured soil bin wear rate (mm of radius reduction/50 km of travel)

W_p - predicted wear (mm/50km)

W_a - actual measured wear (mm/50km)

$\ddot{x}_i$ - particle acceleration (m/s^2)

δ - deflection (m)

ϕ - internal angle of friction (degrees)

σ - normal stress (kPa)

τ - shear stress (kPa)

CHAPTER 1 INTRODUCTION

In Saskatchewan alone, about 17.4 million ha (43 million acres) of land are cultivated each year (Saskatchewan Ministry of Agriculture 2008). This is equivalent to a 12-m tillage tool being pulled approximately 14.2 million km (8.9 million miles) through the soil. The interaction of soil and tillage tool results in significant wearing of the tool metal.

Wear will occur in any situation where materials with different hardness are in contact during relative motion. The asperities of the harder surface deform those of the softer material (Kragelskii 1965). It is this very condition which exists during tillage. The sand particles, which can be 2-5 times harder than the metal (Swanson 1993), abrade the metal surface through impact abrasion. Although abrasion is most prevalent, many processes act to remove metal from the tillage tool (Bayhan 2005).

As farmers look for ways to minimize costs and improve efficiency in their operations, reducing the amount of wear which occurs on their tillage tools, and thus minimizing the need for tool replacement, will help to address their concerns for a stronger bottom line. Studies of wear can enable engineers to choose materials and designs which last longer, maintain their optimal shape, and minimize the draft forces required to pull them through the soil.

Unlike typical wear studies of metal-metal contact, tillage wear involves low stress abrasion, much harder abrading particles, and an absence of lubrication. For this reason, wear studies of tillage tools cannot be carried out in the same manner as other wear experiments. To increase the intricacy of the tillage wear scenario, soil texture (Yu

1991), soil particle angularity (Swanson 1993), and soil moisture (Zhang 1992), all of which can vary widely, also affect the type and speed of tool wear.

Although many types of wear tests for tillage tools exist, the nature of the soil-tool interaction makes results difficult to predict. Even though laboratory methods can effectively isolate certain conditions, they do not provide realistic scenarios as would be experienced by a tillage tool in the field. The primary drawback of any of these investigations is that they are time consuming. However, the application of DEM may solve both these issues. Given the continually increasing trend in computing power, DEM simulations could become a realistic replacement for traditional physical tests involving a bulk granular medium such as soil (Krause 2007).

CHAPTER 2 LITERATURE REVIEW

2.1 Wear of Tillage Tools

Wear of agricultural tillage tools is very difficult to quantify and predict. The processes which take place while wear occurs are diverse and can vary widely depending on service conditions and soil properties. Because agricultural tools are also constructed from a wide variety of materials, the wear response to each of these materials will also change based on environmental conditions. The culmination of these factors has made accurate prediction of wear in actual conditions extremely complex.

Wear can be defined as a progressive loss of volume as a result of the relative motion of two bodies (Zhang 1992). Regardless of the perceived smoothness of a material, on a microscopic level, the surfaces of all materials are rough and wavy. As these hills and valleys (also known as asperities) of a material's surface make contact with those of another, these surfaces can be deformed (Kragelskii 1965). The result can be simple friction or plastic deformations which cause the removal of material. Depending on the nature and situations of these interactions, different forms of wear can occur.

There are multiple modes of wear which can take place during a tillage operation. Although the most prevalent is abrasion, loss of tool mass can also take place by means of impact, fretting, and chemical action (Bayhan 2005). Understanding the processes involved in the abrasion process will help to build an understanding of how and why tillage tools wear.

2.2 Abrasive Wear

The process by which wear takes place can be a result of many phenomena. Most commonly, tillage tools wear by the process of abrasion. Abrasion occurs when there is a difference in hardness between materials, and the harder material gouges grooves into the softer material (Breaux and Keska 2002). These grooves are created by removing chip-like fragments from the surface of the worn material through a process known as micro-cutting (Zhang 1992). Some plastic deformation may also create grooves without the removal of material, but continuation of these deformations will result in fatigue and subsequent removal of surface material.

The difference in hardness is essential for abrasive wear. The contact with harder asperities causes a plastic flow of the softer material as they are forced together (Zhang 1992). The tangential motion between the surfaces plows the softer asperities and results in a removal of material. As could also be predicted, the greater the difference between the hardness of the two materials, the greater the potential for wear. Other factors which can affect the wear are the ductility and fracture toughness of the material, as well as the size, shape, and mechanical properties of the abrading particles.

Abrasive wear can be grouped into three categories. Two-body abrasion (grinding abrasion) occurs when the abrading particles are attached to one surface and are wearing a second surface (Moore 1975). Three-body abrasion has free particles which are trapped between two moving surfaces. The last type is most common in tillage tool wear. Impact abrasion occurs when the abrading particles strike the wearing surface. This is the process taking place during tillage as the free-moving soil particles strike the tool

material. Erosion falls into this category, as well as gouging abrasion which can be created during impact with large stones.

2.3 Soil-Tool Abrasive Wear

Traditional studies of wear by tribologists involve the investigation of mechanical components such as bearings. In these situations, the abrading particles are typically metal fragments or previous wear debris. In many conditions, lubrication is also present. These factors differ widely from those which occur in tillage operations because the abrading particles are sand and rocks which may have hardness values 2-5 times greater than the metal (Swanson 1993).

There are many soil conditions which alter the rate of wear, but the two most important are soil texture and soil moisture. Because the hardness of sand and clay particles differ, the relative proportion found in the soil has an effect on the wear rates. Yu (1991) tested some tools in three soil textures and it was discovered that the sandy loam with gravel created more abrasive wear than the loam or the loam with gravel.

In addition to the hardness of the particles, angularity also plays a role. Because the study by Yu (1991) combined the hardness of the gravel with the high angularity of the sand, this soil produced the most wear. In a study by Swanson (1993), it was found that laboratory tests using angular grained sand had wear losses 4-8 times higher than the round-grain particles. However, a study looking at the wear of mouldboard plough blades by Natsis et al. (2007) reported that sand particles of a diameter 0.45 to 0.75 mm create 2-3 times greater wear than those of 1.0 to 1.5 mm in diameter. This could be due to a change in angularity as the smaller particles were more effective at gouging while the larger particles created a blunting effect. Smaller particles also would have created more

contacts with the material which may have resulted in more opportunities for wear to occur.

Clay particles have the lowest particle hardness and angularity, but they also have an affinity for water as well as good cohesive properties. As a result, the clay can coat or combine with the sand and gravel particles, effectively making them softer and smoother upon impact (Zhang 1992). Increasing moisture content only furthers this process and may also create a coating on the tillage tool which creates soil on soil contact and eliminates the soil-metal interaction.

The other factors that affect the wear in tillage tool operations are the working speed and depth and the resulting soil pressure on the tool. Just as in metal-metal wear, increased pressure will increase the wear rate. The pressure changes can be a function of working speed and depth. As reported by Srivastava et al. (2006), the change in draft, and thus soil pressure, changes more drastically with increases in depth than with increases in working speed. Using an inclined tool, supported in the center, an increase of 5 cm of working depth increases draft by about 22 N while an increase in working speed of 0.5 m/s only increases draft by about 1 N for a sandy soil (Srivastava et al 2006).

In the wear of tillage tools, the differences in pressures can result in either low- or high-stress abrasion. In low-stress abrasion, the forces are low enough that the sand particles remain intact while high-stress abrasion crushes the soil particles as they slide across the metal surface (Swanson 1993). High-stress abrasion is common in many tribology systems such as metal-metal friction and is also found in many laboratory wear testers, but in actual service conditions for tillage tools it is low-stress abrasion which dominates (Zhang 1992).

2.4 Wear Characterization Techniques

In order to reduce the impact of wear, studies must be performed to analyze the performance of tool materials. Many different methods have been developed and each has their strengths and weaknesses. Most often a certain technique is used solely for one type of wear scenario.

2.4.1 Laboratory methods to characterize wear

To minimize the time and cost of completing full-scale wear tests, scaled representations are often completed in a laboratory setting. Although they cannot accurately represent the entire spectrum of conditions experienced in the field, lab tests can effectively isolate conditions to determine the individual contribution of each.

2.4.2 Standardized procedures

The American Society for Testing and Materials (ASTM) has developed standard test methods to study the abrasive wear of materials. Multiple conditions can be inspected although the primary wear mode is abrasion. The rubber wheel tests look at low-stress abrasion while the pin-on-disk method can produce either low or high-stress abrasion (Swanson 1993).

Wet Sand Rubber Wheel Test (ASTM Test Method G105)

In the "Wet Sand Rubber Wheel Test" (ASTM 2002), wear is generated by passing a slurry of sand and de-ionized water between a spring-loaded specimen and a rotating rubber-coated wheel. The specimen to be tested is rectangular in shape (50.5 mm x 25.4 mm x 6.35 mm) and the 177.8-mm diameter wheel is covered with a 12.7-mm thick layer of Neoprene rubber (Swanson 1993). The spring holds the specimen against the wheel

with a force of 222 N while the wheel rotates at 245 rpm which is equivalent to a linear speed of 2.28 m/s (8.21 km/h). The test is considered complete after 1000 revolutions.

The slurry is specified to contain 0.94 kg of de-ionized water and 1.5 kg of silica sand of a specified size. Although a round particle sand is recommended, studies have also been conducted using a crushed quartz abrasive which has a greater amount of angularity (Swanson 1993). To ensure that the sand does not settle out of the slurry, stainless steel vanes on the side of the wheel serve to continually agitate the slurry as well as keep the wearing surface of the wheel covered with the abrasive mixture.

Results are determined from a loss of mass which is then converted to a change in volume using the material density. However, to find these mass losses, multiple measurements are taken with varying test conditions. Each sample is initially run for 1000 revolutions on a 50 Shore A hardness rubber-rimmed wheel and then followed by three runs at increasing wheel hardness for 100 revolutions each. The rubber hardness increments are typically 50, 60, and 70 Shore A durometer. The weights of the specimens are measured before and after each of the runs. Weight losses are then plotted against the rim hardness on a semi-log plot and the value for weight loss is taken as the value at 60 Shore A durometer from the fitted regression line. For each material, this entire procedure should be repeated at least three times to limit variability (Swanson 1993).

Dry sand rubber wheel test (ASTM Test Method G65)

Similar to the Wet Sand Rubber Wheel test, in the Dry Sand Rubber Wheel test (ASTM 2000) the specimen is worn by the sand passing between the spring-loaded specimen and a rotating rubber-rimmed wheel. The specimen is slightly larger (76.2 mm

x 25.4 mm x 6.35 mm) and the wheel is 228.6 mm in diameter. The rubber used is made of chlorobutyl at a hardness of about 60 Shore A durometer and the wheel rotates at 200 rpm. Sand with a diameter of 250 μm, similar to that used in the Wet Sand test, is gravity fed from a hopper to a point on the wheel just ahead of the specimen.

Four separate procedures are defined for the Dry Sand Rubber Wheel Test and each has its own specifications for spring force on the specimen and number of revolutions. With the Dry Sand method, only a single run must be conducted for each specimen but it is still recommended to complete three to four replications for each material tested. Wear is quantified by a weight loss converted to a change in volume, using material density.

Pin-on-abrasive-disk test (ASTM Test Method G99-05)

The ASTM (1998) standard allows the material to be tested to be configured as either the disk or the pin. The pin is either spherical or cylindrical with a rounded tip and has a diameter between 2 and 10 mm. Through the use of a lever arm and masses, the pin is loaded against the disk (30 to 100 mm diameter and 2 to 10 mm thickness) with the disk being either horizontal or vertical.

The test operates by rotating the disk or the pin about the center axis of the disk. The test concludes after a given number of rotations. Wear is measured by the mass of material removed or the reduction in the specimen dimension. Typically, the pin is used as the specimen to be tested.

Although the ASTM standard does not provide standard speeds, loads, or distances, a study by Swanson (1993) looked at previous experiments using a similar technique, before the development of the ASTM standard. The specimens were loaded with a force of 5 N while the disk rotated at 20 rpm. The test was completed with a linear distance

traveled of 3.15 m. Another addition to this methodology which was not described in the ASTM standard was a lateral feed of the specimen holder (Figure 2.1) such that fresh wearing material was exposed to the specimen for each revolution (Swanson 1993).

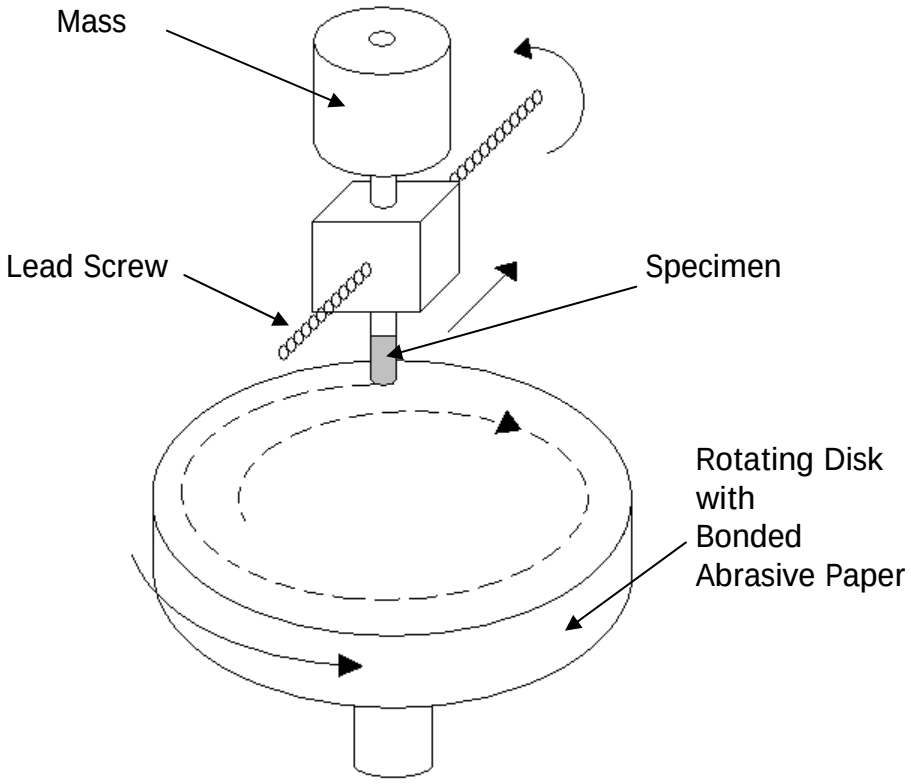

Figure 2.1. Pin-on-disk apparatus as described by Swanson (1993) with lateral feed.

In tests conducted by Dwivedi (2004), a rectangular specimen was tested with a rounded end. The tests were run at loads between 1 and 4 N and because hardsurfacings were being tested, weight loss was calculated after 1000 m of sliding distance.

2.4.3 Soil bin tests

In order to create more realistic wear conditions for a tillage operation without conducting a full-scale field experiment, soil bins are used to mimic field conditions. Some advantages of using soil bins include the ability to provide a more precise and controlled research medium compared to field tests and the opportunity to work in all seasons and all weather conditions. More variables can be studied and the results can be more reliable as more sophisticated controls and data acquisition systems can be employed. Soil bins also allow tests to be conducted on smaller, more economical models which can predict the performance of full scale-prototypes (Gill et al. 1994).

Soil bins can be constructed in a variety of manners depending on their intended use. For wear testing, soil bins are circular in nature to allow for long, continuous travel distances. Kushwaha and Shi (1991) described a circular bin which held the specimen stationary and the soil moved across it as the bin was rotated. This circular motion is sufficient to provide the centrifugal soil forces which, in turn, cause wear to occur. The bin was less than 1 m in diameter and could produce linear speeds at the specimen of 4.4 to 4.5 m/s which produced a small pressure force. This tester produced accelerated wear rates and by varying soils and tool materials, could examine many combinations in a short amount of time. Results were similar to other documented wear tests and showed wear patterns that would be expected in field conditions with the exception of large stone interactions (Kushwaha and Shi 1991).

More common circular soil bin tests use a stationary soil bin with a rotating carriage which pulls the specimen through the soil. Two different circular soil bins have been constructed at the University of Saskatchewan. Zhang (1992) described a bin 3.05 m in

diameter with a 10-kW electric motor driving the hydraulically operated carriage. Scrapers and packers were used to recondition the soil after each pass before the specimen returned on the next revolution.

The benefit of this type of circular soil bin is the more accurate representation of field conditions. Compaction levels and even foreign objects could be added to simulate actual soil. The one advantage of the smaller bin described by Kushwaha and Shi (1991) is that multiple soils can easily be tested while in the larger bins it is more difficult to change soils. Another problem indicated by Zhang (1992) and Graff et al. (2007) is the difficulty in maintaining a consistent moisture content throughout the trials. Although water is continually added, variations are not easily detected and the resulting wear rates may also vary. Accelerated and uncharacteristic wear may also develop if the soil is allowed to settle and compact directly below the specimen (Graff et al. 2007). The other disadvantage of the circular soil bin is the uneven wear created by the circular motion. Care needs to be taken to take into account the effect of circular travel as higher wear rates can result on portions of the tool which are closer to the outer radius of the bin (Graff et al. 2007).

2.4.4 Field methods

Many wear tests are conducted with prototype or production equipment in real service conditions in order to represent actual wear response. Although often more costly and time consuming, the results allow prediction of wear rates and precise wear performance as opposed to simple comparisons between materials or individual conditions.

The conditions under which field experiments are performed can vary widely. It is the goal to operate the tests under conditions which match typical operating

circumstances (Er and Par 2006). Depending on the tool being tested and conditions of interest (i.e. working speed, working depth), the selected travel speeds and distances may be altered. However, certain commonalities often emerge.

In order to replicate actual service conditions, the implement used to test the tools is a standard production machine as would be used under normal circumstances. All treatments and replications are placed on the machine because of the difficulty in measuring the distance, speed, and service conditions of a given set of tests in order to be able to replicate these conditions for the following set of treatments. To minimize interaction effects and differences between wear rates at different mounting locations (i.e. in the tractor wheel tracks), the tools must be randomly rearranged on the implement (Wingate-Hill et al. 1979). The difference between points mounted on the first row compared to the back row will also influence wear rates. Graff et al. (2007) also noted a similar randomization process in soil bin tests when there were multiple specimens being tested simultaneously. To eliminate any effect of one tool having on the one beside it, the positions were randomized to eliminate any bias due to relative position.

The measurement of soil conditions in field tests allows characterization of the soils for future comparisons and predictions. Typical measurements include soil moisture contents and soil texture including the relative stoniness of the soil (Wingate-Hill et al. 1979). The measure of a soil's cone index may also be beneficial to quantify compaction levels or differences between the 'fresh' soil and that which has been compacted by the tractor or implement tires (Owsiak 1997, 1999). Similarly, a measure of soil bulk density may also be recorded (Wingate-Hill et al. 1979). However, because soils are very heterogeneous in nature, a representative sample may be difficult to achieve.

Field tests are conducted with the purpose of mimicking realistic situations and as such, it is not the intent to gather data which are extremely precise and which could be used for mathematical modeling. The objective is to obtain general conclusions about certain materials or the differences in certain conditions. For this reason, wear is typically determined by a change in mass or tool length. In the case of the study by Er and Par (2006), the specimens to be tested were large plowshares and the mass of material lost was substantial, minimizing the need for more complex determination methods. These measurement methods are intended to be simple because they are often performed in the field.

2.5 Measurement Techniques

To characterize the wear, measurements are often made to determine a decrease in specimen dimension or an overall mass loss which can also be used to calculate an average volume loss. As reported by Kragelskii (1965), radiation can also be used. The method was developed by the Scientific Research Institute of the Railway Industry. A radioactive source (usually thallium) is incorporated into the metal and the magnitude of wear is obtained from the change in the intensity of the radiation at the surface. The intensity grows as the distance between the source and the surface decreases as a result of wear.

Other measurement methods have also been invented to meet the needs of individual tests, whether they are laboratory or field experiments. Because the specimens in the standardized tests are constructed of a single material and cut into simple geometries in order to compare resistance of multiple materials, a measurement of mass converted to volume is possible and applicable. However, in the studies by Graff et al. (2007) and

Zhang (1992), where the materials tested were subject to a hardsurface treatment, a mass measurement was not representative of the performance of the material in question because of the heterogeneous nature of the sample. Instead, images of the tool profile were analyzed. Photos of multiple angles can be used to determine a change in the profile area (Zhang 1992) or traces of the tool profile can indicate the linear recession of the tool's leading edge (Graff et al. 2007).

Owsiak (1999) used a method to directly measure linear decrease in the length of spring tine cultivator points. Holes were drilled into the back, non-wearing surface of the points to provide a mount for a reference plate. Measurements were then taken from the edge of this reference plate to the leading edge of the point with a slide calliper. The thickness of the point was also measured with the calliper at 9 pre-determined locations. In studies by Owsiak (1997) and Nastis et al. (2007), an identical procedure of measuring the change in a dimension from a non wearing surface was used on wedge-shaped ridger shares and mouldboard ploughshares, respectively. Field tests as described by Er and Par (2006), Bayhan (2005), Nastis et al. (2007), and Feilke et al. (1993) used the mass loss of the entire tool being tested.

2.6 Comparison of Wear Test Techniques

There are benefits and drawbacks to all forms of wear studies. As Swanson (1993) outlined in his study of laboratory and field wear tests, field tests can provide the most realistic results because they include a large range of the soil types and conditions which exist and as such, the results can be used to estimate tool life. However, these tests can be expensive and time consuming to conduct and because of the variability in conditions, characterizing the processes which are taking place is often not possible. Regarding lab

tests, costs are reduced and many materials can be tested within a short time. Factors can be controlled and the impact of certain changes in conditions can be examined. The main disadvantage for laboratory testing is the poor representation of actual field conditions. Only general comparisons between materials or individual conditions can be made and they cannot be extrapolated to all service conditions.

Laboratory or field tests can provide significant results as long as their limitations are understood. The following is a study on the effectiveness of wear test procedures.

Results from the Wet and Dry Sand Rubber Wheel Tests were very similar in the study by Swanson (1993). Although the total wear was greater for the Dry Sand test, the relative wear resistances were nearly identical with the exception of very hard materials. Possible differences could have been created because of the heat generated in the Dry Sand tests which altered the microstructure of the sample.

The Wet Sand tests required more time because of the multiple measurements that were required, but other problems were also encountered. When reinserting the specimen after measuring, it was important to align it identically to the previous run or the wear scar would be altered and change the wear rate. It was also found that different rubber wheels, although they had the same nominal hardness, produced differing results (Swanson 1993). For these reasons, much care needs to be taken to ensure additional variation is not introduced into the tests.

A drawback of both types of rubber wheel tests was the non-uniformity of the wear of the specimen. Where particles first came in contact with the specimen, an irregular pattern was created such as would occur with rolling and only in the center did the predicted wear grooves form from sliding abrasion. These two effects' impact relative to

each other was also dependant on the hardness of the specimen as abrasion took precedence over the rolling wear with harder specimens (Swanson 1993). Differences also existed between these methods and field results, because rolling of particles was more prevalent in field conditions and variation in particle size due to the heterogeneity of the soil created different wear patterns in field results (Zhang 1992).

Results from the pin-on-disk method showed an identical ranking in terms of wear resistance for the various specimens. The difference was in the amount of wear which occurred. Because the particles were fixed on the abrasive disk, they were not free to reorient themselves and rolling could not take place. This created more cutting and plowing in the abrasion process (Swanson 1993).

The result of a comparison between field and standardized laboratory tests showed high correlation for plain carbon and alloy steels. Conversely, the more heterogeneous and brittle hardsurfacings showed little relation between the two methods (Swanson 1993).

With the intent to be more representative of soil conditions, the accelerated wear tester created from the centrifugal force of a small soil bin created normal pressures and draft forces similar to field situations (Kushwaha and Shi 1991). The ability to quickly change soils was effective for observing a variety of soil conditions.

For all of the previous laboratory tests, it was noted that although representative of a majority of the abrasive wear process, none of these methods could accurately recreate impacts by large stones (Swanson 1993; Kushwaha and Shi 1991; Er and Par 2006). The effect of impacts generates a wear unlike that of abrasive wear and therefore must be considered separately.

When using a larger, stationary soil bin, the wear conditions also accurately matched field conditions. Moisture contents were difficult to control and monitor (Zhang 1992; Graff et al. 2007), but relatively stable conditions could be created. There is some small effect of the circular motion as uneven wear was produced, but the larger diameter soil bins minimize this effect as the working path approaches a straight line. A significant effect noted by Graff et al. (2007) with regard to the circular motion was the tendency to create a compacted layer beneath the test specimen as a result of repeated travel over the same path. Intermittent loosening and moisture content control are required to minimize its impact (Graff et al. 2007).

In field tests, Owsiak (1999) also reported the importance of specimen randomization as the wear rate differed between points located in the front row of the machine relative to the rear. It was also found that wear rates increase on points which are in the tracks of the tractor or implement.

2.7 Wear Simulation

In order to select the appropriate materials for soil-engaging tools, wear studies are required. However, these experiments can be time consuming and are limited to materials and conditions which are available to the researcher. This is particularly true for field tests and soil bin tests, and although the laboratory methods can give some indication of wear performance, the accuracy and comparability to field conditions is questionable.

A promising method to characterize wear is in computer simulation. Much study has been done to simulate wear using the Finite Element Method (FEM) and ANSYS software (an FEM analysis package developed by Ansys, Inc, Canonsburg, PA),

particularly in the medical and dental fields where studies have looked at joint and enamel or tooth wear, respectively (Fialho et al. 2007; Bevill et al. 2004; Ford et al. 2009). Other research has been done using FEM to look at metallic wear in machines as well, but the primary modes of wear being observed differed from that which occurs in a tillage operation.

To properly simulate tillage tool wear as a way of predicting tool life, a granular abrasion process must be implemented. To date, there has been little study of wear using DEM which can model granular flow. The application of DEM shows great prospects (Krause 2007) as DEM has the capability of quickly producing simulated results that are otherwise impossible to determine. Nicholas Fillot and Ivan Iordanoff have published some preliminary studies of wear using the DEM where the focus was on studying three body wear in which abrading particles are contained between two solid bodies. Fillot et al. (2005) found that the contacts and properties of the particles are quite influential in the results. The study mostly examined the impact of the ejected particles on further wear of the material. Because of this phenomenon, only DEM, which tracks these ejected particles, can properly simulate these wear conditions. Fillot et al. (2006) furthered this study to also consider the adhesion of particles. Although the focus was more on ejected particles, adhesion of particles creates a situation more comparable to a soil-metal interaction. When applying DEM more closely, Iordanoff et al. (2007) concluded that the applied two-dimensional model was "too simplified compared to reality". The need for a method which would include a continuous medium far from the actual wear location as well as the small scale interaction at the actual point of wear was expressed.

Although there has been some use of DEM relating to wear for certain mining processes, wear during tillage creates much different conditions. A DEM model would have the ability to account for pressure differences in a soil profile and variability in the abrading particles such as size, angularity, and cohesiveness. These are the conditions which are unique to abrasive wear in a tillage operation. Quick and accurate results of soil-engaging tool wear could be obtained with the effective combination of current test methodologies and computer simulation techniques through the use of a DEM simulation.

2.8 Discrete Element Method

The discrete element method (DEM) was first documented by Cundall and Strack (1979). DEM is a numerical method which explicitly calculates equilibrium contact forces and displacements for each individual particle and its contacts with either other particles or boundary walls. The most valuable feature of the DEM is that it assumes constant velocity and acceleration over a given timestep which makes it possible to solve a non-linear interaction without requiring large memory capabilities or an iterative procedure (Cundall and Strack 1979).

Calculations are completed by alternating between Newton's second law of each particle and the force-displacement law at the contacts. To perform these calculations, the following assumptions are made:

- particles are assumed rigid bodies,
- deformations are small and are accounted for by particle overlap,
- contacts occur at a very small area (i.e. a point), and
- velocities and accelerations are constant over each timestep.

Forces are generated using the force-displacement law as a function of the overlap at a particle contact. In general,

$$F_i = KU \quad , \tag{2.1}$$

where F_i = shear or normal force on ith particle or contact (N),

K = shear or normal stiffness (N/m), and

U = overlap (m).

Once forces have been determined, the calculation cycle moves to Newton's second law in which,

$$F_i = m(\ddot{x}_i - g_i), \tag{2.2}$$

where F_i = shear or normal force on ith particle or contact (N),

m = mass of particle (kg),

$\ddot{x}_i$ = particle acceleration (m/s^2), and

g_i = acceleration of gravity (m/s^2).

It should be noted that similar equations also exist for moments and angular acceleration. With the updated accelerations and velocities, contacts can be updated and the calculation cycle returns to the force-displacement law.

An important part of DEM is the application of contact models. At any point of contact, at least one of three possible situations applies: contact, slip, or bonding. Contact-stiffness models determine the value used for the stiffness coefficient in the force-displacement law calculation when a simple contact occurs. These can be linear combinations of individual stiffness values or a non-linear formulation such as the Hertz-Mindlin model, which uses shear modulus and Poisson's ratio to determine stiffness

coefficients (Itasca 2003). Slip models incorporate the contribution of friction to contact forces to determine whether or not relative motion will occur in the tangential direction.

At points of contact, bonds are also allowed to form. These bonds have a certain strength and stiffness to resist forces. Once the incident forces exceed the strength of the bonds, the bonds break and simple contact models apply.

Data to be collected from the DEM model are gathered via measurement spheres. Each sphere tracks the existence of particles and associated contacts within the sphere. By utilizing the data collected in the measurement spheres, energies can be traced. Typical examples of the types of energy that are recorded are body work, bond energy, boundary work, frictional work, kinetic energy, and strain energy (Itasca 2003).

The key to successful implementation of the DEM is the selection of the appropriate timestep size which satisfies the assumption that velocity, acceleration, and force are constant over the timestep. However, it is also a compromise between accuracy and computing power because a smaller timestep will give the most accurate results, but also requires more calculation time to perform the simulation. The stable solution for the critical timestep is calculated from a mass-spring system (Itasca 2003). Considering first a single spring and point mass and moving to an infinite combination, the solution becomes,

$$t_{crit} = \sqrt{\frac{m}{k_s}}, \qquad 2.3$$

where t_{crit} = critical timestep (s),

m = mass of point mass (particle) (kg), and

k_s = stiffness of each spring (contact stiffness) (N/m).

In order for DEM to calculate all of the above values, certain input values are required from the user. These primarily relate to the characteristics of the particles and the nature of their contacts. Table 2.1 summarizes the various values that are required depending on the applied model.

Table 2.1. Input values required from user by DEM.

Particle Parameters	Contact models	Slip models	Bonds
radius	shear stiffness	coefficient of static friction	critical shear stress
particle density	normal stiffness	coefficient of rolling friction	critical normal stress
	Poisson's ratio		
	shear modulus		
	coefficient of restitution		

Of greatest importance to the success of DEM simulations is the ability to select the proper values for the input parameters for the contact models. The difficulty is in determining these values as often recorded data on the parameters do not exist. A particular example is the coefficient of restitution. Although difficult to determine exact values for all types of interactions, the simulation can be greatly affected by the coefficient of restitution.

2.8.1 Current DEM applications

There has been increasing development in the past thirty years since the introduction of the DEM by Cundall and Strack (1979) as the number of articles published on the method has increased dramatically (Zhu et al. 2007). The majority focus on bulk solids handling such as flow through hoppers (Anand et al. 2008; Kruggel-Emden et al. 2006),

chutes (Zhang and Vu-Quoc 2000), and conveyors (Minkin et al. 2007), particularly in the pharmaceutical industry.

Because pharmaceuticals typically involve very homogenous dispersions of particle sizes in standard shapes, the application of DEM is easier than other situations where particle characteristics vary within the sample. Examples of applications to the pharmaceutical industry include work by Lewis et al. (2005) where they combined DEM with finite element analysis to study the process of compressing powders into pharmaceutical tablets by comparing particle shapes and sizes. Baxter et al. (2000) used DEM to improve the handling of the powders used to create pharmaceuticals.

Much work with DEM has also focused on the mining industry and milling processes. This includes everything from force analysis of front end loader buckets (Nezami et al. 2007) to wave propagation through rock masses upon blasting (Fan et al. 2004). Power consumption from rolling mills can be determined by the energy lost in collisions inside tumbling mills or from the torques created through interactions with the drum (Djordjevic 2003) as recorded by a DEM simulation. It was found that this method produced statistically identical results to actual power consumption measurements.

This is also one of the few areas where the application of DEM to wear is also employed. Kalala et al. (2005) and Cleary (1998) used DEM to look at the forces generated on the liners and lifters in a tumbling mill drum. From these forces, wear values could be estimated.

Some application to agriculture has also been recorded. Multiple studies have been conducted by Martin Roberge (M. Roberge, Sr. Project Engineer, Digital Prototyping and Simulation, CNH Canada, Ltd. Saskatoon, SK) employing DEM. The studies have

involved tillage tools and the prediction of draft forces and soil flows. Li et al. (2003) applied DEM to sieving procedures as it may apply to particle size distribution or agricultural practices. They used polyethylene pellets which would be comparable to a cereal grain. Landry et al. (2006) also employed DEM to model manure–machine interactions in a prototype manure spreader. Liu et al. (2008) used DEM to model the lateral pressures in a grain storage bin and the changes in pressure due to external vibrations. Other applications to agriculture were recorded by Van Zeebroeck et al. (2008) in their study of apple bruising during truck transport. They were able to determine optimal placement within the truck and truck speeds to minimize the impact force which could cause bruising.

CHAPTER 3 OBJECTIVES

Techniques capable of more easily indicating implement wear would be beneficial in the design and development of agricultural machines, especially soil-engaging tools. The purpose of this research was to determine a method to simulate wear tests of tillage tools by utilizing the discrete element method (DEM). The expected advantage of employing the results of a DEM simulation is that wear simulations can be performed in less time and with less variability of results.

The objectives of the study were to:

- collect a set of wear data from a circular soil bin experiment for future use in verifying the results of a DEM simulation,
- determine a method to re-create the conditions present in a circular soil bin through the use of a DEM simulation, and
- create and verify a relationship which can predict wear based on parameters obtained from a DEM simulation.

Future work, beyond the scope of this project, could be performed to use the model to predict the wear of any material. It is expected that this work will support development of future models able to predict the wear of other tool shapes or materials in various soil conditions.

CHAPTER 4 METHODS AND MATERIALS

4.1 Soil Bin Testing

The soil bin used for these tests was located at the University of Saskatchewan, Saskatoon, SK (Figure 4.1). This circular soil bin pulls a tillage tool sample through a soil medium intended to represent field conditions. The carriage was powered using a 37.3 kW (50-hp) three-phase electric motor which ran a variable-flow hydraulic power unit controlled with electric solenoids. The hydraulic power unit served to operate a drive train from a self-propelled combine which rotated the carriage of the soil bin. The inner and outer diameters of the bin were 2.3 and 4.3 m (7.5 and 14 ft), respectively and at a working diameter of 3.2 m (10.5 ft), the working speed range was 0 to 9.7 km/h (6 mi/h). The layer of soil was approximately 0.6 m (2 ft) deep. The bin was also designed to allow the mechanism to rotate in either direction to counteract the effects of a circular motion. A magnetic pick up connected to a data logger allowed the number of revolutions of the tool carriage to be counted for tool travel distance measurement.

Figure 4.1. Circular soil bin housed at the University of Saskatchewan with stationary bin and hydraulically powered carriage.

4.1.1 Wear specimen design

As a compromise between simplicity for future modeling and ease of use in the soil bin, a cylindrical rod pulled horizontally was chosen as the tool shape (Figure 4.2). The rounded profile allowed soil to move freely past the tool and there was no effect of a corner or sharp edge that would wear differently over time. Although the cylindrical shape was different than any standard tillage tool shapes, the cylindrical profile provided a range of soil pressures, and thus a range of wear rates, while also maintaining a simple geometry which was easy to recreate in the simulations. In addition, determining the

level of wear on a simple geometry such as a cylinder was much less complex than measuring volume or shape changes on a more complex tool.

Figure 4.2. Test specimen geometry.

The length of the bar was chosen to be approximately half the available width of the soil bin, 400 mm. To determine an appropriate diameter, calculations were completed to find a diameter that would provide an acceptable amount of flexure. According to draft data recorded by Hunt (1983) for a rodweeder and the flexure formula,

$$\delta = \frac{wL^4}{384EI}, \qquad 4.1$$

where δ = deflection (m),

w = distributed load (N/m),

L = length (m),

E = elastic modulus (Pa), and

I = moment of inertia (m^4),

a standard material size with a diameter of 25 mm was found to provide about 6 μm of deflection in the center of the bar for aluminum and was considered sufficient for the experiment.

Two materials were selected from which the bars would be constructed. Materials were selected based on anticipated wear characteristics and availability, and not necessarily those which would be common in the manufacture of tillage tools. To ensure that quantifiable wear would occur, one of the materials selected was 6061 aluminum. A steel sample (AISI 1018) was chosen as the other material in order to provide significant contrast in wear life. Based on hardness values (95 HB for 6061-T6 aluminum and 131 HB for cold drawn AISI 1018), it was assumed that the aluminum would show much higher wear rates. Three replications of each material were tested with the designation AA1 through AA3 for aluminum and AS1 through AS3 for steel.

Steel and aluminum are not materials used for construction of tillage tools. However, the focus of the work was on developing the procedure to determine a level of wear and thus, a similar procedure could be performed on any material type. The aluminum and steel samples wore at a rate more acceptable for the purpose of this study, but the process could be repeated with typical tool materials over a longer period of time.

Figure 4.3 illustrates the mounting bracket used to hold the bars in the soil bin. A single bolt at each end of the rod gripped the rod in the bracket. The protective sleeves were also mounted via the bolts. The sleeves were added to eliminate any wear on the ends of the bar as the coordinate measuring machine (CMM), used to measure the bar's radius, required unaltered material in these regions for calibration during each measurement. These sleeves were replaced, as needed.

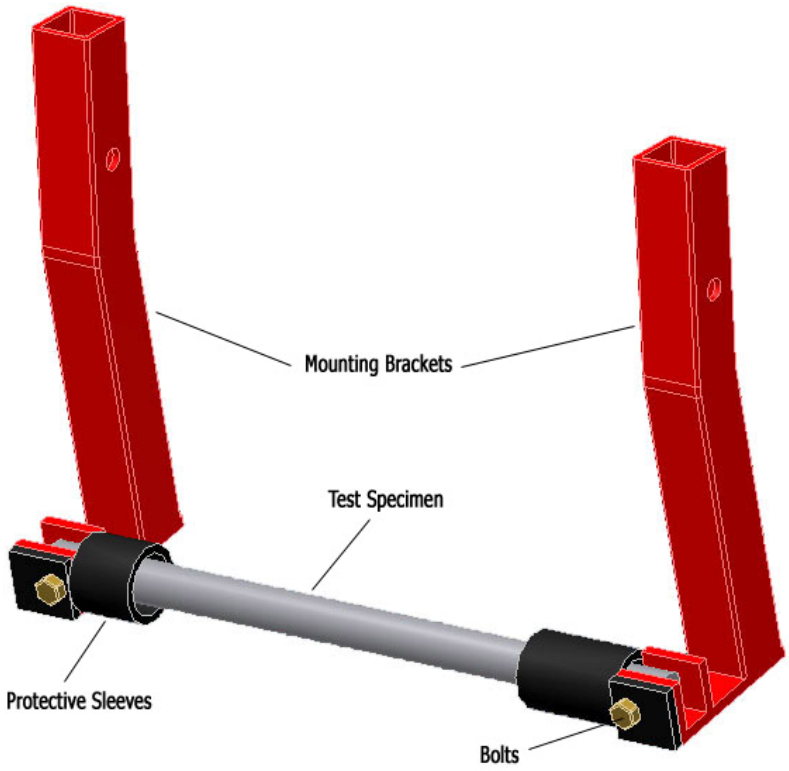

Figure 4.3. Bracket used to mount specimen in the soil bin.

4.1.2 Operating conditions

The soil bin was equipped with a set of four disks to loosen and level the soil for each pass. Following the disks were three packing wheels which provided a consistent level of compaction to accelerate wear and more accurately represent field tillage conditions. Along the inner circumference of the bin, spray nozzles regularly added water to the soil to maintain a moisture content of approximately 4 % w.b. Soil texture was 8% gravel, 72% sand, 7% silt, and 13% clay which was classified as loamy sand.

The average speed of the center of the bar (located at 1.64 m from the center of rotation) was set at 8 km/h. The bar was run at a depth of approximately 7.5 cm relative to the center of the bar. Based on the dimensions of the bin, 50 km of travel could be completed each day. As such, measurement intervals were set at 50 km. The

experimental design had two material types, three replications per material with 9 repeated measures which constituted 400 km of total travel for each bar.

Although the soil bin was capable of operating in both directions, a single direction was used in wearing the specimens due to the time required to convert the soil bin to operate in the opposite direction. Reversing the direction has the advantage of balancing the distance travelled and speeds encountered for each end of the specimen. However, this was not of great concern for the purpose of these tests and instead, measurements were limited to the center portions of the specimen where the wear rates would be less affected by the circular motion.

4.1.3 Data acquisition

The coordinate system set for the bar was selected based on conventions from the coordinate measuring machine (CMM) that was used for determining change in tool shape. This convention created the origin on the central axis of the bar at the outermost edge according to the direction the bar traveled through the soil bin (Figure 4.4). As such, the positive x- direction faced rearward, parallel to the plane of motion. Positive y was in the downward direction, perpendicular to the plane of motion and positive z was along the axis of the bar towards the outside of the soil bin.

The level of wear was determined from the change in radius of the circular bar near the center of its length. Twenty points around the circumference of the bars were measured at the middle of the bar (z = -200 mm) in addition to 2 regions on either side of the middle (z = -174.6 mm and z = -225.4 mm). Figure 4.4 illustrates these measurement areas labelled B, A, and C, respectively. Because the soil bin was rotating in a single direction, the linear speed and total linear distance varied over the length of the bar. For

this reason, measurements were limited to an area close to the middle where variations would be minimal. Location A was at the outer radius which resulted in a speed and distance which was 1.6 % higher than Location B. The opposite is true for Location C. The other benefit of measuring wear near the center of the bar was that the soil flow would be relatively unaffected by the disturbances created by the specimen's mounting brackets and the protective sleeves as shown in Figure 4.3.

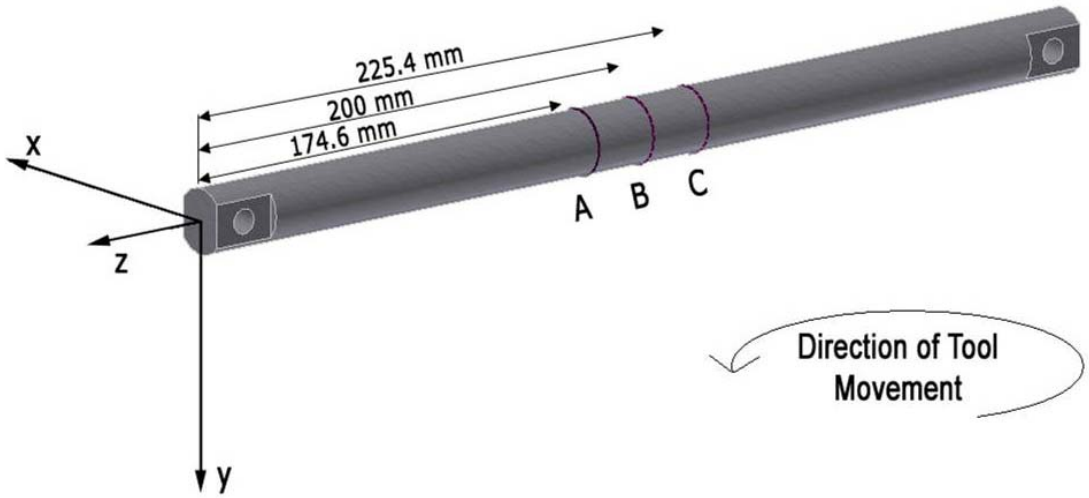

Figure 4.4. Coordinate system for test specimen.

Radii of the test specimens were determined using a CMM. By calibrating to known, unchanging locations on the bar, precise measurements within the three x-y planes at each of the 20 points around the circumference could be recorded. Angles were measured beginning at the leading edge (-12.7 mm, 0 mm , $Z_{A,B,C}$) and increasing counterclockwise such that 90 degrees would be at the bottom (0 mm, 12.7 mm, $Z_{A,B,C}$), etc. (Figure 4.5).

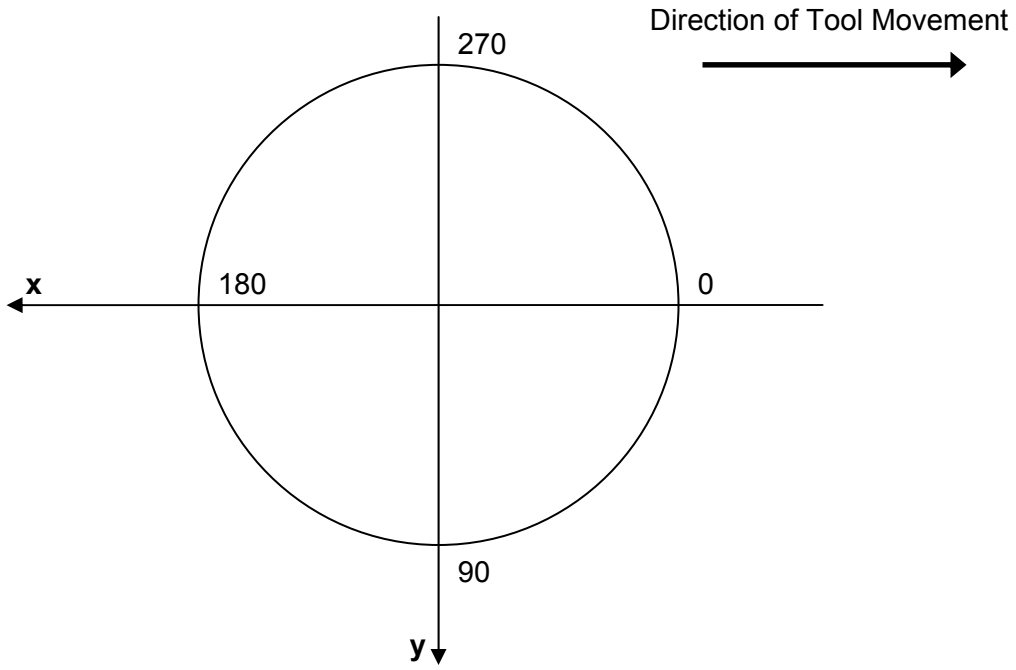

Figure 4.5. Schematic of bar profile indicating conventions for angles.

In addition to profile measurements, the mass of the bar was also recorded. Because the bars were constructed of a single material, the amount of mass loss could be converted to a loss of volume using the material density. The densities used for calculations were 2.70 and 7.87 g/cm^3 for 6061 aluminum and 1018 steel, respectively.

4.2 DEM Computer Simulation

The DEM simulations were performed using EDEM 3D v. 2.0 from DEM Solutions (Edinburgh, Scotland). This software employs the Discrete Element Method in an object oriented user interface, eliminating the need for complex coding while providing visual representation of all simulations.

The purpose of the simulations was to imitate conditions present in the soil bin testing as closely as possible. However, concessions were made to minimize the size of data files and the corresponding time to complete the simulations.

4.2.1 Simulation design

Wear is a process which is difficult to model. Because of the time dependence and the slow rate of progression, wear is nearly impossible to recreate in a simulation. It was originally hypothesized that a tool could be represented by a group of particles bound together using a DEM bonding model. As the forces exceeded the bond strength and the bonds broke, these particles would be released and the tool would slowly change shape. Upon further experimentation, it was found that this was an unrealistic expectation as the number of bonded particles required in the tool to create a realistic wear rate was extremely high. To ensure the particles were small enough such that removal of a particle per calculation cycle would meet the wear rate measured in the soil bin, the tool would need to be constructed from particles numbering on the order of 10^{35}. The time required to run such a simulation was unreasonable. Thus, a new approach was taken.

Similar to the wear studies in roller mills as recorded by Kalala et al. (2005) and Cleary (1998), forces and other readily available data from a DEM simulation could be used to predict wear. Archard and Hirst (1956) developed a relationship for sliding wear which states that wear is proportional to the applied load and the sliding distance, and inversely proportional to the flow pressure of the softer material. This relationship, called the Archard Equation, is often simplified as,

$$W \propto \frac{Fv}{H}, \tag{4.2}$$

where W = wear rate,

F = applied normal load,

v = relative velocity, and

H = material hardness.

It is then justified to assume that a relationship between wear rate and the product of normal force and relative velocity would exist for a given type of material. As such, the DEM simulations were used to estimate the compressive force created by the soil particles on the tool and relative velocity between soil and tool material. Using the actual measured wear data from the soil bin, an empirical relationship could be developed such that future wear or other studies could predict wear based only on the normal force and relative velocity data obtained from a DEM solution.

Due to the fact that wear rates were small for the steel bars in the soil bin, only the aluminum bars were used for the purpose of generating the empirical relationship. Two of the replications were used for creating the relationship while the other was used for verification. Assuming all other conditions were kept constant, changing the tool material would not affect the compressive force and relative velocity measured by the simulation. Therefore, differences in wear rate determined by the empirical relationship must only be due to material properties (i.e. material hardness as described by the Archard Equation). It is then possible to later modify the empirical relationship to also predict wear of another material (i.e. steel) by incorporating a constant which is a function of the material hardness.

The relationship would be created by considering each of the 11 measurement locations which made contact with soil, assuming that larger wear would have been measured at locations with a larger compressive force and relative velocity. A simulation was run for all eight 50-km intervals and for both specimens used for creating the relationship. As such, there were 176 data points available to generate the relationship.

4.2.2 Simulation components

The simulated tool to be worn was designed to replicate the bars used in the soil bin. Because the circular motion of the bar could not be replicated in the simulation and the measurements were limited to the center of the bar, only a short section of a cylinder was used. According to the locations of the CMM measurements of the soil bin specimens, the tool was separated into 18-degree segments along the surface in contact with the soil. These segments were aligned to match the radius measurement locations from the soil bin experiment. The center of the segments corresponded to the 270-degree through 90-degree locations along the leading face of the bar, according to the CMM convention. Figure 4.6 illustrates these segments at which force and relative tangential velocity could be recorded in the simulation with segment '342' highlighted. Segments were named according to the angle at the middle of the segment. Therefore, segment 342 ranged between 333 and 351 degrees (9 degrees on either side of center).

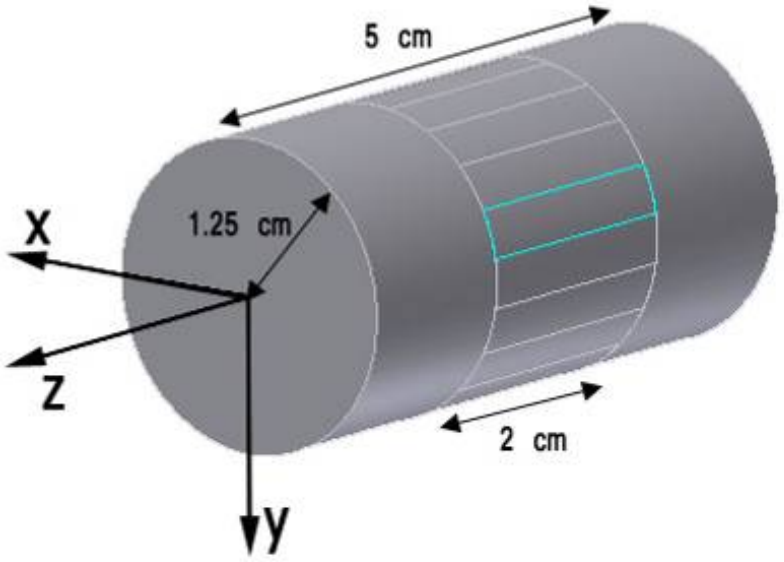

Figure 4.6. Diagram of tool used in simulation shown from the leading face.

As can be seen, the bar was limited to 5 cm in length, only 2 cm of which was divided into the segments where data would be collected. Figure 4.5 shows the bar before wear. However, prior to each simulation, the bar was re-drawn to represent the amount of wear which actually accumulated at the end of the previous 50-km interval in the soil bin (Figure 4.7). As seen in Figure 4.7, the change in shape altered the shape of the face of the segment as well. Although segment 342 is still in the same location, the face of the segment has a new curvature and a slightly larger area. As all data were taken as an average across the entire face, this small change in area was assumed to have negligible effect on the data.

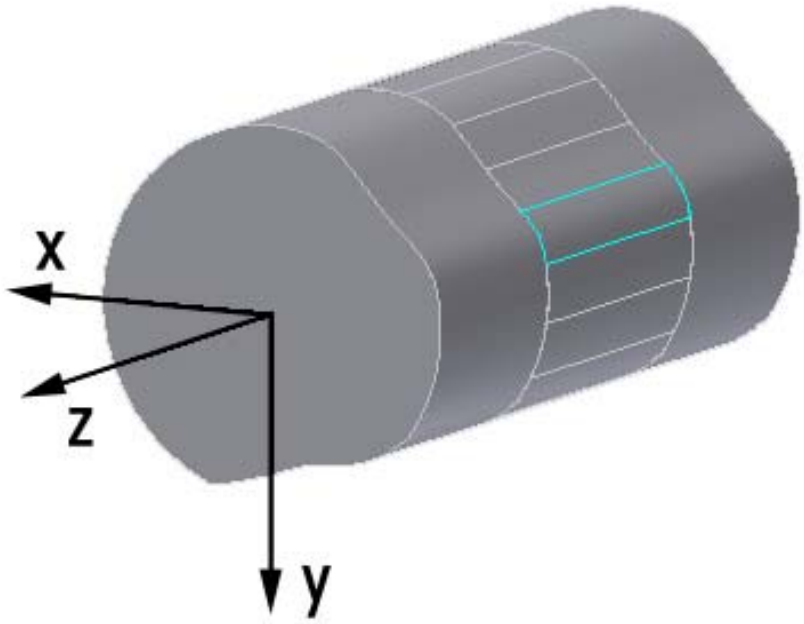

Figure 4.7. Updated tool shape to include previous wear.

After test simulation runs, changes were made to the shape of the tool to account for an occurrence which happened in the soil bin and is discussed further in Section 5.2. A soil wedge formed on the leading face of the bar such that the soil flow pattern changed. Because the simulation did not provide sufficient time for this phenomenon to develop, the soil wedge was recreated with a solid geometry (Figure 4.8). The shape of the wedge was created based on measurements from the soil bin tests and was assumed constant for all simulations, regardless of previous amounts of wear. The wedge was created between angles of 342 and 36 degrees on the bar. From Figure 4.8, it can be seen that half of segment 342 was covered by the wedge.

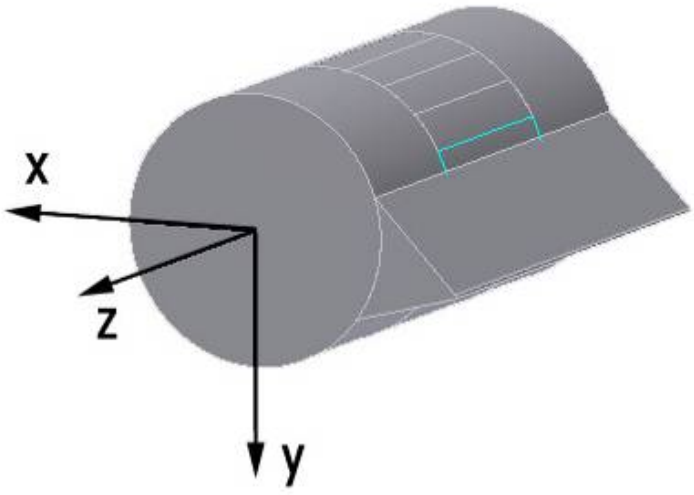

Figure 4.8. Tool with addition of soil wedge representation.

Simulated soil particles were contained in a bin which measured 5 cm wide and 20 cm long. The bin was only as wide as the bar to force soil to flow under and above the bar as it would have occurred at the center of the bar in the soil bin. Soil was filled to 15 cm in the bin and, as with the soil bin experiment, the bar traveled from one end of the bin to the other at a depth of approximately 7.5 cm. The soil consisted of three particle types which represented sand and gravel, silt, and clay particles. In order to recreate the compaction created by the packer wheels in the soil bin, the first 0.5 seconds of the simulation were dedicated to compacting the particles using an increased gravity force (arbitrarily set at $g = 25$ m/s^2).

4.2.3 Model parameters

The soil was represented by three particle types – sand, silt, and clay, with diameters of 4, 2, and 1 mm, respectively. Particle sizes were increased beyond the normal size according to classification systems to limit the total number required in order to control the total simulation time. The size differences relative to the classification system were

not maintained because the classification ranges are different by orders of magnitude. This would have required an extremely large number of clay particles or a very small number of sand particles. Instead, the soil was recreated based on the distribution of particle mass in the soil bin (Section 5.1), with gravel considered as sand as the gravel particles were only slightly larger than the maximum size for sand according to the classification system. Therefore, the mix consisted of 45% sand, 52% silt, and 3% clay by mass. Due to differences in density and size, the number of particles used then became 7% sand, 65% silt, and 28% clay.

Two contact models were employed in the simulation. All contacts were modeled with a linear Hertz-Mindlin contact, assuming no slipping. The data that DEM required to calculate these contacts were the coefficients of restitution, Poisson's ratio, shear modulus, and the particle density (Table 4.1). With the exception of the coefficient of restitution, these parameters were taken from materials databases (aluminum) (Matweb 2009) and lab testing as outlined in Section 5.1. The coefficients of restitution were based on best estimates and altered if the simulated results became unstable (Table 4.2).

Table 4.1. Material parameters for EDEM model taken from lab measurements (soil) and online databases (aluminum) (Matweb 2009).

	Particle Density	Poisson's Ratio	Shear Modulus
	kg/m^3		MPa
Sand	2690	0.25	120
Silt	2650	0.3	100
Clay	2790	0.35	60
Aluminum	2700	0.33	2600

Table 4.2. Matrix of coefficients of restitution used for particle interactions.

	Sand	Silt	Clay	Aluminum
Sand	0.45	0.4	0.2	0.5
Silt	-	0.2	0.1	0.3
Clay	-	-	0.01	0.1

In addition to the linear contact model, a cohesion model was included to represent the effect of moisture in the soil and adhesion of the soil to the tool. The cohesion model acted to add a normal cohesion force to the Hertz-Mindlin contact using,

$$F_c = k_e A, \tag{4.3}$$

where F_c = cohesive force (N),

k_e = energy density (J/m^3 or Pa), and

A = contact area (m^2).

The model was used for particle-particle interactions as well as interactions between the geometries (tool) and the particles. Values for the energy density were also based on best estimates from example files in EDEM and refined until the simulation showed visible indicators of cohesion without creating an unstable system (Table 4.3). The intention was to provide more cohesiveness for interactions involving clay particles and less for those which involved sand.

Table 4.3. Matrix of energy density (kJ/m^3) for particle and geometry interactions.

	Sand	Silt	Clay	Aluminum
Sand	16	18	20	16
Silt	-	18	20	18
Clay	-	-	20	20

CHAPTER 5 RESULTS AND DISCUSSION

5.1 Soil Parameters

Because the soil present in the soil bin was unique and quite different from a typical agricultural soil, tests were performed to determine the properties of this soil. The parameters selected for testing were also required as boundary conditions and input constraints when modeling with DEM. These properties were the grain size distribution, particle density and shear strength parameters including critical angle of friction and shear modulus. The purpose of these tests was not to determine an absolute, definitive measurement of these properties but instead, obtain an initial estimate to be entered into the model.

The nature of the rotary action and continual rolling from the disks in the soil bin also created a unique character of the soil. Silt and clay-sized particles became firmly bound either with each other or by surrounding a sand particle in such a way that new particles were created as a combination of smaller particles. As the soil was continuously and repeatedly rolled by the disks around the bin, these new particles slowly increased in size and became substantially solid and difficult to break apart into their smaller components. As such, some of these tests of soil parameters were conducted with the soil left "as is" with the composite particles intact as well as following a procedure to break them down into their components.

5.1.1 Grain size distribution

A wet sieve analysis following a procedure employing ASTM D422 (ASTM 2007) and ASTM D6913 (ASTM 2005) was conducted to determine the actual particle size

distribution of the soil. By soaking and rinsing the soil through a No. 200 sieve, slowly the silt and clay-sized particles were released from the larger composites to reveal the true grain size distribution of the soil. A hydrometer was then used to determine the proportion of particles smaller than the No. 200 sieve which are clay and silt. Figure 5.1 illustrates this distribution.

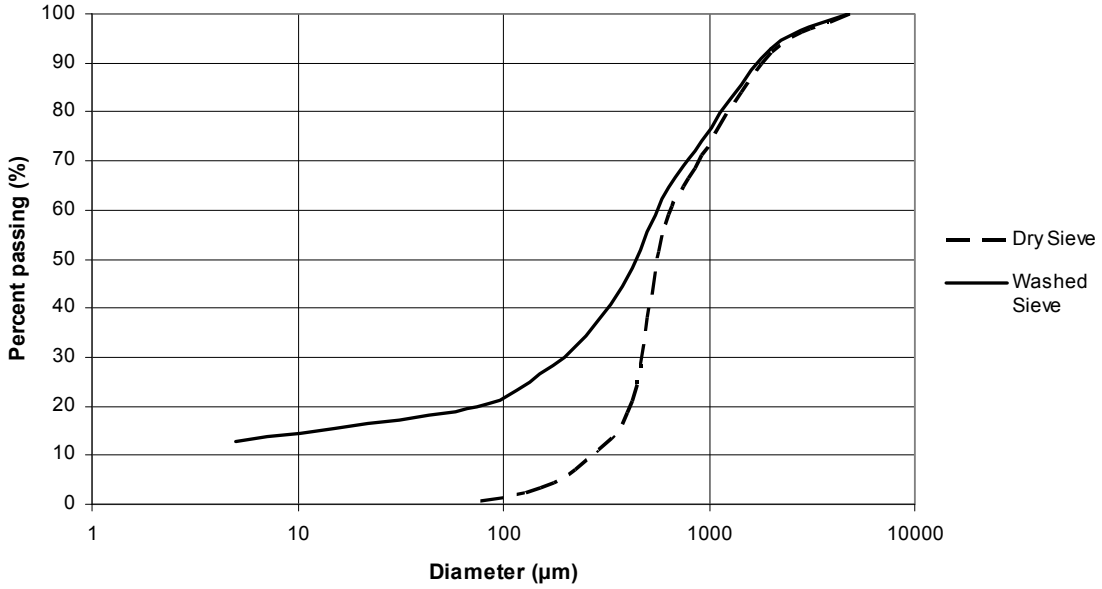

Figure 5.1. Grain size distribution of soil bin soil by washed and dry sieve method.

A dry sieve analysis similar to ASTM D6913 was also performed on the soil to determine the *in situ* distribution which included the large composite particles. The deviation from the method was to omit the washing of the soil to find the proportion of particles smaller than 75 µm. From Figure 5.1 it can be seen that there were fewer particles with a diameter less than 75 µm, which is the upper limit of silt/clay sized particles.

Using the distributions, it is possible to classify the soil. The coefficient of curvature, C_z, and coefficient of uniformity, C_u, can be calculated based on the particle size which corresponds to 10, 30 and 60 % passing from Figure 5.1. The coefficients are given by,

$$C_u = \frac{D_{60}}{D_{10}} \text{ and} \qquad 5.1$$

$$C_z = \frac{(D_{30})^2}{D_{60} D_{10}} \ , \qquad 5.2$$

where C_u = coefficient of uniformity,

C_z = coefficient of curvature, and

D_{10}, D_{30}, D_{60} = diameter at which 10, 30, and 60 percent of particles pass through, respectively.

A coefficient of uniformity close to 1 indicates a very uniform soil with all particles close to the same size. As this number increases, the soil becomes better graded and the curve, similar to Figure 5.1, will flatten, spanning a greater size distribution of particles. The coefficient of curvature describes how uniformly the particles are distributed through the various particle sizes. A small C_z value indicates that the soil is gap-graded which means that there is a certain particle size which is missing. In this case, the curve similar to Figure 5.1 will show a flat spot at the corresponding particle diameter.

The curve of the washed sieve analysis was extended so that a 10% passing diameter could be estimated. Table 5.1 shows these results. The small C_u value for the dry sieve analysis shows that the clay and silt had balled up into particles of a similar size to the sand, reducing the amount of variation present when in actuality the washed sieve analysis showed that there was a large variation in particle size distribution. The low value of curvature coefficient for the dry sieve results indicates that there is a particle size

missing, likely the lack of silt and clay-sized particles. As seen with the washed sieve analysis, the curvature coefficient increased as all particle sizes were present.

Table 5.1. Grading coefficients of *in situ* and actual soil particle distributions.

	Dry Sieve	Washed Sieve
D_{10} (μm)	240	2
D_{30} (μm)	480	200
D_{60} (μm)	620	530
C_u	2.58	265.00
C_z	1.55	37.74

In terms of usefulness for the purpose of modeling, the dry sieve results were more indicative of the conditions present in the wear scenario. Although the actual soil had a large portion of fines, it behaved more like a sandy soil with regard to particle size.

5.1.2 Particle density

By definition, the specific gravity of a soil is the ratio of the particle density to the density of water. As such, determining the specific gravity also provides the particle density because the density of distilled water is 1 g/cm^3. Multiple tests were performed according to ASTM D854 (ASTM 2006) to determine the specific gravity of varying particle sizes and distributions of the soil bin soil.

After sieving the soil using the dry sieve method, the sample was split into three distributions: greater than 595 μm, which generally represented sand and gravel particles, between 150 and 595 μm, which generally represented the composite, balled particles, and less then 150 μm, which generally represented the silt and clay particles. In addition, an overall specific gravity of the soil in unaltered condition was determined. Finally, because the gravel/sand measurement also contained some clay dust which may have

skewed the results, a sample from the wet sieve grading analysis with the same particle sizes was also measured. Table 5.2 summarizes the results of the experiments.

Table 5.2. Calculated particle densities of spectrum of soil particle sizes.

	Particle density (g/cm^3)
Overall	2.65 ± .001
Dry, Uncleaned Sand	2.66 ± .001
Washed Sand	2.69 ± .001
Composite, Balled Particles	2.65 ± .001
Fines	2.79 ± .003

The particle densities were generally very similar, regardless of particle size or composition. Because the overall value was the same as the density of the composite balls, it suggested that the overall soil was dominated by the properties of the balls. There was some discrepancy between the washed and dry sand, but it is likely this difference was only due to measurement error, and the effect of the clay dust was minimal as the inclusion of clay dust, which had a high density, would have increased the particle density of the dry, uncleaned sand. Of particular interest was the density of the fines. Generally, soils have particle densities between 2.65 and 2.70 g/cm^3. The density of fines, 2.79 g/cm^3, was significantly higher than would be initially assumed.

5.1.3 Friction and shear strength

Frictional properties were determined using a direct shear box test according to ASTM 3080 (ASTM 2004). A 5-cm by 5-cm by 5-cm box was filled with soil in the unaltered condition at about 1% moisture content. Three tests were conducted with normal loads of 52.6, 91.8 and 170.3 kPa. Data on the shear force, shear displacement, and normal displacement were calculated and Figure 5.2 was developed. The slope of the residual shear stresses to the normal stress is the tangent of the critical angle of friction,

namely 32.1 degrees. The difference between this angle and the angle created by maximum shear stress values is the dilation angle of the soil. An angle of 2.1 degrees was determined to be the dilation angle which indicated that a very small amount of dilation occurs in this soil.

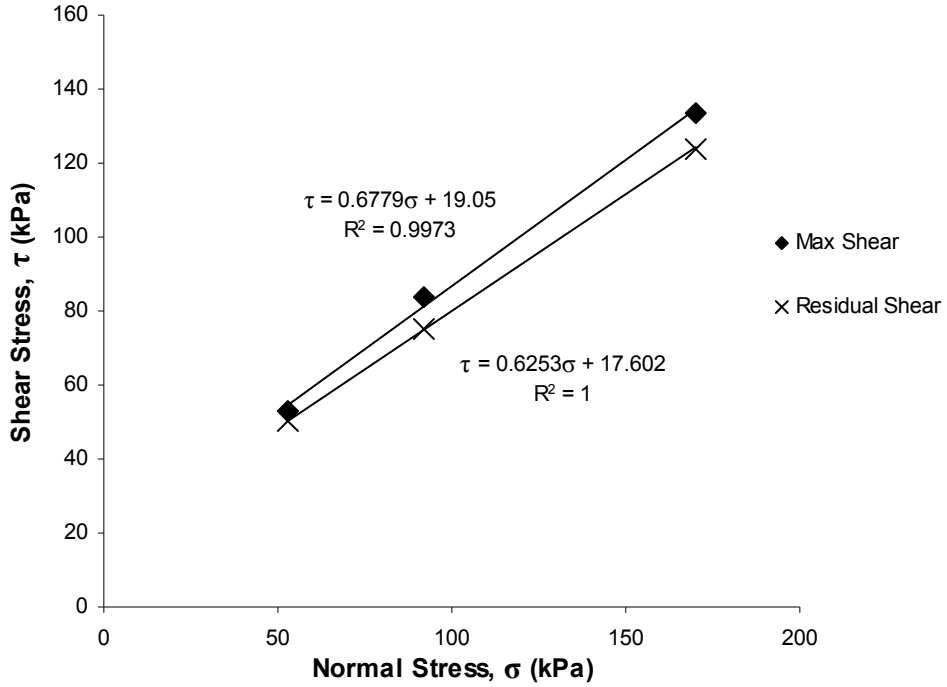

Figure 5.2. Plot of normal stress, σ and shear stress, τ to determine critical angle of friction and dilation angle.

The purpose of performing the tests on normal and shear stress of the soil was to determine the friction angle of the soil, but the cohesion of the soil can also be estimated from the same data. According to the Coulomb criterion, based on Mohr-Coulomb failure theory, the relationship between maximum shear stress and normal shear stress can be expressed as,

$$\tau = c' + \sigma \tan \phi, \qquad 5.3$$

where τ = maximum shear stress (kPa),

σ = normal stress (kPa),

c' = cohesion (kPa), and

ϕ = internal angle of friction (degrees).

Cohesion is a function of soil texture, particularly clay content, and moisture content. Because the moisture content of the samples used in creating the curves in Figure 5.2 was not the same as the soil during the wear tests, the cohesion values estimated from the regression equations may not accurately represent the cohesion present in the soil. The value of 19 kPa taken from the regression of the maximum shear plot provides only an estimate as to the amount of cohesion in the soil bin soil.

The ASTM 3080 standard does not cover the calculation of shear modulus because the stresses and displacements are non-uniformly distributed and the appropriate height cannot be determined. However, an estimation from the values obtained can be determined.

To calculate the shear modulus of the soil, the shear stress values were plotted against shear strain values at each of the three normal stress increments. Strain values were approximated from the height of the shear box even though the actual height may have differed.

The slope of the linear portion of the curve gave the shear modulus. As shown in Table 5.3, shear modulus varied significantly between tests but on average, was assumed to be approximately 4150 kPa for this soil.

Table 5.3. Calculated shear modulus values from direct shear box tests.

	Normal Force	Shear Modulus
	kPa	kPa
	52.6	3595.8
	91.8	4570.6
	170.3	4290.1
Average		4152.2

5.2 Soil Bin Experiment

Each of the six bars exhibited visible wear following 400 km of travel. Visual inspection showed that wear was concentrated at two particular locations around the circumference of the bar. Along the leading edge (defined as 0 degrees), the bar was still in its original state and completely unaffected by wear. This phenomenon could be confirmed from the state of the bar in the soil just prior to removal from the soil bin (Figure 5.3). The leading edge of the bar was covered with a layer of soil, thereby protecting the bar from abrasion.

Figure 5.3. Soil formation after completion of a run.

This was also the cause of the difference between the straight wear scar edge at the back side of the bar and the jagged surface at the leading edge of the scar (Figure 5.4).

Because the soil stuck to slightly different areas on the bar with each run, the shape of the wear scar changed (Figure 5.5) and layers of wear could be seen.

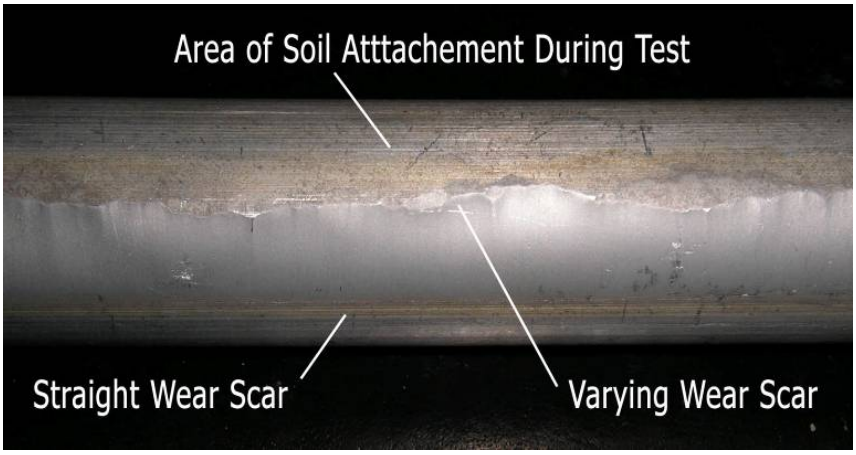

Figure 5.4. Variance in soil attachment created an uneven wear edge as seen from the bottom of the specimen (90 degrees).

Figure 5.5. Wear scar layering caused by differences in soil attachment over a set of runs.

It was also noted that the steel bars were affected by corrosion as well as abrasion. When cleaning the bars before measurement, the soil was easily removed from the aluminum bars but was firmly attached to the steel. Due to the moist soil and lack of

movement where the soil stuck to the bar, small amounts of rust began to form at the edges of the wear scar (Figure 5.6).

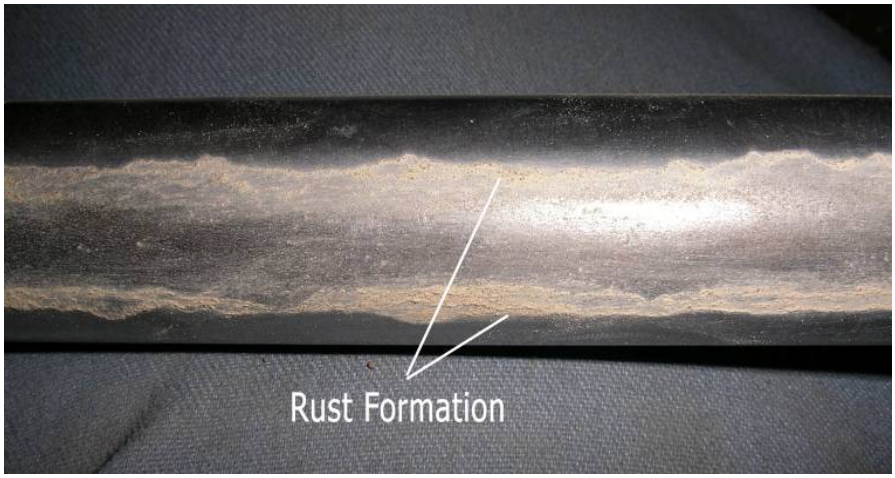

Figure 5.6. Rust formation at edge of wear scar.

5.2.1 Mass/volume change

Mass data were collected at each 50-km interval. Volume loss was then determined using the material density. Although mass data were very similar initially, with approximately 1 g of material removed at each interval, the difference in densities proved obvious when volume loss was considered (Figure 5.7). The general trend appears to be exponential for the aluminum as the rate of wear increased with each measurement. For the steel, volume loss remained quite consistent which may be a result of the low wear rate. It could be assumed that the exponential type wear would also occur on the steel in the future but over the interval of study, this level of wear was not yet reached.

Over the entire exposed area of the bar, the aluminum lost approximately 6.5 cm^3 while only about 1.1 cm^3 was removed from the steel after 400 km of travel.

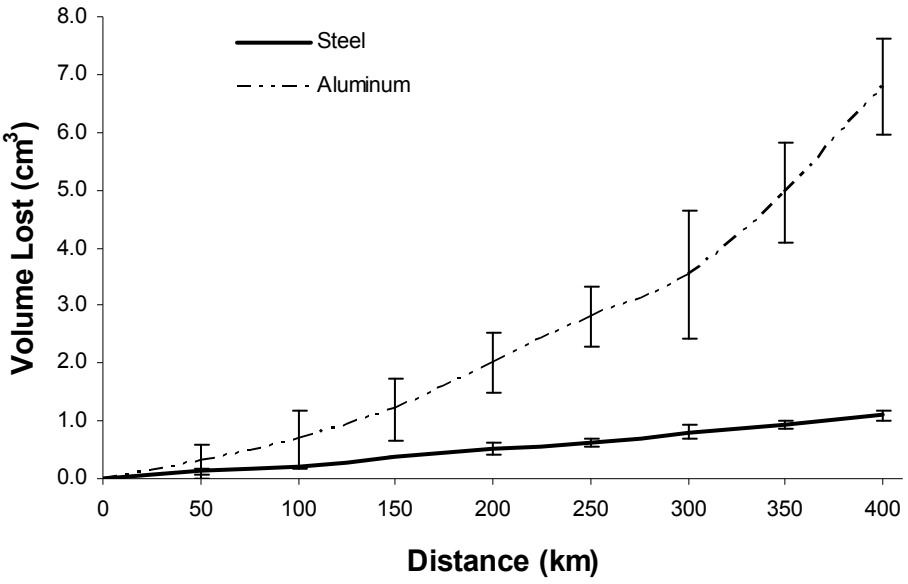

Figure 5.7. Average and standard deviation (shown by error bars) of volume lost calculated from mass change.

5.2.2 Tool profile

Tool profile was determined from measuring the radius of the bars at multiple locations around its circumference. By plotting these radii, the change in shape of the profile was studied and the level of wear was quantified.

Verification of CMM results

Because the specimens were mounted at their extremes while being pulled through the soil medium, it was possible that the bars could have bent as a result of the draft forces. As the CMM also used the ends of the bar for generating the reference axes, a change in the central axis at the center of the bar would not have been recognized. Bending would have skewed the radius measurements by indicating wear had occurred when the change in measurement was actually due to a change in the central axis of the

bar at the point of measurement. To eliminate potential error that may have been present in the CMM data before analysis was complete, separate tests were done to ensure this bending did not occur.

If bending was to have occurred, the radii data would indicate an increase in radius at the 180-degree location. Because this location is at the back and it has been established in trial runs using a painted bar that wear did not occur at this location, any change in this measurement would indicate bending rather than radius change.

As an example, Figure 5.8 shows a plot of the bar radius at the 180-degree measurement for bar AS1 against the 8 measurement intervals. A trendline and associated equation present the size and direction of change in this measurement. From this figure, it can be seen that the trendlines were nearly horizontal and the slopes were on the order of magnitude of ten thousandths of a millimetre per measurement (converted from mm/50 km where 1 measurement = 50 km). This value is smaller than the resolution of the CMM (± 0.003 mm) and the sign of the slope should be positive for the bar to be bending. Table 5.4 provides complete data for all the specimens tested.

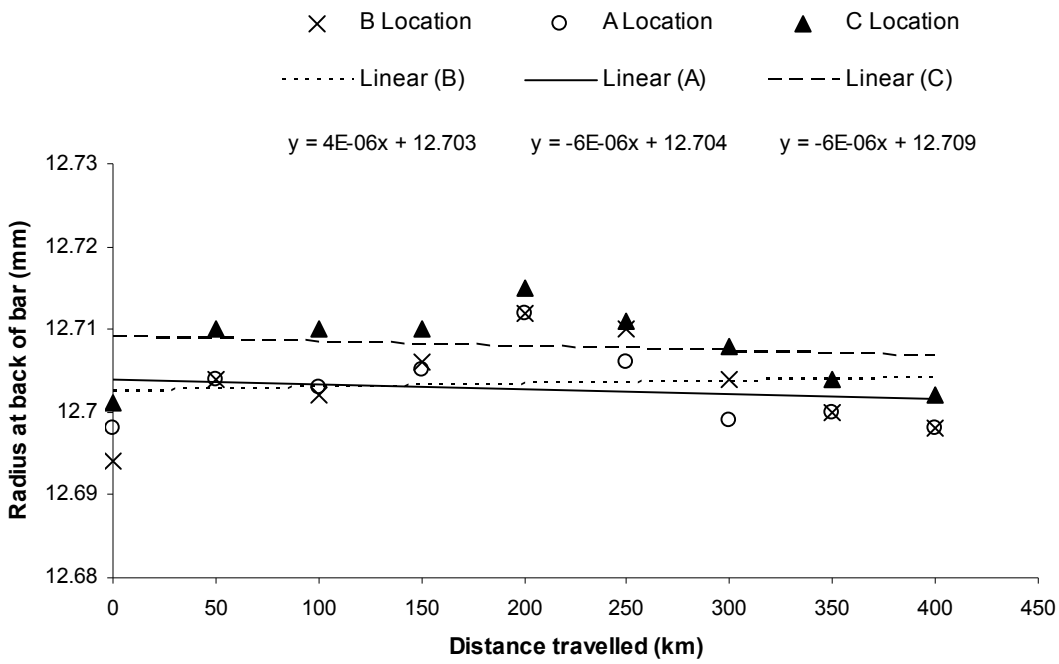

Figure 5.8. Example of methodology performed on an aluminum bar to determine amount of bend.

Table 5.4. Test for bending data for each replication of steel (AS) and aluminum (AA).

Replication	Measurement Location	Change in Radius per Measurement μm/meas.	Range μm	Min/Max Measurement km
AS1	B	0.20	18.03	0 / 200
	A	-0.30	14.01	400 / 200
	C	-0.30	14.00	0 / 200
AS2	B	0.05	14.01	0 / 250
	A	0.10	12.98	0 / 250
	C	0.08	13.99	0 / 250
AS3	B	0.02	19.03	200 / 250
	A	-0.10	17.01	200 / 250
	C	-0.30	15.01	200 / 250
AA1	B	-1.60	21.04	200 / 150
	A	-1.70	17.00	200 / 0
	C	-1.30	19.01	200 / 150
AA2	B	-0.01	21.01	200 / 300
	A	-0.30	16.00	200 / 150
	C	-0.30	22.01	200 / 150
AA3	B	-2.10	23.03	200 / 0
	A	-1.70	25.00	200 / 50
	C	-1.80	28.01	200 / 150

Table 5.4 shows the change in radius per measurement for each bar. More variation was present in the aluminum bars, but due to the negative change in radius per measurement, it is likely that these results are not due to bending. A gradual increase in the radius at the back of the bar would indicate the bar was bending over time and thus a positive value would be obtained.

The range data give the difference between the maximum and minimum measurement for that bar at the specified measurement location, as well as the measurement interval at which the maximum and minimum occurred. For bending to have taken place, the 180 degree measurement would have steadily increased such that the minimum measurement would be at 0 km and the maximum at 400 km. Because of the random nature of the min/max locations and the fact that the minimum occurs after the maximum (indicating

the bar 'un-bent'), it can be inferred that bending did not occur. The randomness of the minimum and maximum values can be attributed to random error in the CMM measurement process. This can be confirmed by the very small change in radius per measurement (on the order of 0.1 μm) which is less than the accuracy of the CMM (± 3 μm).

Change in tool radius

From the x-y coordinates provided by the CMM, changes in radii could be analyzed. Figure 5.9 illustrates the locations of wear on the bar. The upper and lower front surfaces experienced the majority of the wear.

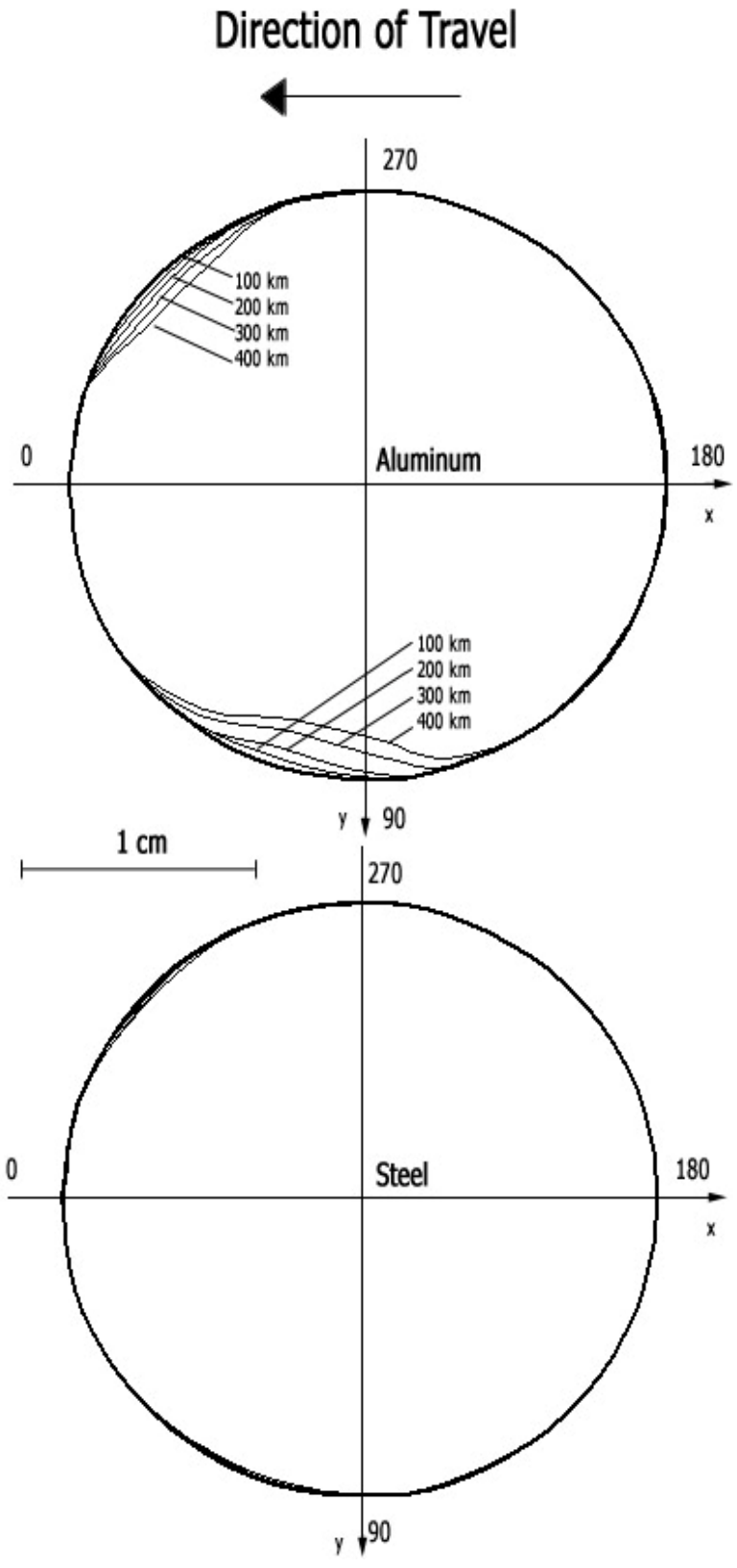

Figure 5.9. Wear profile of steel and aluminum bars at 100 km intervals.

When plotted as a function of the measurement angle, Figure. 5.10 illustrates that wear was concentrated at about the 72 and 324-degree marks. While most of the bar did not wear, the wear measurement came to a distinct maximum which indicates that material was not removed evenly from the entire surface. Instead, as is seen in Figure 5.9, a segment of the profile was worn. Of the two wearing regions on the aluminum bars, the area at 72 degrees experienced more wear as it was located on the lower edge of the profile where higher soil pressures would exist. Soil could easily flow above the bar but at the lower edge, compaction was required to allow the bar to pass through the soil. This extra pressure increased the abrasive wear. It is possible that the low wear rate for steel was unable to capture this phenomenon. As with the mass/volume change data, the trends of steel wear may have become more like that of aluminum if the steel tool was allowed to wear further.

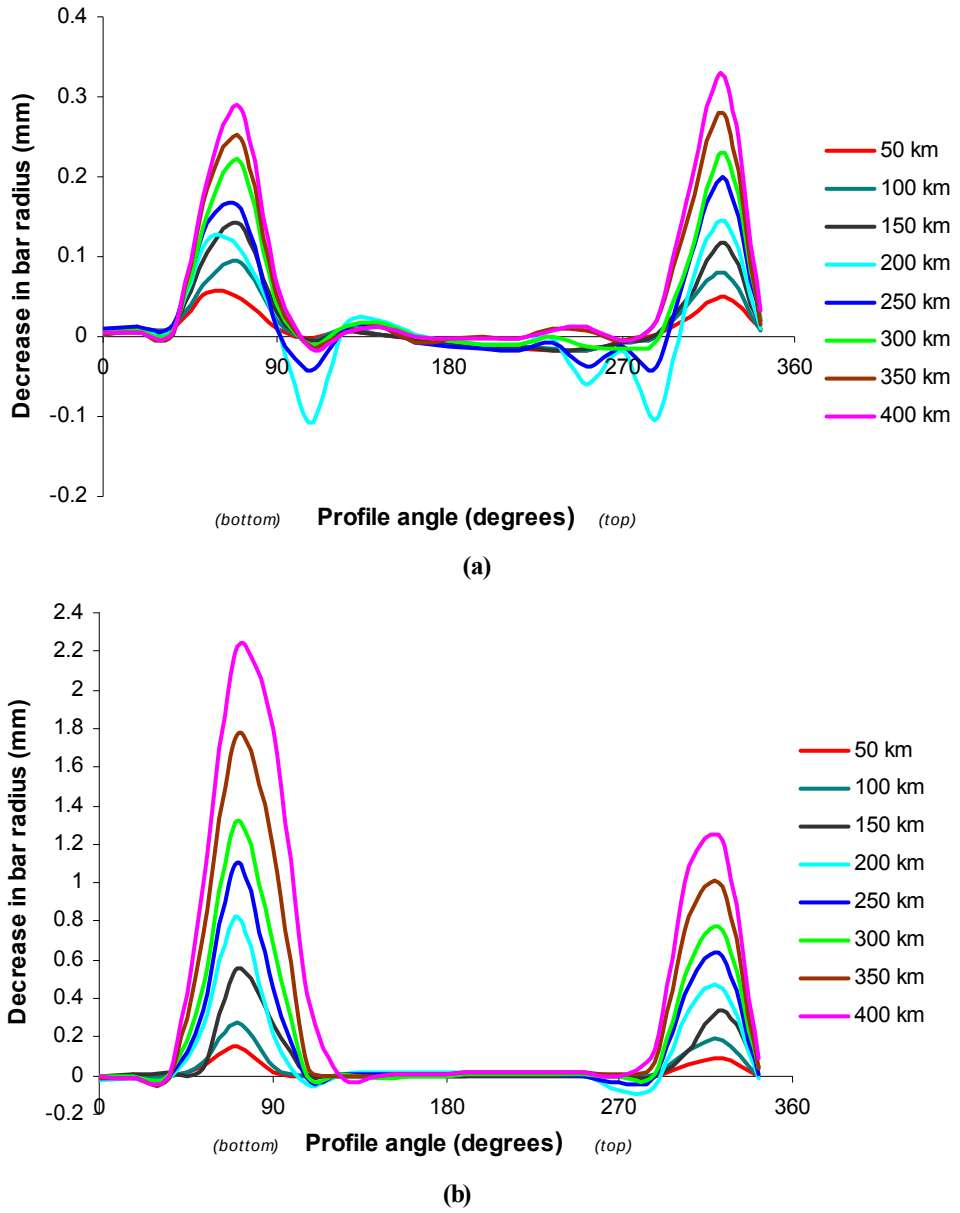

Figure 5.10. Cumulative radius change as a function of angle of measurement for (a) steel and (b) aluminum.

One anomaly which is particularly obvious on the steel bar plot for the 200-km and 250-km measurements are the increases in radius (negative decrease). Physically, this indicates that the bar grew in size which is not possible. As was seen in Figure 5.6, this may be due to the rust formation at the edge of the wear scar. As moist soil collected in

this area it built up a very hard ridge which may have resulted in the CMM reading that the bar had an increase in radius. Other possible explanations could have been the sensitivity of the CMM's measurement or that another process was taking place such as plastic deformation without material removal.

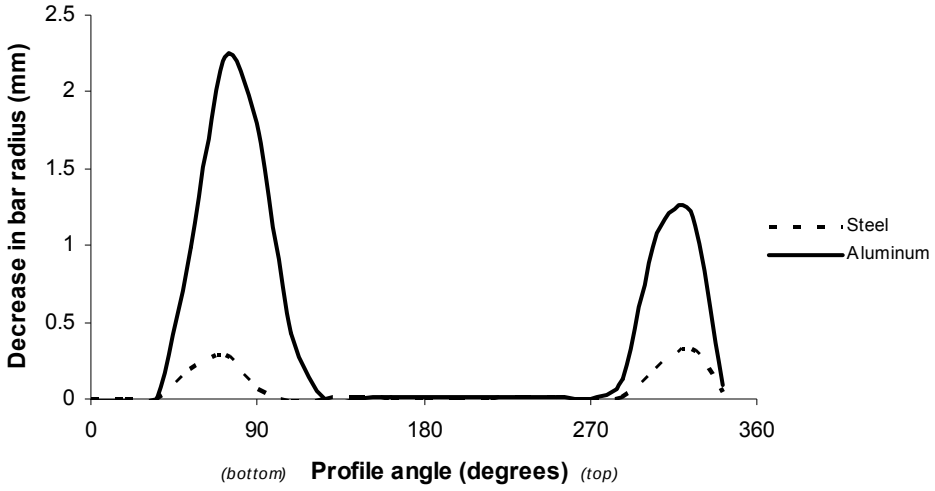

Figure 5.11. Comparison of final radius change of aluminum and steel.

As expected, the aluminum bars had the greatest reduction in radius. At the point of maximum wear, the radius of the aluminum bar was reduced by about 2.2 mm, while the steel bars lost less than 0.35 mm (Figure 5.11). When comparing the two materials, both exhibited similar characteristics. The locations experiencing large amounts of wear were very similar but the aluminum showed much greater wear at the bottom location while the steel had similar radius change at the bottom and top wear locations.

Wear profile change

As seen in Figure 5.9, wear did not occur consistently over the entire profile. Wear occurred at distinct locations, but the way in which these wear spots progressed was also different. Assuming the wear spot to be a straight line segment (Figure 5.12), the angle

of this segment relative to the horizontal changed as a function of the wear distance. The implication of this change is a variation in the soil pressure across the tool.

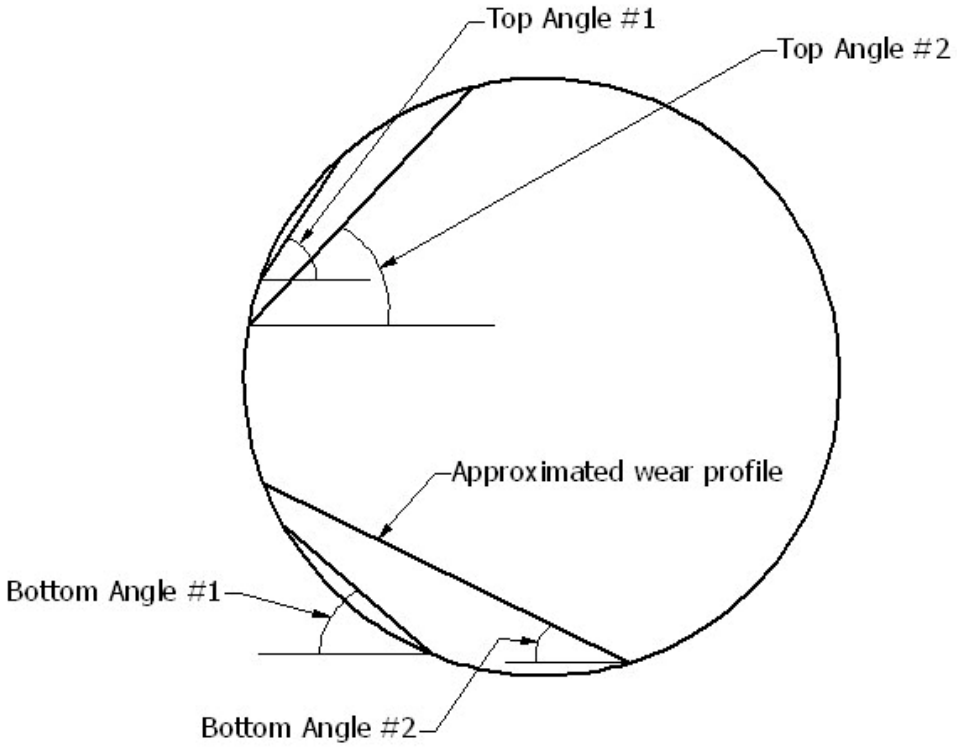

Figure 5.12. Schematic of wear angle calculation.

The wear spot angle was determined from first approximating the wear profile as a straight line from the x-, y-coordinates of two locations from the CMM measurements. The angle they created was plotted against the distance traveled for the bottom wear spot in Figure 5.13 and the top wear spot in Figure 5.14.

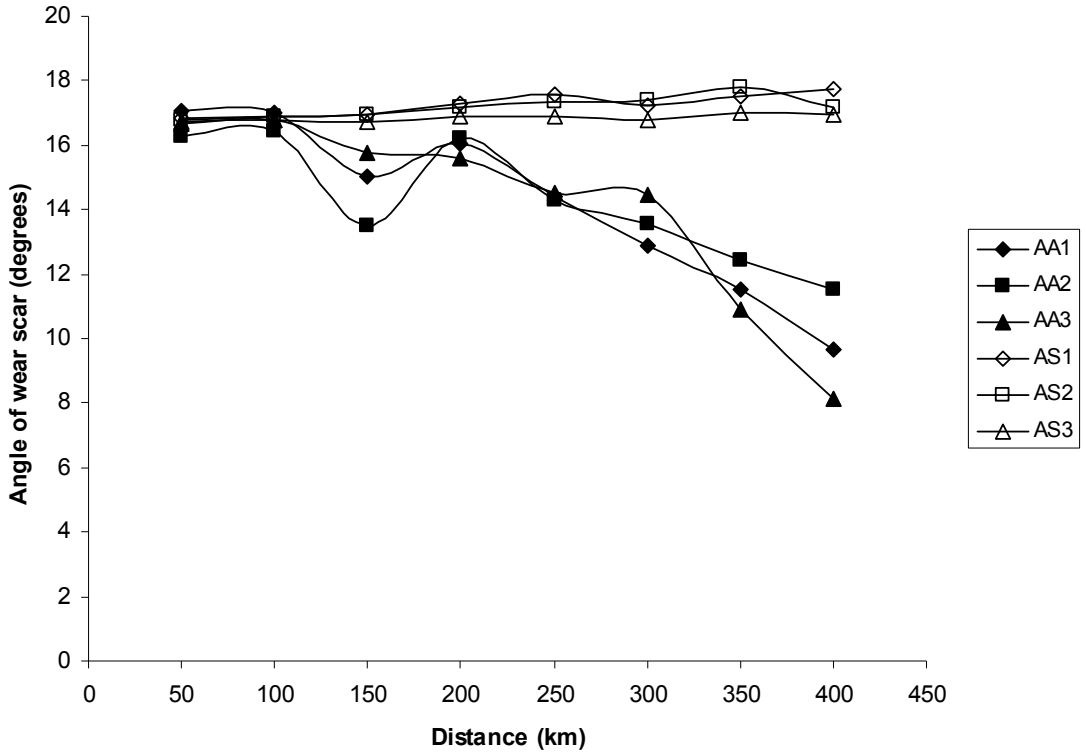

Figure 5.13. Angle of wear scar near the 72 degree location (bottom) for three aluminum (AA) and three steel (AS) bars.

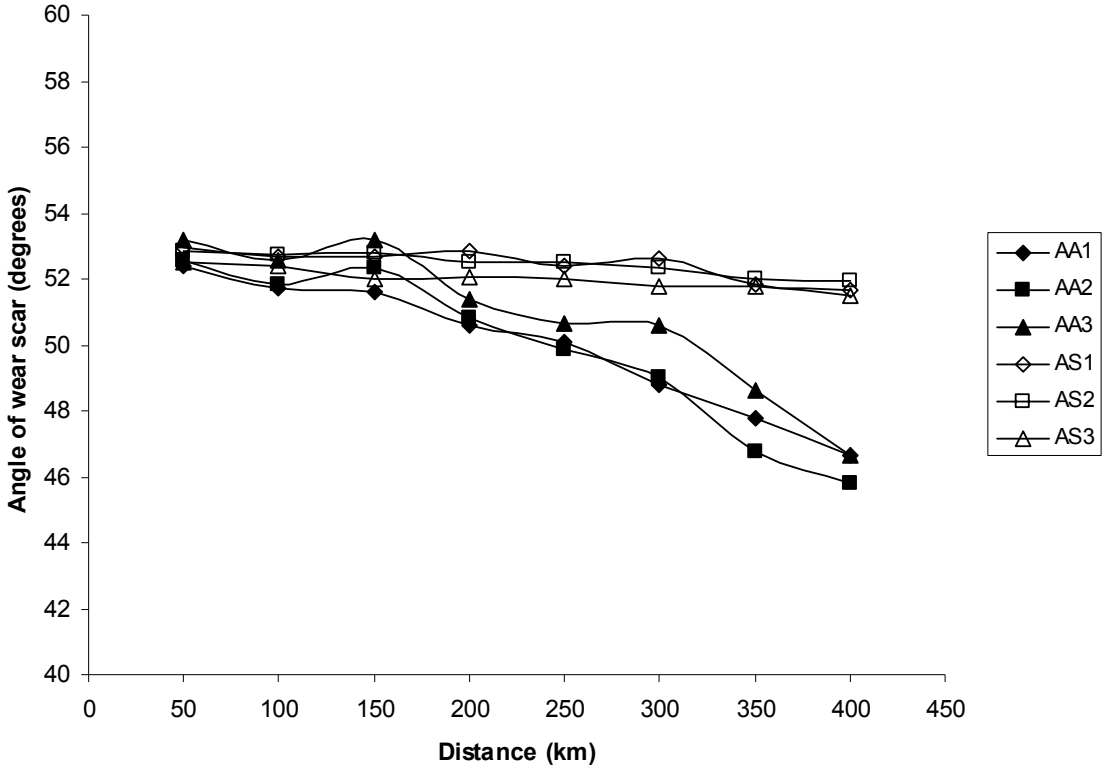

Figure 5.14. Angle of wear scar near the 288 degree location (top) for three aluminum (AA) and three steel (AS) bars.

Aluminum saw the greatest change in angle as it also experienced the most wear. Because both steel and aluminum initially showed a very similar wear angle, it can be assumed that further wear of the steel would also create a similar trend as to that shown for aluminum. As wearing distance increased, the wear angle approached horizontal at the top and the bottom which would act to minimize the differential in soil pressure along the top and bottom side of the tool.

The variation from the trend for aluminum at the 150-km measurement is interesting to note. Because the bottom appeared to extenuate the angle and the top reversed the change, it may indicate a problem with the CMM measurements such as a misalignment rather than an event which occurred during the test.

5.3 DEM Simulation

After considerable debugging and trial-and-error processes to determine appropriate input parameters, the set of simulations were run over a period of one month. The total simulated time was 0.6 seconds. The first 0.5 s were used only to settle the particles into the bin with an elevated gravity force. This interval took approximately 48 hr to simulate and was only completed once. All the remaining simulations with each bar shape were started at the 0.5 s point in the simulation. Not only did this save many hours of simulation time, but it also ensured every simulation was run with the identical initial conditions in terms of soil preparation. Figure 5.15 is a screenshot of the software with the tool passing through the soil.

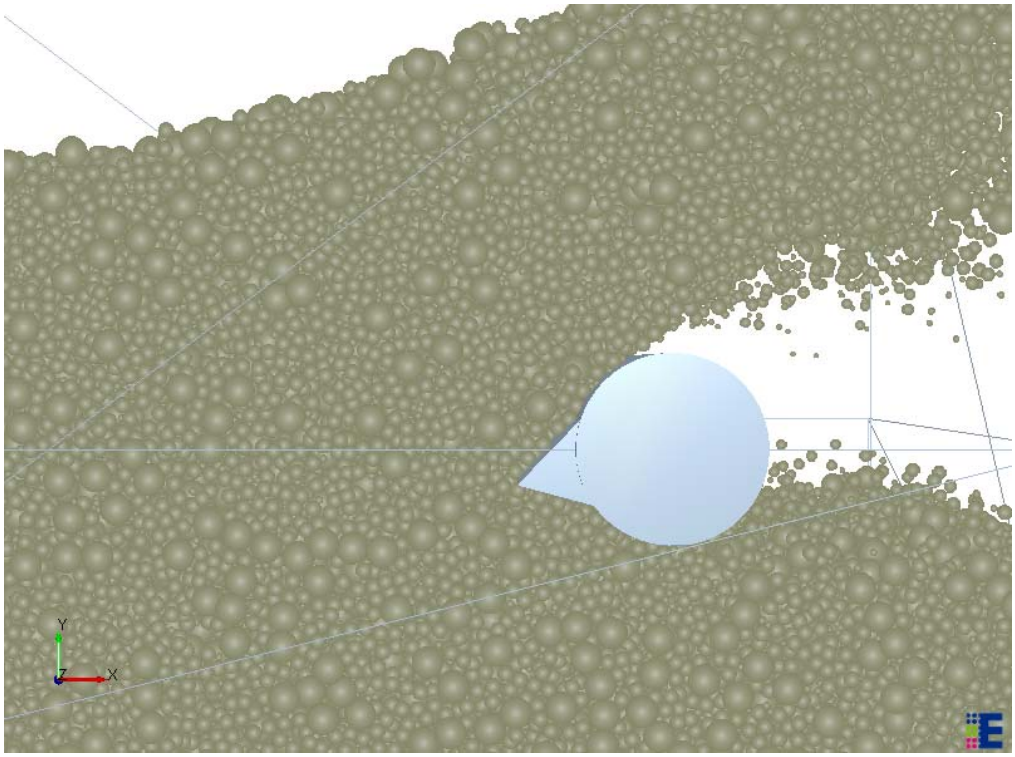

Figure 5.15. Screenshot of simulation on initial bar shape.

During the 0.1-s simulation interval where the bars were moved through the bin of soil particles, measurements of total compressive force and relative tangential velocity of

soil particles were recorded every 0.005 sec creating 20 data points in each simulation. Tangential velocity of soil particles moving over the bar was determined for interactions between each of the soil particle types and the bar. For a given measurement, the particle type with the highest relative velocity was selected. This eliminated any contribution of particles that did not make contact with the bar which would have shown a relative velocity of zero.

Of the 20 compressive force and relative velocity measurements, an average value was used from the 14 values in the middle of the interval to give a single value of compressive force and tangential velocity for the simulation at each of the bar sectors. Matching the force and velocity values with the actual measured wear from the same bar, sector, and 50-km soil bin wear interval, a relationship could be determined. Figure 5.16 illustrates the recorded compressive force and tangential velocity values for the bar in its initial shape as a function of profile angle. It can be seen that both distributions show similarities to the measured wear magnitude in Figures 5.10 and 5.11. As expected, the relative velocities were similar at the top and bottom of the bar due to the symmetry of the tool. The compressive force was also as expected as higher forces were predicted on the bottom half of the tool. At the bottom of the tool the soil must be forced and compressed to pass under the bar, creating higher compressive forces, but could freely pass over the top.

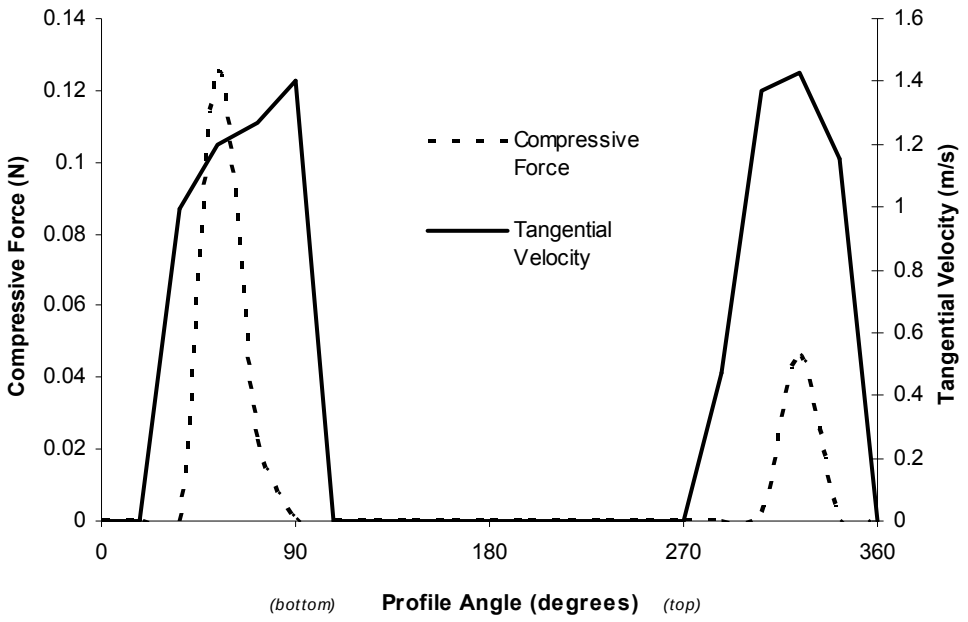

Figure 5.16. Distribution of simulated compressive forces and tangential velocities on the bar profile.

5.3.1 Model development

According to the Archard Equation (Eq. 4.1), the initial relationship which was attempted between wear and the compressive force and relative tangential velocity data was a linear regression,

$$W = kFv \ , \qquad 5.4$$

where W = measured soil bin wear rate (mm of radius reduction/50-km of travel),

F = simulated compressive force (N),

v = simulated relative tangential velocity (m/s), and

k = constant of proportionality.

The product of force and velocity ('wear product') was plotted against the measured soil bin wear rate and a regression was preformed using Microsoft Excel (Figure 5.17). Upon inspection, the non-zero y-intercept was not as expected. Even though there are a

conglomerate of points at (0,0), the remaining data were so scattered that the fitted line did not pass through the origin. Although correlation was poor ($r^2 = 0.07$), this exercise did highlight a separate issue.

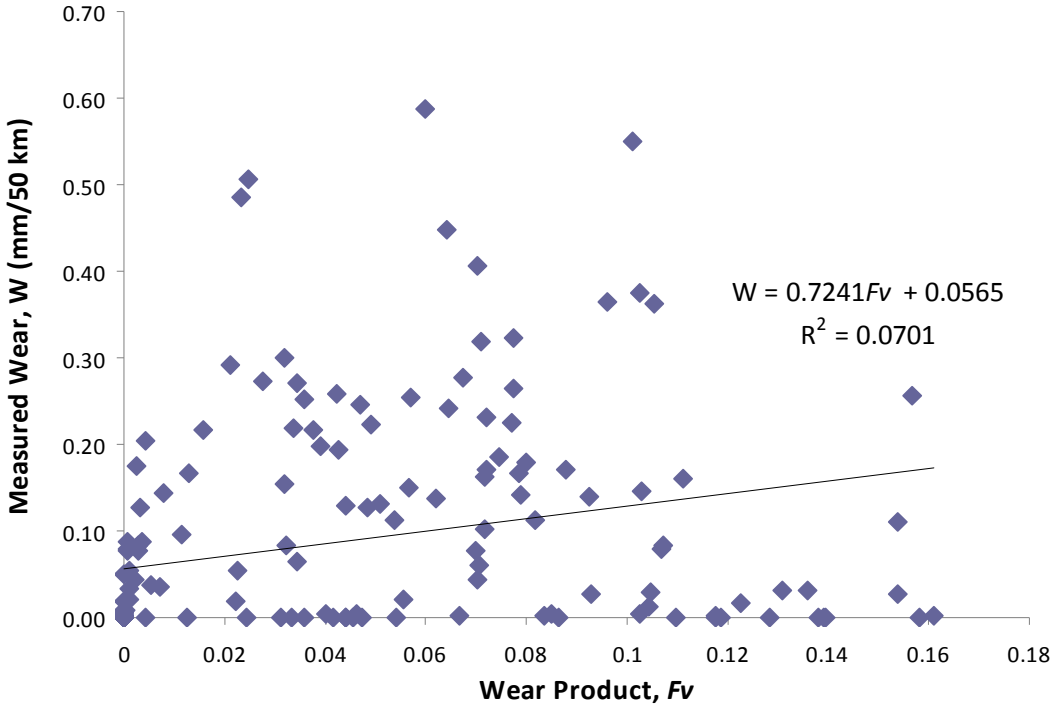

Figure 5.17. Linear regression of measured wear, W, and wear product, *Fv*.

A significant number of data points were found on the horizontal axis which indicated that a compressive force and relative velocity were predicted at locations or instances where no wear was actually measured in the soil bin trials. Upon further inspection, it was discovered that these points were all from data measured at the 342 and 36 degree segments on the bar. The reason for this occurrence was the difference in the measurement method for this comparative data. Segments 342 and 36 were positioned on the edge of the soil wedge such that a portion was covered by the wedge and a portion was exposed to the soil. It is likely that the single location where the CMM measured the radius change, located at the center of the segment, was protected by the wedge and did

not wear. However, in the simulation, force and relative velocity data were determined from an average over the entire sector – part of which was exposed to the soil and therefore recorded a force and relative velocity. Assuming these edge effects were a limitation of the regression and removing these data points, the coefficient of determination increased to $r^2 = 0.29$ and the y-intercept moved closer to zero following a repeated analysis.

It was possible that a linear relationship did not best fit the collected data. A second equation was fit to the data which modified the Archard relationship to account for any difference in contribution of one of the wear product elements relative to the other. The relationship was modified to,

$$W = kF^b v^c, \qquad 5.5$$

where W = measured soil bin wear rate (mm of radius reduction/50 km of travel),

F = simulated compressive force (N),

v = simulated relative tangential velocity (m/s),

k = constant of proportionality, and

b,c = weighting constants.

Constants were determined from the application of a non-linear regression process using SAS v. 9.1 software (Cary, NC). The regression iterated through the constants using the Gauss-Newton method to reduce the sum of squared error. The process also completed an F-test to determine the significance of the constants (i.e. how much of the variation is accounted for by the model). The result showed a highly significant fit ($p<.0001$) with values of $k = 0.1059$, $b = 0.1563$, and $c = 2.3329$ for the constants in Equation 5.5.

To verify this equation to other collected data, compressive force and relative tangential velocity data were collected for simulations based on the third aluminum bar tested in the soil bin. Using the relationship, wear could be predicted based on these two parameters. Figure 5.18 shows the correlation between the predicted wear using the relationship and the actual wear measured for bar three. Deviation from the 1:1 line indicates differences between the actual and predicted wear rates.

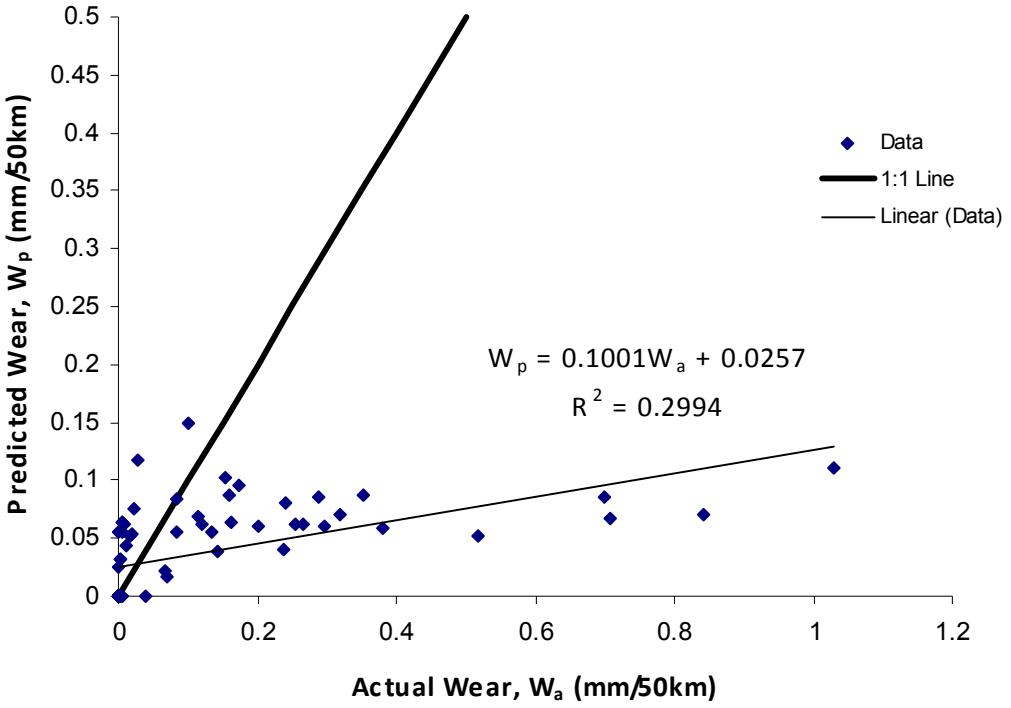

Figure 5.18. Correlation between predicted wear, W_p, and actual measured wear, W_a, for bar AA3.

There were significant variations as the model tended to underestimate the actual amount of wear. The slope of the regression line for the data was near 0.1 which is significantly lower than the ideal slope of 1.

The likely reason for the poor correlation of the model and the actual wear was the way in which bar AA3 wore in the soil bin. Wear rates were initially much lower compared to bars AA1 and AA2 and yet, by the conclusion of the tests, all three bars had worn very similarly. This means that at some point, wear rates were very large and this could account for the underestimation of the model as certain actual wear rates were abnormally high. Evidence of these differences in wear rates can be seen in Figures 5.13 and 5.14 as the angle of the wear scar for AA3 changes little initially but shows a greater slope than bars AA1 and AA2 near the end of the tests.

In order to prove the true potential for the model, data for bar AA3 were excluded for verification. Rather, the relationship was generated using only data from AA1 and verification was performed with AA2 data (Figure 5.19). The equation fitting using only data from bar AA1 to Equation 5.5 produced constants of $k = 0.129$, $b = 0.1534$ and $c = 1.8928$. Although correlation to actual wear values was still low, it was drastically improved over Figure 5.17.

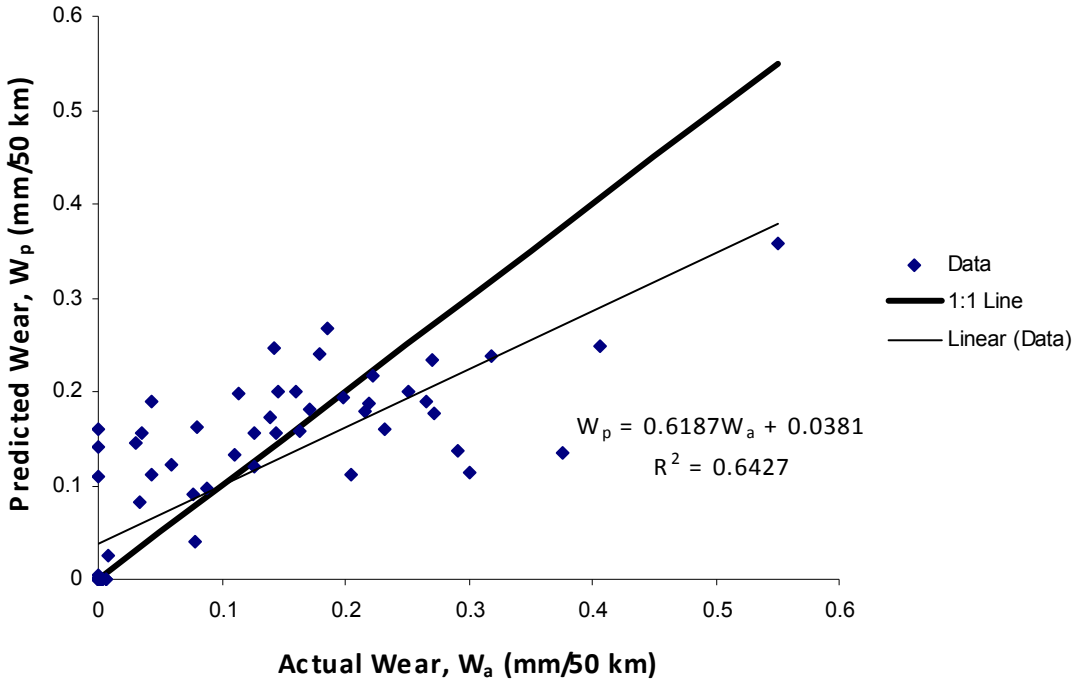

Figure 5.19. Improved correlation of model by excluding AA3 data.

Because of irregular data recorded by the CMM for the actual wear of the bars in the soil bin, outliers exist such as the incidences of zero measured wear with a non-zero predicted wear. Uneven wear rates also created the points to the right where sporadic large wear rates were recorded. However, there does appear to be some relationship in the data as the trend of the predicted wear is clustered around the 1:1 line of correlation.

Attempted improvements to the model included the addition of an intercept for all non-zero predicted wear and the refining of data to remove potential outliers. The result of these regressions showed no improvement over the relationship shown in Figure 5.19. Details of these analyses can be found in Appendix D.

5.3.2 Simulation results verification

The interactions which occurred in the simulation were constantly in flux. Prediction of parameters was completed by sampling this dynamic process in order to infer the mean. Because the limitations of computing power required the use of a small soil bin and a short simulated time, sampling could only take place over a short period of time. As such, the amount of variation present could have affected the predicted mean which, in turn, may have affected the model. The other potential issue is the lack of experimental compressive force data to compare with the predicted values determined by the simulation. With the addition of extended simulation force data, it is possible to gain insight into the results previously obtained. Similar trends in the compressive force predictions of multiple simulations would give greater confidence that the force values collected were representative of the conditions occurring in the soil bin.

To determine the impact of simulation duration, a simulation was performed with a bin three times as long which then required tripling the simulated time in the bin (Figure 5.20). The second related investigation was to "move" the soil past the tool continuously, rather than moving the tool in a bin of finite length. The continuous soil bin was based on the design of Martin Roberge (M. Roberge, Sr. Project Engineer, Digital Prototyping and Simulation, CNH Canada, Ltd. Saskatoon, SK) whereby particles were continually generated and transported via a conveyor at the given speed towards a stationary tool (Figure 5.21). Again, as computing power and time were limiting factors, a single simulation was executed, but three replications of the bar in its initial state were run simultaneously (one beside the next). Three profiles of compressive force data were

collected for comparison to the original force data in a manner similar to that done for the longer bin. The continuous simulation was executed for 40 seconds.

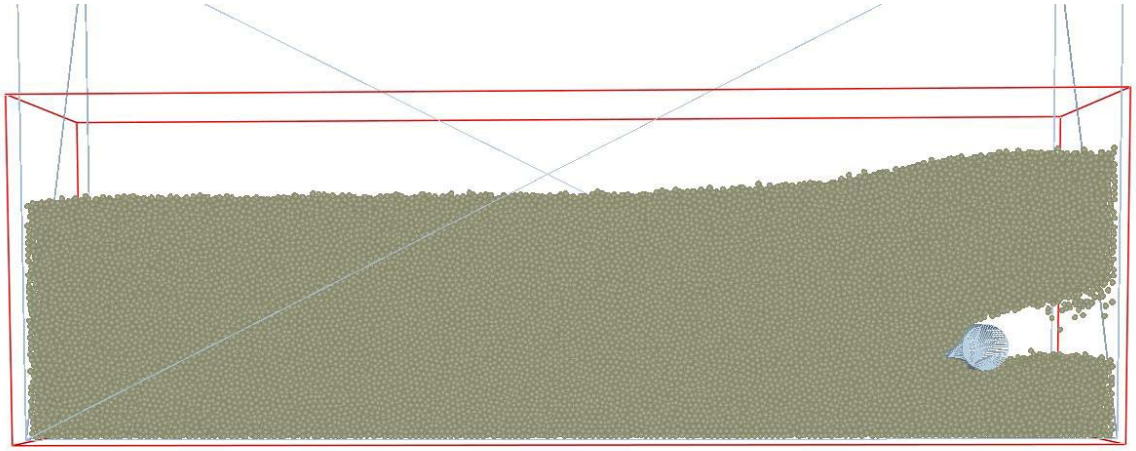

Figure 5.20. Screenshot of simulated soil bin which was three times longer than the original bin.

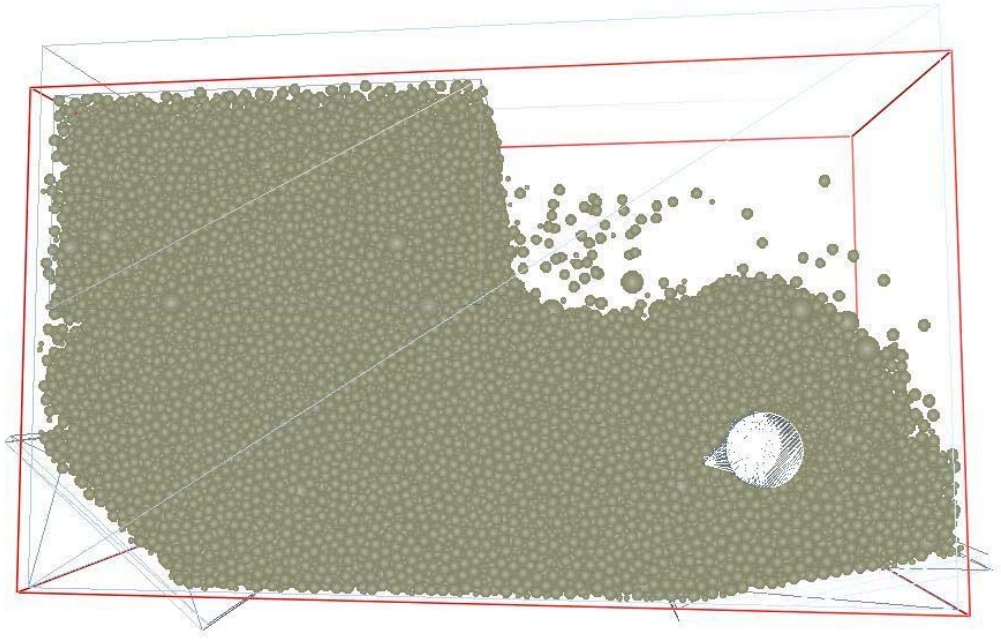

Figure 5.21. Screenshot of continuous bin simulation with a continual feed of particles to a set of stationary bars.

The goal was to determine whether the coefficient of variation for the normal force variable changed as a result of increasing the simulation duration. Figure 5.22 gives the coefficient of variation for the force data when comparing the initial bar shape in the long bin, the three replicates in the continuous bin simulation, and the original short soil bin. Little effect of increasing the soil bin length can be seen on the variation of the data. The cause of the large differences in some of the data can be explained by the magnitudes of the force data, shown in Figure 5.23. Non-zero force was recorded at the 288-degree segment in the long bin and continuous bin while none was predicted for the shorter bin. A zero force prediction indicates that no contacts were made between the particles and the tool. In the short bin, it is likely that no contacts were made at the exact moment of sampling. In the longer simulations, a higher sampling rate was able to capture the infrequent occurrence of an interaction at this bar location. Because the average compressive force was zero for the short bin, there was also no variation.

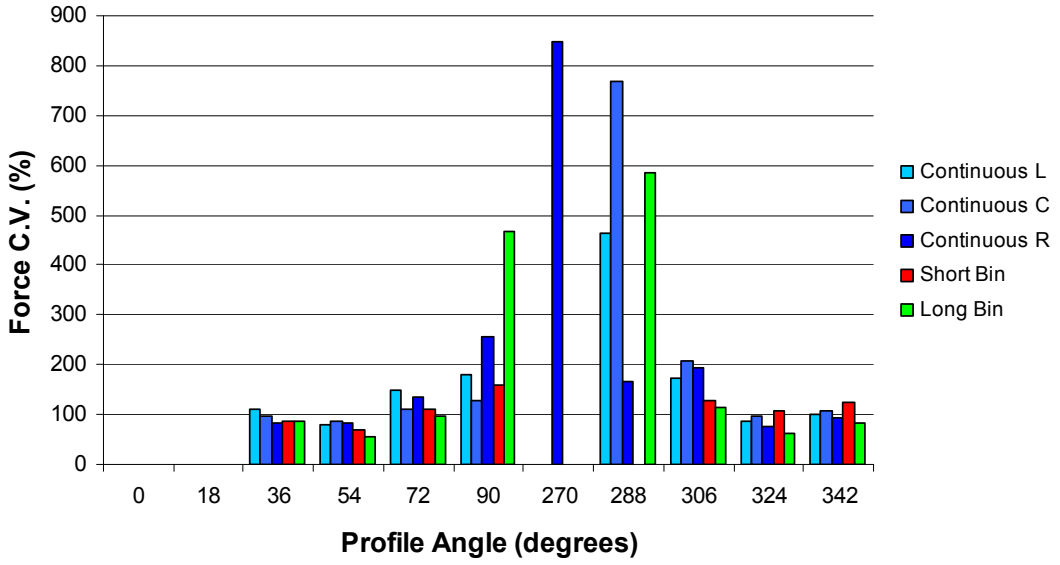

Figure 5.22. Coefficient of variation of force measurements in the longer soil bin and the left (Continuous L), right (Continuous R), and center (Continuous C), measurements in the continuous bin compared to the original shorter bin.

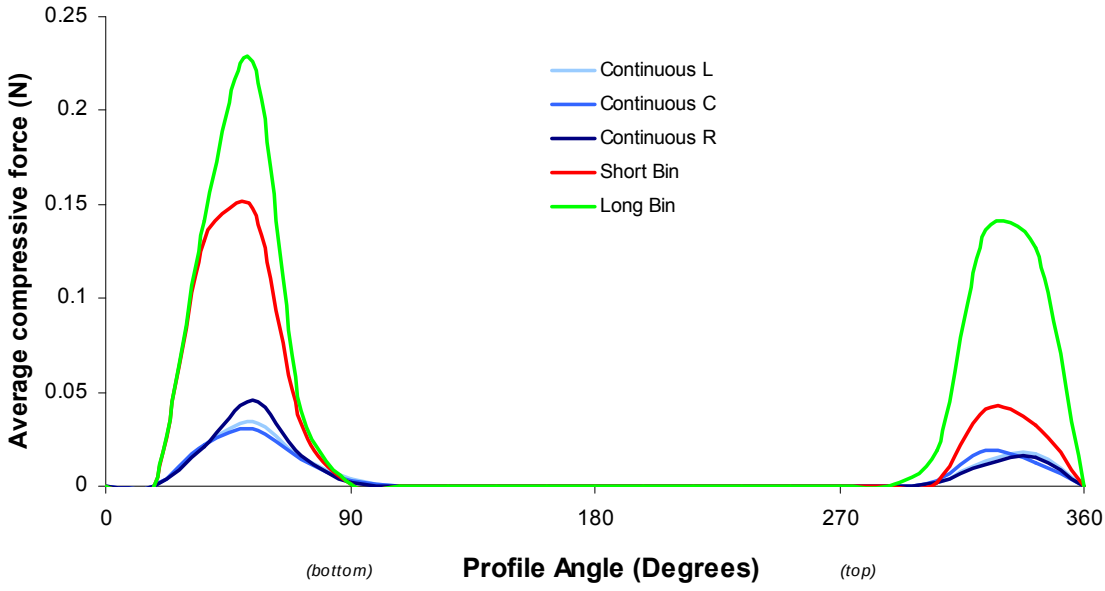

Figure 5.23. Distribution of compressive force for initial bar with original, longer, and continuous bins.

Results of this investigation indicated that variation in simulated data was not reduced by increasing the duration of the simulation (bin length); data resulting from the shortest simulation were generally as consistent as those obtained from longer simulations. Although larger compressive forces were recorded with the longer bin (Figure 5.23), the reason could not be directly connected to the longer bin itself because the depth of soil was not constant between the trials as the number of particles had to be adjusted for the larger bin.

For the continuous bin, it is most likely that a difference in the total thickness of the soil layer accounts for most of this difference in average compressive force, but the nature of the interactions may also have contributed. Because the soil is being pulled toward the stationary bar, it may slip as it is conveyed or have an initial motion with respect to the bar that is not perpendicular to the motion of the "bar" before contact which could reduce the force recorded on the bar.

From the shape of the compressive force curve in Figure 5.23, the peak of the force between 270 and 360 degrees occurs at the 306-degree segment for the short bin, the long bin, and the centre location in the continuous bin. However, the peak compressive force is at the 324-degree segment for the left and right locations in the continuous bin. This may indicate that an edge effect is affecting the data as it moves away from the centre of the bin as all other force predictions at the centre of the bin peaked at the same segment on the bar.

Without experimental data to assess the accuracy of these data, it can be assumed that the use of the data from the short-bin simulations was just as reasonable as those from the longer simulations. Justification for this argument can be taken from the shape of the

curves in Figure 5.23. The distributions of the mean forces were very similar with higher forces on the bottom of the bar and lower forces on the top. The relative size of the peak forces is also quite similar as the peak force at the bottom of the bar was about twice as large as the peak at the top in each of the simulations.

The purpose of running the continuous simulation was to determine if a difference in variation could be obtained. Figure 5.23 demonstrates that the predicted mean force profile magnitudes were different for the three bars in the simulation even though they were running simultaneously with identical properties. Further, Figure 5.22 shows that the variability of data for these 3 bar sections was not constant. This illustrates the randomness of the interactions occurring at the interface of the tool and soil and the difficulty in obtaining precise predictions of compressive force.

As was discovered with the longer bin and the continuous bin simulations, no beneficial gain, as indicated by data consistency, was realized by increasing the length of the simulation. Therefore, without experimental data to compare the accuracy of the results, the short bin data were found to be as consistent as those obtained from longer simulations and were thus considered sufficient for these analyses. The inherent variance in the dynamic process was not mitigated by increasing the length of the simulation.

CHAPTER 6 CONCLUSIONS

Results of the soil bin wear study showed a significant difference between the aluminum and steel materials in the amount of wear which occurred. With regard to the maximum radius change and the change in total volume, the aluminum bars' wear rates were approximately seven times greater than those of steel.

Supplementary to the objectives set for the soil bin studies, it was found that wear was confined to two locations on the bar as a result of the formation of a soil wedge which was created on the leading face of the bar. This caused an alteration in the soil flow pattern as well, but was similar for both the aluminum and the steel bars. As would also be expected, the level of wear was greatest on the lower portion of the bar as compared to the upper as higher soil pressures would be present at the lower half of the bar.

Simulation data confirmed some of the supplementary findings of the soil bin test. The range of soil forces matched the predictions such that higher forces were present at the lower portion of the bar. Through an application of both the soil forces and the relative velocities of the soil and tool, a relationship was determined which approximated wear rate based on these simulation parameters. Initial correlation to actual data was poor because of irregular wear patterns on one of the bars. Upon removing this outlying data, the model was determined to be,

$$W = 0.129F^{0.1524}v^{1.8928}, \qquad 6.1$$

where W = predicted wear rate (mm of radius reduction /50 km of travel),

F = simulated compressive force (N), and

v = simulated relative tangential velocity (m/s).

Although not a perfect correlation to actual data, the predicted equation indicates that a relationship likely does exist and there is promise in employing DEM simulations as a method to recreate results of tillage tool wear. Additional analyses completed in an attempt to verify the predictions of the simulation found that it was just as reasonable to use results from a shorter simulation as to use an extended virtual soil bin.

CHAPTER 7 RECOMMENDATIONS

Through the completion and analysis of these studies on tillage tool wear, limitations were discovered that reduced the effectiveness of the methods and the quality of the findings. Upon further study of DEM simulations, it is suggested that the following changes could be made.

1. The cylindrical geometry chosen for the tool shape was selected in anticipation that modeling its shape would be easier and effects of changing shape during wear would not drastically change the flow of soil. However, the cylindrical shape created unforeseen issues with soil attachment to the leading face. Because this attached soil prevented wear by protecting the bar, it needed to be included in the simulations and because the shape of the soil wedge was continually changing in the soil bin, it could not be accurately represented in the model.

   A less cohesive soil may have not created this soil attachment, but under the same conditions, a different tool shape (such as an actual cultivator sweep) would be recommended. The EDEM software would allow this geometry to be easily imported into the simulation.

2. Measurement methods must be taken in a similar manner. Issues arose with the difference in measuring radius with the CMM at a discrete point versus the average values for compressive force and relative tangential velocity over the entire segment in the simulation. In future simulations, the force and velocity should be predicted over a smaller area which would more closely match the conditions where the actual wear measurements were taken.

3. Because of the random nature of wear in a tillage scenario, more replications (i.e. more bars) would be beneficial for the process of model development and verification. As was discovered, one of the aluminum bars wore differently than the other two and thus created extra variance in the fitted model.

4. Preliminary analyses found no justifiable difference in the results of changing the length of a simulated soil bin. However, it would be beneficial to obtain experimental data on the compressive forces experienced by the bar for comparison to the values predicted by the simulation. A similar procedure could also be undertaken to verify the relative tangential velocity profile.

CHAPTER 8 REFERENCES

Anand, A., J.S. Curtis, C.R. Wassgren, B.C. Hancock, and W.R. Ketterhagen. 2008. Predicting discharge dynamics from a rectangular hopper using the discrete element method (DEM). *Chemical Engineering Science.* 63: 5821-5830.

ASTM. 2007. Standard Test Method for Particle-Size Analysis of Soils, D422 – 63. ASTM Annual Book of Standards.

ASTM. 2006. Standard Test Methods for Specific Gravity of Soil Solids by Water Pycnometer, D854-06. ASTM Annual Book of Standards.

ASTM. 2005. Standard Test Methods for Particle-Size Distribution (Gradation) of Soils Using Sieve Analysis, D6913 - 04e2. ASTM Annual Book of Standards.

ASTM. 2004. Standard Test Method for Direct Shear Test of Soils Under Consolidated Drained Conditions, D3080-04. ASTM Annual Book of Standards.

ASTM. 2002. Standard test method for conducting wet sand/rubber wheel abrasion tests, G 105-02. ASTM Annual Book of Standards.

ASTM. 2000. Standard test method for measuring abrasion using the dry sand/rubber wheel apparatus, G 65-00. ASTM Annual Book of Standards.

ASTM. 1998. Standard test method for wear testing with a pin-on-disk apparatus, G 99-95. ASTM Annual Book of Standards.

Archard, J.F. and W. Hirst. 1956. The wear of metals under unlubricated conditions. *Proceedings of the Royal Society of London. Series A, Mathematical and Physical Sciences.* 236(1206): 397-410.

Bevill, S.L., G.R. Bevill, J.R. Penmetsa, A.J. Petrella, and P.J. Rullkoetter. 2004. Finite element simulation of early creep and wear in total hip arthroplasty. *Journal of Biomechanics.* 38(12): 2365-2374.

Baxter, J., H. Abou-Chakra, U. Tuzun, and B. Mills Lamptey. 2000. A DEM simulation and experimental strategy for solving fine powder flow problems. *Transactions of the Institution of Chemical Engineers.* 78:1019-1025.

Bayhan, Y. 2005. Reduction of wear via hardfacing of chisel ploughshare. *Tribology International.* 39(6):570-574.

Breaux N.J. and J.K Keska. 2002. Application of a pin-on-disk test to determine abrasive wear. In *Proceedings of the 2002 ASEE Gulf Southwest Annual Conference.* Lafayette, LO: American Society for Engineering Education.

Cleary, P.W. 1998. Predicting charge motion, using power draw, segregation and wear in ball mills using discrete element methods. *Materials Engineering.* 11(11): 1061-1080.

Cundall, P. A., and O. D. L. Strack. 1979. A discrete numerical model for granular assemblies. *Geotechnique*. *29*(1): 47-65.

Djordjevic, N. 2003. Discrete element modelling of power draw of tumbling mills. *Mineral Processing and Extractive Metallurgy.* 112: 109-114.

Dwivedi, D.K. 2004. Microstructure and abrasive wear behaviour of iron base hardfacing. *Materials Science and Technology.* 20:1326-1330.

Er, U. and B. Par. 2006. Wear of plowshare components in SAE 950C steel surface hardened by powder boriding. *Wear.* 261:251-255.

Fan, S.C., Y.Y. Jiao, and J. Zhao. 2004. On modelling of incident boundary for wave propagation in jointed rock masses using discrete element method. *Computers and Geotechnics.* 31: 57-66.

Feilke, J.M., T.W. Riley, M.G. Slattery, R.W. Fitzpatrick. 1993. Comparison of tillage forces and wear rates of pressed and cast cultivator shares. *Soil & Tillage Research.* 25:317-328.

Fialho, J.C., P.R. Fernandes, L. Eca, and J. Folgado. 2007. Computational hip joint simulator for wear and heat generation. *Journal of Biomechanics.* 40(11): 2358-2366.

Fillot, N., I. Iordanoff, and Y. Berthier. 2006. Modelling third body flows with a discrete element method – a tool for understanding wear with adhesive particles. *Tribology International.* 40: 973-981.

Fillot, N., I. Iordanoff, and Y. Berthier. 2005. Simulation of wear through mass balance in a dry contact. *Journal of Tribology.* 127: 230-237.

Ford, C., M.B. Bush, and B. Lawn. 2009. Effect of wear on stress distributions and potential fracture in teeth. *Journal of Materials Science: Materials in Medicine.* 20:2243-2247.

Gill, W.R., R.L. Schafer, and R.D. Wismer. 1994. Soil dymanics and soil bins. In *Advances in Soil Dynamics Vol. 1*, eds. S.K. Upadhyaya, W.J. Chancellor, J.V. Perumpral, R.L. Schafer, W.R. Gill, and G.E. VandenBerg, 1-19. St. Joseph, MI: American Society of Agricultural Engineers.

Graff, L.G., R.C. Roberge, M.A. Roberge, T.G. Crowe. 2007. Wear of ripper point hardsurfacings. In Proceedings of the 2007 North Central Intersectional Conference of the ASABE, RRV-07120. Fargo, ND: American Society of Agricultural and Biological Engineers.

Hunt, D. 1983. Farm Power and Machinery Management, 8th edition, Ames, Iowa: The Iowa State University Press.

Iordanoff, I., J.L. Charles, and Y. Berthier. 2007. Discrete element model: a helpful tool for abrasion process study. *Proceedings of the Institution of Mechanical Engineers – Part B – Engineering Manufacture.* 221: 1031-1039.

Itasca. 2003. PFC3D User's Manual, Version 3.0. Itasca Consulting Group Inc, Minneapolis, MN, USA.

Kalala, J.T., M.T. Bwalya, and M.H. Moys. 2005. Discrete element method (DEM) modelling of evolving liner profiles due to wear. Part I: DEM validation. *Minerals Engineering.* 18: 1386-1391.

Kragelskii, I.V. 1965. Friction and Wear. London, UK: Butterworth and Co.

Krause, F. 2007. A research area with great prospects. *Bulk Solids Handling*. 27(1):14-16.

Kruggel-Emden, H., S. Wirtz, E. Simsek, and V. Scherer. 2006. Modeling of granular flow and combined heat transfer in hoppers by the discrete element method (DEM). *Journal of Pressure Vessel Technology.* 128: 439-444.

Kushwaha, R.L. and J. Shi. 1991. Investigation of wear of agricultural tillage tools. *Lubrication Engineering*. 47(3): 219-222.

Landry, H., C. Lague, and M. Roberge. 2006. Discrete element modelling of machine-manure interactions. *Computers and Electronics in Agriculture.* 52: 90-106.

Lewis, R.W., D.T. Gethin, X.S. Yang, and R.C. Rowe. 2005. A combined finite-discrete element method for simulating pharmaceutical powder tableting. *International Journal for Numerical Methods in Engineering.* 62: 853-869.

Li. J., C. Webb, S.S. Pandiella, and G.M. Campbell. 2003. Discrete particle motion on sieves – a numerical study using the DEM simulation. *Powder Technology.* 133: 190-202.

Liu, C., Q. Zhang, and Y. Chen. 2008. PFC3D simulations of lateral pressures in model bins. In Proceedings of the 2008 Annual Conference of the ASABE, 083340. Providence, RI: American Society of Agricultural and Biological Engineers.

Matweb. 2009. Aluminum 6061-T4; 6061-T451. Available: <http://www.matweb.com/search/DataSheet.aspx?MatGUID=d5ea75577b1b49e8ad03caf007db5ba8> (Accessed: March 24, 2009)

Minkin, A., A. Katterfeld, and T. Groger. 2007. Application of the discrete element method in materials handling – Part 2: Screw and shaftless screw conveyors. *Bulk Solids Handling.* 27(2): 92-93.

Moore, D.F. 1975. Wear and abrasion. In *Principles and Applications of Tribology*, ed. D.W. Hopkins, 177-202. Oxford, UK: Pergamon Press.

Natsis, A., G. Petropolous, and C. Pandazaras. 2007. Influence of local soil conditions on mouldboard ploughshare abrasive wear. *Tribology International.* 41(3):151-157

Nezami, E.G., Y.M.A. Hashash, D. Zhao, and J. Ghaboussi. 2007. Simulation of front end loader bucket – soil interaction using discrete element method. *International Journal for Numerical and Analytical Methods in Geomechanics.* 31: 1147-1162.

Owsiak, W. 1999. Wear of spring tine cultivator points in sandy loam and light clay soils in southern Poland. *Soil & Tillage Research* 50:333-340.

Owsiak, Z. 1997. Wear of symmetrical wedge-shaped tillage tools. *Soil & Tillage Research.* 43:295-308.

Saskatchewan Ministry of Agriculture. 2008. Who knew – agriculture in Saskatchewan. Government of Saskatchewan, Regina, SK.

Srivastava, A.K, C.E. Goering, R.P. Rohrbach, and D.R. Buckmaster. 2006. Soil tillage. In *Engineering Principles of Agricultural Machines*, 2nd Ed. ed. P. McCann, 169-229. St. Joseph, MI: American Society of Agricultural and Biological Engineers.

Swanson, P.A. 1993. Comparison of laboratory abrasion tests and field tests of materials used in tillage equipment. *In Tribology: Wear Test Selection for Design and Application, ASTM STP 1199. ed.* A. W. Ruff and R. Bayer, 80-99. Philadelphia, PA: American Society for Testing and Materials.

Van Zeebroeck, M. G. Lombaert, E. Dintwa, H. Ramon, G. Degrande, and E. Tijskens. 2008. The simulation of the impact damage to fruit during the passage of a truck over a speed bump by means of the discrete element method. *Biosystems Engineering.* 101: 58-68.

Wingate-Hill, R., M.I.E. Aust, G.R. Davis, and H.G. Bowditch. 1979. Wear of hardfacing treatments applied to shares of tined tillage implements. *Transactions of the Institution of Engineers, Australia*. ME4:11-16.

Yu, H.J. 1991. Abrasive wear evaluation of tillage tool materials. Unpublished M.Sc Thesis. University of Regina, Regina, SK.

Zhang, J. 1992. Measurement of wear and draft of cultivator sweeps with hardened edges. Unpublished M.Sc. thesis. Department of Agricultural and Bioresource Engineering, University of Saskatchewan, Saskatoon, SK.

Zhang, X. and L. Vu-Quoc. 2000. Simulation of chute flow of soybeans using an improved tangential force-displacement model. *Mechanics of Materials.* 32: 115-129.

Zhu, H.P., Z.Y. Zhou, R.Y. Yang, and A.B. Yu. 2007. Discrete particle simulation of particulate systems: Theoretical developments. *Chemical Engineering Science.* 62: 3378-3396.

Appendix A
Soil Property Data

Table A.1. Particle size distribution data for dry sieve analysis.

Seive No.	Opening Size	$Mass_{empty}$	$Mass_{Total}$	$Mass_{Soil}$	Percent of Total	Percent Passing
	μm	g	g	g	%	%
4	4750	0.00	0.00	0.00	0.00	100.00
10	2000	463.78	540.48	76.70	7.71	92.29
20	850	428.23	661.96	233.73	23.51	68.78
30	595	425.90	563.05	137.15	13.79	54.98
40	425	351.10	688.27	337.17	33.91	21.07
60	250	343.36	462.55	119.19	11.99	9.08
100	150	333.72	391.56	57.84	5.82	3.26
200	75	319.45	346.47	27.02	2.72	0.54
Pan	0	378.80	384.21	5.41	0.54	0.00
Total				**994.21**	**100**	

Table A.2. Particle size distribution data for washed sieve analysis.

Seive No.	Opening Size	$Mass_{empty}$	$Mass_{Total}$	$Mass_{Soil}$	Percent of Total	Percent Passing
	μm	g	g	g	%	%
4	4750	0.00	0.00	0.00	0.00	100.00
10	2000	463.46	535.25	71.79	7.23	92.77
20	850	428.05	635.12	207.07	20.87	71.90
30	595	425.81	520.60	94.79	9.55	62.35
40	425	350.93	491.03	140.10	14.12	48.23
60	250	343.16	481.51	138.35	13.94	34.29
100	150	333.64	410.40	76.76	7.74	26.55
200	75	319.41	387.20	67.79	6.83	19.72
Silt	5	(determined from hydrometer analysis)				15.90
Pan	0	378.77	389.49	195.70	19.72	0.00
Total				**992.35**	**100**	

Table A.3. Data and calculated values for specific gravity (particle density).

	Overall	Dry Sand	Washed Sand	Balls	Fines
Mass of flask and water, M1 (g)	678.37	681.35	678.26	678.00	671.86
Temperature of water, T1 (deg C)	22	23	22	22	22
Mass of flask, water and soil, M2 (g)	739.71	754.77	744.82	751.12	692.40
Temperature of water and soil (deg C)	22	22	22	22	22
Mass of dish (g)	16.69	18.84	16.21	17.58	480.96
Mass of dried dish (g)	115.25	136.52	122.15	135.01	512.99
Mass of dry soil Ms (g)	98.56	117.68	105.94	117.43	32.03
Equivalent mass of water, Mw (g)	37.22	44.26	39.38	44.31	11.49
Specific Gravity at T1	2.648	2.659	2.690	2.650	2.788
Density of distilled water at T1	0.9996	0.9996	0.9996	0.9996	0.9996
Specific Gravity at 20 degrees C	2.647	2.658	2.689	2.649	2.787

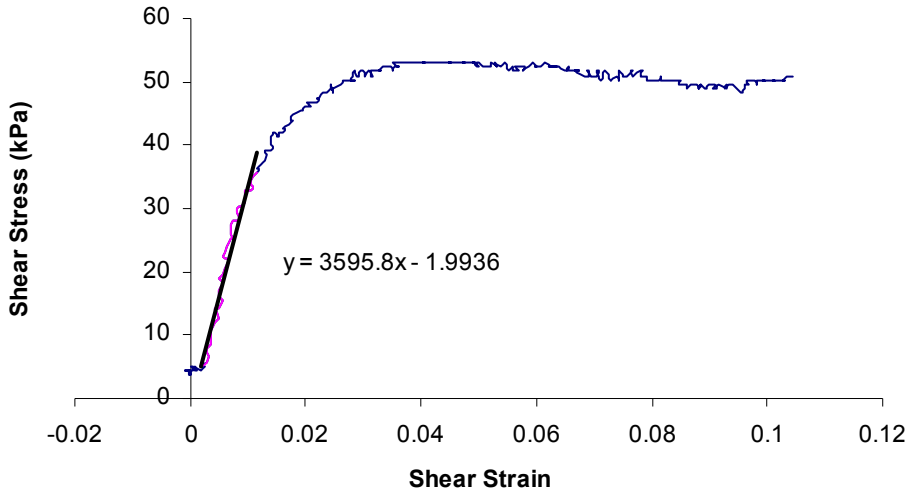

Figure A.1. Shear stress - strain plot at low normal force (52.6 kPa) to estimate shear modulus.

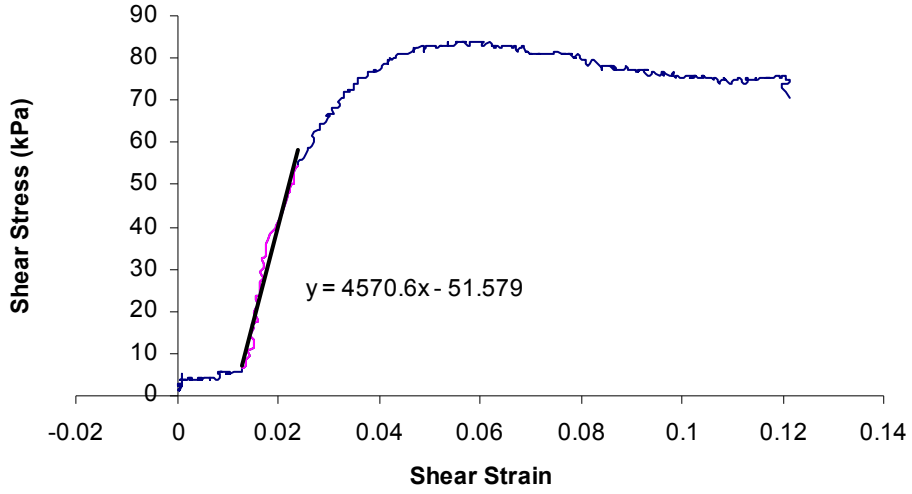

Figure A.2. Shear stress - strain plot at medium normal force (91.8 kPa) to estimate shear modulus.

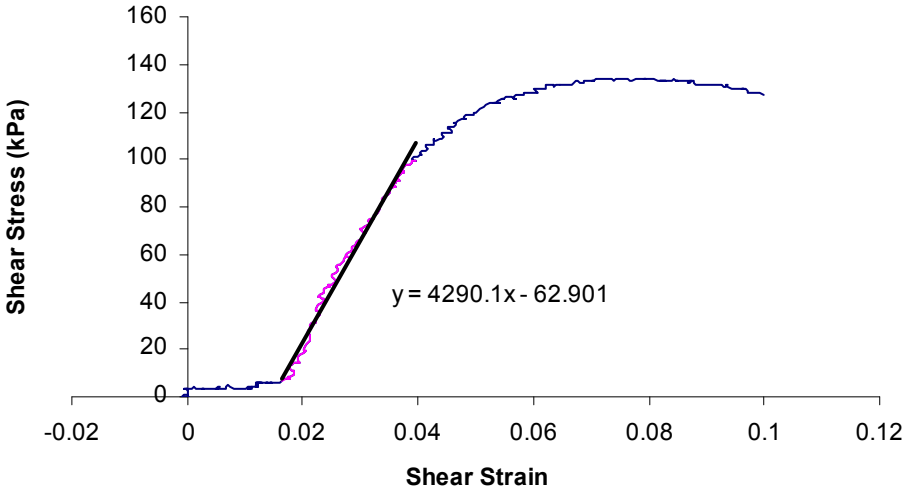

Figure A.3. Shear stress - strain plot at high normal force (170.3 kPa) to estimate shear modulus.

Appendix B
CMM Measurement Data

Table B.1 CMM radius measurements for bar AS1 for given intervals of wear.

			Radius Measurement (mm)								
Location	**Angle**	**CMM Code**	**Initial**	**50 km**	**100 km**	**150 km**	**200 km**	**250 km**	**300 km**	**350 km**	**400 km**
C	0	WP 17	12.686	12.678	12.689	12.682	12.672	12.676	12.679	12.683	12.681
C	18	WP 16	12.698	12.690	12.689	12.691	12.680	12.687	12.686	12.691	12.689
C	36	WP 15	12.709	12.703	12.697	12.698	12.691	12.693	12.731	12.714	12.700
C	54	WP 14	12.716	12.661	12.656	12.625	12.588	12.560	12.568	12.520	12.466
C	72	WP 13	12.721	12.676	12.629	12.580	12.632	12.555	12.508	12.481	12.416
C	90	WP 12	12.729	12.718	12.710	12.703	12.712	12.725	12.691	12.686	12.669
C	108	WP 51	12.711	12.715	12.720	12.724	12.818	12.772	12.738	12.734	12.736
C	126	WP 50	12.713	12.705	12.706	12.706	12.709	12.712	12.708	12.715	12.712
C	144	WP 49	12.712	12.708	12.709	12.711	12.714	12.716	12.710	12.715	12.713
C	162	WP 48	12.706	12.706	12.707	12.708	12.713	12.712	12.703	12.720	12.706
C	180	WP 47	12.694	12.704	12.702	12.706	12.712	12.710	12.704	12.700	12.698
C	198	WP 46	12.688	12.700	12.699	12.700	12.703	12.700	12.695	12.691	12.688
C	216	WP 45	12.686	12.697	12.694	12.695	12.699	12.697	12.690	12.681	12.680
C	234	WP 44	12.678	12.694	12.691	12.692	12.693	12.690	12.684	12.677	12.676
C	252	WP 43	12.671	12.686	12.684	12.683	12.767	12.715	12.712	12.680	12.668
C	270	WP 22	12.648	12.649	12.653	12.651	12.657	12.673	12.672	12.656	12.653
C	288	WP 21	12.650	12.649	12.649	12.646	12.746	12.693	12.678	12.626	12.639
C	306	WP 20	12.656	12.631	12.613	12.591	12.611	12.546	12.586	12.481	12.453
C	324	WP 19	12.662	12.601	12.554	12.510	12.457	12.421	12.375	12.325	12.282
C	342	WP 18	12.673	12.664	12.663	12.665	12.655	12.658	12.655	12.669	12.650
L	0	WP 28	12.688	12.678	12.692	12.684	12.683	12.680	12.685	12.687	12.687
L	18	WP 29	12.698	12.689	12.695	12.688	12.680	12.688	12.693	12.693	12.692
L	36	WP 30	12.708	12.701	12.697	12.698	12.692	12.704	12.705	12.717	12.707
L	54	WP 31	12.718	12.666	12.664	12.624	12.598	12.569	12.563	12.527	12.485
L	72	WP 32	12.723	12.686	12.642	12.587	12.622	12.541	12.493	12.453	12.392
L	90	WP 33	12.730	12.723	12.713	12.704	12.718	12.724	12.691	12.681	12.663
L	108	WP 34	12.714	12.719	12.720	12.718	12.831	12.770	12.736	12.735	12.744
L	126	WP 35	12.720	12.712	12.710	12.713	12.716	12.717	12.715	12.722	12.720
L	144	WP 36	12.712	12.710	12.710	12.714	12.716	12.716	12.711	12.717	12.714
L	162	WP 37	12.702	12.707	12.707	12.709	12.713	12.713	12.706	12.725	12.697
L	180	WP 38	12.698	12.704	12.703	12.705	12.712	12.706	12.699	12.700	12.698
L	198	WP 39	12.685	12.698	12.699	12.698	12.705	12.700	12.695	12.662	12.686
L	216	WP 40	12.680	12.696	12.691	12.693	12.700	12.691	12.686	12.684	12.678
L	234	WP 41	12.673	12.689	12.687	12.688	12.690	12.690	12.683	12.676	12.672
L	252	WP 42	12.666	12.683	12.681	12.680	12.767	12.722	12.713	12.674	12.667
L	270	WP 23	12.646	12.644	12.646	12.646	12.652	12.661	12.660	12.658	12.651
L	288	WP 24	12.650	12.645	12.646	12.644	12.744	12.686	12.675	12.625	12.634
L	306	WP 25	12.657	12.632	12.604	12.593	12.604	12.533	12.548	12.473	12.446
L	324	WP 26	12.663	12.612	12.604	12.553	12.520	12.482	12.431	12.380	12.340
L	342	WP 27	12.676	12.669	12.669	12.658	12.659	12.660	12.644	12.662	12.638
R	0	WP 6	12.683	12.670	12.677	12.675	12.670	12.673	12.679	12.681	12.678
R	18	WP 7	12.690	12.681	12.683	12.680	12.682	12.680	12.689	12.689	12.687
R	36	WP 8	12.719	12.694	12.694	12.690	12.683	12.690	12.700	12.698	12.701
R	54	WP 9	12.713	12.664	12.615	12.602	12.589	12.530	12.547	12.502	12.440
R	72	WP 10	12.721	12.671	12.638	12.593	12.642	12.579	12.518	12.489	12.423
R	90	WP 11	12.725	12.715	12.710	12.699	12.713	12.725	12.689	12.683	12.668
R	108	WP 52	12.710	12.716	12.720	12.720	12.834	12.767	12.743	12.725	12.735
R	126	WP 53	12.710	12.708	12.708	12.709	12.713	12.713	12.710	12.718	12.716
R	144	WP 54	12.714	12.713	12.714	12.713	12.717	12.720	12.714	12.716	12.716
R	162	WP 55	12.705	12.712	12.709	12.711	12.714	12.715	12.709	12.726	12.707
R	180	WP 56	12.701	12.710	12.710	12.710	12.715	12.711	12.708	12.704	12.702
R	198	WP 57	12.686	12.705	12.703	12.704	12.710	12.706	12.702	12.696	12.691
R	216	WP 58	12.687	12.698	12.699	12.696	12.701	12.701	12.694	12.686	12.684
R	234	WP 59	12.678	12.696	12.691	12.693	12.693	12.695	12.686	12.678	12.678
R	252	WP 60	12.681	12.688	12.684	12.682	12.772	12.718	12.716	12.680	12.669
R	270	WP 1	12.655	12.655	12.658	12.654	12.661	12.671	12.687	12.662	12.659
R	288	WP 2	12.650	12.649	12.649	12.647	12.727	12.709	12.655	12.635	12.645
R	306	WP 3	12.656	12.629	12.608	12.595	12.641	12.598	12.620	12.508	12.484
R	324	WP 4	12.660	12.594	12.549	12.515	12.560	12.437	12.398	12.355	12.305
R	342	WP 5	12.671	12.655	12.660	12.649	12.646	12.642	12.618	12.650	12.613

Table B.2. CMM radius measurements for bar AS2 for given intervals of wear.

			Radius Measurement (mm)								
Location	**Angle**	**CMM Code**	**Initial**	**50 km**	**100 km**	**150 km**	**200 km**	**250 km**	**300 km**	**350 km**	**400 km**
C	0	WP 17	12.737	12.730	12.730	12.727	12.734	12.724	12.731	12.733	12.729
C	18	WP 16	12.737	12.727	12.723	12.725	12.727	12.717	12.727	12.733	12.729
C	36	WP 15	12.731	12.719	12.717	12.716	12.720	12.722	12.718	12.723	12.720
C	54	WP 14	12.719	12.644	12.608	12.580	12.548	12.530	12.495	12.431	12.507
C	72	WP 13	12.703	12.617	12.596	12.539	12.576	12.509	12.445	12.416	12.405
C	90	WP 12	12.688	12.665	12.657	12.652	12.659	12.663	12.640	12.620	12.616
C	108	WP 51	12.655	12.652	12.669	12.661	12.752	12.702	12.659	12.662	12.662
C	126	WP 50	12.646	12.635	12.636	12.637	12.616	12.619	12.618	12.625	12.624
C	144	WP 49	12.641	12.637	12.637	12.635	12.586	12.595	12.591	12.593	12.594
C	162	WP 48	12.638	12.642	12.641	12.643	12.634	12.648	12.640	12.640	12.642
C	180	WP 47	12.639	12.648	12.648	12.646	12.643	12.653	12.646	12.644	12.642
C	198	WP 46	12.651	12.666	12.667	12.664	12.659	12.670	12.663	12.656	12.656
C	216	WP 45	12.664	12.679	12.681	12.680	12.675	12.684	12.677	12.670	12.670
C	234	WP 44	12.677	12.697	12.697	12.699	12.656	12.668	12.655	12.642	12.645
C	252	WP 43	12.686	12.709	12.710	12.710	12.727	12.698	12.676	12.653	12.649
C	270	WP 22	12.686	12.698	12.698	12.699	12.696	12.695	12.694	12.686	12.685
C	288	WP 21	12.707	12.709	12.710	12.707	12.819	12.747	12.713	12.688	12.686
C	306	WP 20	12.713	12.697	12.676	12.661	12.634	12.616	12.603	12.567	12.536
C	324	WP 19	12.723	12.680	12.645	12.602	12.566	12.536	12.516	12.486	12.432
C	342	WP 18	12.732	12.727	12.727	12.717	12.721	12.714	12.721	12.739	12.714
L	0	WP 28	12.732	12.726	12.717	12.724	12.729	12.722	12.728	12.731	12.727
L	18	WP 29	12.735	12.724	12.723	12.722	12.728	12.714	12.724	12.729	12.727
L	36	WP 30	12.728	12.717	12.714	12.716	12.715	12.708	12.712	12.733	12.725
L	54	WP 31	12.722	12.657	12.656	12.605	12.610	12.587	12.567	12.573	12.573
L	72	WP 32	12.704	12.648	12.587	12.543	12.576	12.527	12.456	12.436	12.396
L	90	WP 33	12.690	12.669	12.656	12.652	12.659	12.668	12.638	12.626	12.606
L	108	WP 34	12.660	12.661	12.663	12.665	12.754	12.693	12.656	12.667	12.667
L	126	WP 35	12.653	12.640	12.639	12.638	12.617	12.626	12.621	12.629	12.630
L	144	WP 36	12.647	12.637	12.637	12.638	12.589	12.600	12.597	12.599	12.599
L	162	WP 37	12.645	12.645	12.644	12.643	12.641	12.655	12.644	12.649	12.644
L	180	WP 38	12.642	12.647	12.648	12.650	12.644	12.655	12.647	12.643	12.646
L	198	WP 39	12.653	12.669	12.668	12.666	12.662	12.674	12.665	12.660	12.657
L	216	WP 40	12.666	12.686	12.684	12.683	12.681	12.688	12.681	12.670	12.672
L	234	WP 41	12.682	12.702	12.701	12.700	12.675	12.679	12.672	12.662	12.663
L	252	WP 42	12.688	12.713	12.715	12.710	12.738	12.707	12.642	12.661	12.652
L	270	WP 23	12.686	12.699	12.701	12.700	12.690	12.698	12.695	12.693	12.683
L	288	WP 24	12.709	12.707	12.707	12.702	12.817	12.746	12.702	12.687	12.681
L	306	WP 25	12.713	12.695	12.682	12.660	12.643	12.615	12.596	12.556	12.529
L	324	WP 26	12.724	12.681	12.654	12.601	12.564	12.518	12.469	12.435	12.377
L	342	WP 27	12.727	12.711	12.711	12.704	12.709	12.695	12.702	12.700	12.681
R	0	WP 6	12.735	12.724	12.726	12.723	12.731	12.718	12.724	12.728	12.729
R	18	WP 7	12.738	12.720	12.721	12.719	12.725	12.719	12.720	12.729	12.726
R	36	WP 8	12.730	12.713	12.712	12.714	12.717	12.711	12.718	12.724	12.726
R	54	WP 9	12.718	12.653	12.650	12.605	12.607	12.583	12.580	12.587	12.587
R	72	WP 10	12.699	12.650	12.594	12.545	12.591	12.502	12.453	12.436	12.411
R	90	WP 11	12.688	12.670	12.658	12.655	12.663	12.660	12.637	12.621	12.605
R	108	WP 52	12.664	12.655	12.652	12.656	12.766	12.706	12.663	12.672	12.668
R	126	WP 53	12.651	12.636	12.635	12.641	12.619	12.624	12.620	12.625	12.627
R	144	WP 54	12.647	12.640	12.640	12.641	12.598	12.609	12.603	12.607	12.607
R	162	WP 55	12.644	12.643	12.644	12.646	12.640	12.652	12.644	12.642	12.645
R	180	WP 56	12.640	12.650	12.650	12.650	12.646	12.654	12.648	12.645	12.645
R	198	WP 57	12.653	12.667	12.668	12.667	12.664	12.673	12.665	12.658	12.659
R	216	WP 58	12.663	12.684	12.682	12.680	12.678	12.686	12.677	12.670	12.669
R	234	WP 59	12.676	12.699	12.699	12.698	12.660	12.668	12.660	12.651	12.650
R	252	WP 60	12.684	12.710	12.710	12.709	12.730	12.710	12.680	12.661	12.654
R	270	WP 1	12.685	12.699	12.701	12.698	12.691	12.702	12.698	12.687	12.682
R	288	WP 2	12.704	12.706	12.708	12.700	12.811	12.746	12.702	12.684	12.684
R	306	WP 3	12.711	12.693	12.678	12.658	12.631	12.610	12.596	12.562	12.524
R	324	WP 4	12.719	12.671	12.641	12.598	12.583	12.550	12.513	12.469	12.419
R	342	WP 5	12.730	12.722	12.726	12.716	12.719	12.697	12.702	12.716	12.706

Table B.3. CMM radius measurements for bar AS3 for given intervals of wear.

			Radius Measurement (mm)								
Location	**Angle**	**CMM Code**	**Initial**	**50 km**	**100 km**	**150 km**	**200 km**	**250 km**	**300 km**	**350 km**	**400 km**
C	0	WP 17	12.744	12.737	12.742	12.739	12.749	12.731	12.740	12.741	12.741
C	18	WP 16	12.771	12.767	12.769	12.765	12.776	12.760	12.768	12.770	12.771
C	36	WP 15	12.790	12.787	12.784	12.796	12.793	12.785	12.786	12.790	12.793
C	54	WP 14	12.797	12.750	12.739	12.728	12.730	12.723	12.701	12.668	12.666
C	72	WP 13	12.801	12.766	12.718	12.680	12.723	12.711	12.646	12.609	12.592
C	90	WP 12	12.782	12.784	12.770	12.759	12.786	12.788	12.754	12.744	12.736
C	108	WP 51	12.759	12.759	12.761	12.758	12.866	12.788	12.760	12.770	12.768
C	126	WP 50	12.730	12.727	12.725	12.724	12.719	12.731	12.725	12.735	12.734
C	144	WP 49	12.701	12.704	12.703	12.700	12.689	12.706	12.697	12.705	12.706
C	162	WP 48	12.668	12.673	12.672	12.669	12.660	12.674	12.669	12.670	12.672
C	180	WP 47	12.637	12.644	12.644	12.646	12.632	12.651	12.641	12.642	12.639
C	198	WP 46	12.613	12.626	12.621	12.623	12.611	12.624	12.621	12.616	12.613
C	216	WP 45	12.595	12.609	12.606	12.609	12.599	12.616	12.607	12.597	12.599
C	234	WP 44	12.589	12.600	12.603	12.604	12.595	12.604	12.598	12.590	12.590
C	252	WP 43	12.593	12.603	12.606	12.607	12.626	12.634	12.609	12.591	12.590
C	270	WP 22	12.581	12.584	12.586	12.586	12.626	12.591	12.594	12.590	12.596
C	288	WP 21	12.606	12.605	12.603	12.606	12.718	12.638	12.601	12.591	12.584
C	306	WP 20	12.638	12.612	12.592	12.582	12.564	12.534	12.514	12.485	12.448
C	324	WP 19	12.674	12.626	12.596	12.596	12.545	12.487	12.462	12.408	12.361
C	342	WP 18	12.710	12.704	12.705	12.749	12.715	12.701	12.711	12.691	12.685
L	0	WP 28	12.748	12.744	12.741	12.742	12.755	12.739	12.745	12.746	12.745
L	18	WP 29	12.781	12.774	12.777	12.774	12.784	12.769	12.774	12.781	12.779
L	36	WP 30	12.802	12.795	12.795	12.794	12.803	12.788	12.797	12.802	12.804
L	54	WP 31	12.812	12.759	12.752	12.705	12.661	12.654	12.655	12.600	12.595
L	72	WP 32	12.811	12.763	12.717	12.672	12.667	12.638	12.606	12.557	12.538
L	90	WP 33	12.794	12.790	12.779	12.769	12.802	12.787	12.764	12.749	12.741
L	108	WP 34	12.765	12.769	12.770	12.765	12.874	12.800	12.773	12.781	12.781
L	126	WP 35	12.734	12.732	12.725	12.726	12.721	12.733	12.726	12.736	12.736
L	144	WP 36	12.702	12.706	12.704	12.702	12.692	12.708	12.700	12.704	12.704
L	162	WP 37	12.677	12.670	12.670	12.667	12.658	12.674	12.665	12.671	12.670
L	180	WP 38	12.630	12.637	12.637	12.636	12.623	12.640	12.633	12.631	12.634
L	198	WP 39	12.604	12.612	12.615	12.614	12.602	12.617	12.608	12.605	12.605
L	216	WP 40	12.584	12.596	12.599	12.599	12.587	12.601	12.594	12.587	12.584
L	234	WP 41	12.577	12.590	12.590	12.592	12.585	12.591	12.587	12.576	12.580
L	252	WP 42	12.578	12.590	12.596	12.591	12.627	12.625	12.599	12.583	12.578
L	270	WP 23	12.569	12.570	12.574	12.577	12.592	12.568	12.584	12.578	12.577
L	288	WP 24	12.596	12.593	12.597	12.595	12.710	12.622	12.587	12.577	12.572
L	306	WP 25	12.634	12.596	12.571	12.618	12.541	12.508	12.484	12.448	12.401
L	324	WP 26	12.672	12.613	12.584	12.550	12.514	12.456	12.442	12.376	12.310
L	342	WP 27	12.710	12.705	12.704	12.703	12.716	12.700	12.709	12.702	12.695
R	0	WP 6	12.732	12.727	12.728	12.726	12.739	12.722	12.731	12.734	12.730
R	18	WP 7	12.758	12.751	12.753	12.754	12.763	12.749	12.752	12.756	12.753
R	36	WP 8	12.775	12.767	12.767	12.767	12.774	12.763	12.766	12.775	12.777
R	54	WP 9	12.782	12.740	12.724	12.687	12.687	12.679	12.649	12.615	12.616
R	72	WP 10	12.782	12.755	12.713	12.662	12.673	12.653	12.589	12.551	12.530
R	90	WP 11	12.768	12.764	12.753	12.741	12.767	12.765	12.735	12.723	12.718
R	108	WP 52	12.745	12.747	12.752	12.749	12.846	12.772	12.750	12.761	12.759
R	126	WP 53	12.724	12.723	12.719	12.718	12.711	12.724	12.718	12.726	12.727
R	144	WP 54	12.700	12.704	12.700	12.698	12.690	12.704	12.699	12.704	12.704
R	162	WP 55	12.671	12.678	12.674	12.674	12.664	12.679	12.674	12.674	12.674
R	180	WP 56	12.648	12.654	12.651	12.653	12.642	12.657	12.649	12.646	12.649
R	198	WP 57	12.626	12.636	12.637	12.636	12.624	12.640	12.632	12.625	12.625
R	216	WP 58	12.610	12.625	12.622	12.624	12.615	12.629	12.618	12.611	12.612
R	234	WP 59	12.608	12.620	12.618	12.621	12.615	12.621	12.623	12.606	12.608
R	252	WP 60	12.607	12.618	12.628	12.625	12.638	12.651	12.625	12.610	12.608
R	270	WP 1	12.600	12.601	12.606	12.607	12.652	12.614	12.616	12.604	12.613
R	288	WP 2	12.622	12.620	12.617	12.617	12.733	12.651	12.617	12.606	12.600
R	306	WP 3	12.647	12.624	12.599	12.590	12.581	12.553	12.543	12.513	12.493
R	324	WP 4	12.676	12.640	12.617	12.584	12.562	12.519	12.494	12.444	12.414
R	342	WP 5	12.703	12.692	12.688	12.681	12.693	12.673	12.672	12.669	12.649

Table B.4. CMM radius measurements for bar AA1 for given intervals of wear.

			Radius Measurement (mm)								
Location	**Angle**	**CMM Code**	**Initial**	**50 km**	**100 km**	**150 km**	**200 km**	**250 km**	**300 km**	**350 km**	**400 km**
C	0	WP 17	12.693	12.696	12.693	12.686	12.712	12.696	12.695	12.708	12.702
C	18	WP 16	12.715	12.714	12.710	12.711	12.729	12.716	12.717	12.728	12.735
C	36	WP 15	12.757	12.758	12.754	12.723	12.767	12.755	12.755	12.773	12.764
C	54	WP 14	12.797	12.727	12.712	12.795	12.696	12.681	12.321	12.001	11.977
C	72	WP 13	12.823	12.702	12.458	12.120	12.004	11.666	11.194	10.792	10.678
C	90	WP 12	12.843	12.824	12.784	12.583	12.635	12.384	11.828	11.326	11.064
C	108	WP 51	12.824	12.826	12.825	12.824	12.905	12.846	12.820	12.669	12.440
C	126	WP 50	12.835	12.831	12.835	12.838	12.827	12.832	12.837	12.844	12.844
C	144	WP 49	12.844	12.841	12.843	12.840	12.831	12.838	12.919	12.840	12.839
C	162	WP 48	12.839	12.806	12.838	12.841	12.826	12.834	12.840	12.833	12.830
C	180	WP 47	12.833	12.831	12.832	12.836	12.815	12.829	12.830	12.819	12.821
C	198	WP 46	12.833	12.827	12.829	12.825	12.807	12.822	12.820	12.808	12.809
C	216	WP 45	12.809	12.806	12.809	12.807	12.790	12.801	12.802	12.785	12.788
C	234	WP 44	12.791	12.786	12.789	12.796	12.778	12.786	12.787	12.767	12.773
C	252	WP 43	12.746	12.745	12.745	12.756	12.741	12.759	12.745	12.726	12.730
C	270	WP 22	12.693	12.696	12.694	12.700	12.752	12.722	12.702	12.689	12.708
C	288	WP 21	12.673	12.668	12.664	12.672	12.756	12.678	12.655	12.622	12.613
C	306	WP 20	12.662	12.570	12.486	12.440	12.318	12.230	12.049	11.871	11.687
C	324	WP 19	12.663	12.521	12.408	12.276	12.210	12.113	11.892	11.756	11.551
C	342	WP 18	12.671	12.675	12.671	12.657	12.686	12.676	12.669	12.641	12.610
L	0	WP 28	12.684	12.696	12.685	12.675	12.704	12.691	12.684	12.700	12.695
L	18	WP 29	12.705	12.708	12.704	12.704	12.723	12.706	12.709	12.719	12.716
L	36	WP 30	12.752	12.748	12.749	12.737	12.760	12.746	12.744	12.759	12.759
L	54	WP 31	12.792	12.788	12.721	12.680	12.511	12.453	12.310	11.785	11.814
L	72	WP 32	12.821	12.660	12.441	12.002	11.896	11.531	11.269	10.550	10.530
L	90	WP 33	12.843	12.821	12.783	12.515	12.580	12.258	11.939	11.038	10.962
L	108	WP 34	12.829	12.827	12.825	12.829	12.909	12.849	12.829	12.514	12.438
L	126	WP 35	12.840	12.836	12.845	12.840	12.835	12.835	12.817	12.852	12.850
L	144	WP 36	12.851	12.852	12.851	12.848	12.839	12.849	12.848	12.851	12.845
L	162	WP 37	12.849	12.839	12.846	12.849	12.830	12.843	12.847	12.839	12.839
L	180	WP 38	12.842	12.839	12.840	12.841	12.825	12.834	12.839	12.829	12.826
L	198	WP 39	12.835	12.831	12.832	12.834	12.818	12.831	12.832	12.819	12.814
L	216	WP 40	12.818	12.814	12.815	12.815	12.786	12.810	12.810	12.795	12.793
L	234	WP 41	12.797	12.794	12.796	12.803	12.781	12.792	12.794	12.775	12.774
L	252	WP 42	12.756	12.748	12.750	12.761	12.751	12.767	12.746	12.725	12.730
L	270	WP 23	12.698	12.698	12.699	12.700	12.753	12.720	12.705	12.692	12.708
L	288	WP 24	12.670	12.667	12.662	12.670	12.737	12.665	12.635	12.542	12.263
L	306	WP 25	12.660	12.583	12.486	12.393	12.077	11.961	11.750	11.483	10.940
L	324	WP 26	12.656	12.530	12.408	12.169	12.060	11.793	11.539	11.350	10.921
L	342	WP 27	12.662	12.664	12.661	12.661	12.676	12.691	12.593	12.607	12.443
R	0	WP 6	12.705	12.708	12.704	12.698	12.721	12.708	12.708	12.718	12.712
R	18	WP 7	12.727	12.726	12.721	12.723	12.743	12.730	12.726	12.740	12.755
R	36	WP 8	12.765	12.766	12.762	12.753	12.778	12.766	12.762	12.791	12.773
R	54	WP 9	12.799	12.789	12.776	12.647	12.414	12.235	12.012	11.760	11.674
R	72	WP 10	12.820	12.636	12.425	12.114	11.922	11.658	11.047	10.712	10.450
R	90	WP 11	12.834	12.810	12.776	12.594	12.609	12.442	11.800	11.443	11.014
R	108	WP 52	12.815	12.817	12.819	12.817	12.890	12.831	12.820	12.796	12.548
R	126	WP 53	12.826	12.825	12.828	12.827	12.816	12.823	12.829	12.832	12.828
R	144	WP 54	12.829	12.826	12.832	12.827	12.818	12.825	12.832	12.830	12.830
R	162	WP 55	12.827	12.825	12.826	12.827	12.812	12.823	12.827	12.820	12.818
R	180	WP 56	12.820	12.816	12.821	12.824	12.805	12.816	12.820	12.807	12.810
R	198	WP 57	12.813	12.811	12.817	12.815	12.800	12.811	12.815	12.799	12.803
R	216	WP 58	12.804	12.799	12.802	12.805	12.783	12.792	12.794	12.778	12.780
R	234	WP 59	12.786	12.783	12.785	12.793	12.773	12.782	12.782	12.762	12.769
R	252	WP 60	12.748	12.745	12.746	12.757	12.741	12.756	12.743	12.726	12.730
R	270	WP 1	12.697	12.703	12.702	12.706	12.754	12.723	12.710	12.691	12.714
R	288	WP 2	12.679	12.679	12.673	12.679	12.776	12.692	12.675	12.653	12.676
R	306	WP 3	12.677	12.597	12.545	12.520	12.432	12.347	12.238	12.105	12.072
R	324	WP 4	12.678	12.642	12.540	12.402	12.343	12.318	11.962	11.839	11.700
R	342	WP 5	12.684	12.689	12.683	12.641	12.698	12.652	12.558	12.599	12.546

Table B.5. CMM radius measurements for bar AA2 for given intervals of wear.

			Radius Measurement (mm)								
Location	**Angle**	**CMM Code**	**Initial**	**50 km**	**100 km**	**150 km**	**200 km**	**250 km**	**300 km**	**350 km**	**400 km**
C	0	WP 17	12.728	12.726	12.724	12.722	12.740	12.725	12.718	12.726	12.724
C	18	WP 16	12.729	12.730	12.729	12.718	12.739	12.726	12.725	12.731	12.729
C	36	WP 15	12.737	12.737	12.737	12.712	12.745	12.734	12.729	12.743	12.735
C	54	WP 14	12.736	12.733	12.689	12.737	12.449	12.464	12.422	12.424	12.177
C	72	WP 13	12.746	12.437	12.210	12.028	11.669	11.465	11.409	11.396	11.065
C	90	WP 12	12.747	12.709	12.665	12.303	12.421	12.168	12.021	11.847	11.502
C	108	WP 51	12.732	12.735	12.732	12.712	12.776	12.745	12.736	12.743	12.591
C	126	WP 50	12.736	12.735	12.741	12.734	12.727	12.736	12.738	12.747	12.742
C	144	WP 49	12.734	12.731	12.733	12.735	12.722	12.729	12.738	12.739	12.736
C	162	WP 48	12.745	12.742	12.743	12.746	12.732	12.746	12.749	12.745	12.746
C	180	WP 47	12.751	12.750	12.753	12.754	12.737	12.754	12.758	12.749	12.749
C	198	WP 46	12.761	12.760	12.759	12.763	12.748	12.760	12.762	12.753	12.752
C	216	WP 45	12.767	12.764	12.763	12.767	12.757	12.764	12.768	12.753	12.755
C	234	WP 44	12.759	12.749	12.753	12.766	12.744	12.753	12.752	12.738	12.742
C	252	WP 43	12.766	12.749	12.750	12.758	12.751	12.765	12.750	12.737	12.741
C	270	WP 22	12.720	12.723	12.721	12.728	12.810	12.752	12.727	12.720	12.722
C	288	WP 21	12.723	12.719	12.716	12.724	12.775	12.722	12.699	12.629	12.585
C	306	WP 20	12.714	12.637	12.551	12.594	12.399	12.250	12.121	11.787	11.577
C	324	WP 19	12.716	12.569	12.441	12.374	12.286	12.063	11.969	11.656	11.459
C	342	WP 18	12.726	12.724	12.723	12.700	12.737	12.722	12.717	12.693	12.614
L	0	WP 28	12.727	12.726	12.725	12.726	12.739	12.729	12.721	12.727	12.725
L	18	WP 29	12.728	12.728	12.729	12.723	12.737	12.725	12.720	12.730	12.727
L	36	WP 30	12.737	12.735	12.737	12.732	12.741	12.734	12.731	12.742	12.738
L	54	WP 31	12.740	12.690	12.644	12.738	12.497	12.363	12.145	12.125	11.993
L	72	WP 32	12.743	12.480	12.273	12.282	11.943	11.657	11.322	11.213	10.796
L	90	WP 33	12.739	12.704	12.664	12.489	12.549	12.314	12.026	11.909	11.222
L	108	WP 34	12.738	12.739	12.736	12.721	12.772	12.745	12.736	12.747	12.510
L	126	WP 35	12.734	12.735	12.734	12.735	12.723	12.732	12.736	12.743	12.738
L	144	WP 36	12.732	12.730	12.728	12.734	12.721	12.728	12.733	12.740	12.733
L	162	WP 37	12.746	12.745	12.745	12.743	12.730	12.744	12.745	12.744	12.742
L	180	WP 38	12.749	12.750	12.749	12.754	12.738	12.749	12.753	12.748	12.746
L	198	WP 39	12.762	12.760	12.759	12.764	12.750	12.761	12.762	12.754	12.754
L	216	WP 40	12.765	12.763	12.764	12.767	12.757	12.764	12.768	12.753	12.753
L	234	WP 41	12.758	12.753	12.743	12.767	12.748	12.754	12.753	12.739	12.746
L	252	WP 42	12.757	12.754	12.754	12.760	12.756	12.767	12.754	12.741	12.743
L	270	WP 23	12.725	12.727	12.729	12.731	12.810	12.756	12.733	12.725	12.728
L	288	WP 24	12.723	12.722	12.721	12.731	12.773	12.726	12.702	12.601	12.527
L	306	WP 25	12.722	12.648	12.587	12.601	12.401	12.278	12.093	11.749	11.491
L	324	WP 26	12.721	12.533	12.534	12.461	12.289	12.169	11.962	11.664	11.409
L	342	WP 27	12.731	12.728	12.726	12.590	12.736	12.722	12.719	12.723	12.711
R	0	WP 6	12.719	12.722	12.720	12.719	12.734	12.718	12.712	12.723	12.728
R	18	WP 7	12.724	12.723	12.721	12.716	12.725	12.721	12.716	12.728	12.726
R	36	WP 8	12.737	12.736	12.735	12.728	12.741	12.730	12.728	12.742	12.735
R	54	WP 9	12.739	12.463	12.461	12.738	12.140	12.021	11.863	11.701	11.385
R	72	WP 10	12.755	12.425	12.377	12.037	11.781	11.475	11.217	10.904	10.431
R	90	WP 11	12.746	12.716	12.696	12.361	12.533	12.206	12.085	11.783	11.162
R	108	WP 52	12.738	12.741	12.742	12.719	12.777	12.745	12.741	12.753	12.621
R	126	WP 53	12.741	12.741	12.742	12.739	12.732	12.740	12.746	12.751	12.747
R	144	WP 54	12.734	12.738	12.737	12.743	12.728	12.738	12.742	12.744	12.743
R	162	WP 55	12.749	12.750	12.750	12.751	12.737	12.751	12.755	12.748	12.750
R	180	WP 56	12.755	12.752	12.755	12.762	12.740	12.759	12.760	12.751	12.749
R	198	WP 57	12.761	12.759	12.755	12.774	12.751	12.761	12.766	12.754	12.755
R	216	WP 58	12.768	12.758	12.759	12.765	12.753	12.762	12.767	12.750	12.754
R	234	WP 59	12.751	12.746	12.745	12.762	12.742	12.751	12.748	12.731	12.736
R	252	WP 60	12.748	12.745	12.745	12.754	12.746	12.757	12.745	12.729	12.735
R	270	WP 1	12.719	12.722	12.721	12.723	12.792	12.754	12.725	12.713	12.731
R	288	WP 2	12.705	12.709	12.705	12.721	12.756	12.712	12.725	12.660	12.647
R	306	WP 3	12.710	12.631	12.515	12.566	12.346	12.239	12.123	11.989	11.798
R	324	WP 4	12.714	12.560	12.556	12.316	12.237	12.043	11.919	11.776	11.561
R	342	WP 5	12.699	12.717	12.715	12.563	12.701	12.651	12.649	12.655	12.585

Table B.6. CMM radius measurements for bar AA3 for given intervals of wear.

			Radius Measurement (mm)								
Location	**Angle**	**CMM Code**	**Initial**	**50 km**	**100 km**	**150 km**	**200 km**	**250 km**	**300 km**	**350 km**	**400 km**
C	0	WP 17	12.704	12.709	12.710	12.704	12.733	12.720	12.709	12.719	12.716
C	18	WP 16	12.703	12.701	12.703	12.702	12.720	12.711	12.703	12.710	12.710
C	36	WP 15	12.699	12.699	12.699	12.693	12.711	12.705	12.695	12.708	12.705
C	54	WP 14	12.700	12.700	12.699	12.691	12.700	12.689	12.681	12.551	11.818
C	72	WP 13	12.711	12.713	12.717	12.447	12.144	12.003	11.997	11.365	10.456
C	90	WP 12	12.736	12.732	12.730	12.594	12.578	12.412	12.399	11.749	10.738
C	108	WP 51	12.710	12.707	12.709	12.687	12.724	12.712	12.709	12.698	11.955
C	126	WP 50	12.734	12.732	12.731	12.714	12.720	12.725	12.728	12.734	12.732
C	144	WP 49	12.735	12.735	12.736	12.732	12.720	12.726	12.734	12.738	12.734
C	162	WP 48	12.764	12.760	12.762	12.751	12.740	12.752	12.757	12.756	12.752
C	180	WP 47	12.779	12.777	12.778	12.777	12.756	12.765	12.771	12.767	12.762
C	198	WP 46	12.794	12.784	12.787	12.789	12.764	12.776	12.783	12.774	12.771
C	216	WP 45	12.797	12.794	12.792	12.796	12.778	12.785	12.790	12.779	12.778
C	234	WP 44	12.795	12.792	12.793	12.804	12.781	12.785	12.791	12.780	12.780
C	252	WP 43	12.789	12.785	12.793	12.793	12.779	12.787	12.784	12.775	12.774
C	270	WP 22	12.747	12.753	12.752	12.760	12.834	12.786	12.757	12.748	12.751
C	288	WP 21	12.737	12.743	12.742	12.750	12.778	12.742	12.735	12.704	12.673
C	306	WP 20	12.723	12.719	12.650	12.652	12.440	12.330	12.309	12.010	11.720
C	324	WP 19	12.712	12.671	12.534	12.373	12.192	12.072	12.060	11.805	11.553
C	342	WP 18	12.708	12.712	12.712	12.640	12.697	12.687	12.683	12.661	12.643
L	0	WP 28	12.698	12.702	12.700	12.731	12.721	12.713	12.705	12.711	12.710
L	18	WP 29	12.695	12.698	12.700	12.698	12.715	12.708	12.699	12.705	12.709
L	36	WP 30	12.696	12.699	12.699	12.690	12.710	12.702	12.694	12.705	12.704
L	54	WP 31	12.701	12.700	12.700	12.696	12.482	12.290	12.282	11.835	11.399
L	72	WP 32	12.716	12.717	12.717	12.386	12.048	11.719	11.711	10.894	9.977
L	90	WP 33	12.736	12.738	12.735	12.572	12.587	12.340	12.325	11.404	10.276
L	108	WP 34	12.715	12.718	12.719	12.713	12.736	12.721	12.714	12.620	11.604
L	126	WP 35	12.741	12.739	12.738	12.726	12.726	12.734	12.736	12.742	12.740
L	144	WP 36	12.746	12.743	12.750	12.744	12.725	12.736	12.740	12.742	12.738
L	162	WP 37	12.770	12.770	12.767	12.760	12.754	12.765	12.767	12.763	12.761
L	180	WP 38	12.776	12.781	12.779	12.778	12.756	12.767	12.773	12.768	12.766
L	198	WP 39	12.788	12.785	12.786	12.790	12.767	12.777	12.782	12.773	12.772
L	216	WP 40	12.790	12.791	12.792	12.799	12.778	12.786	12.786	12.778	12.777
L	234	WP 41	12.793	12.792	12.792	12.798	12.778	12.784	12.789	12.777	12.778
L	252	WP 42	12.783	12.788	12.787	12.788	12.778	12.784	12.779	12.768	12.771
L	270	WP 23	12.744	12.745	12.748	12.754	12.827	12.776	12.751	12.742	12.746
L	288	WP 24	12.731	12.735	12.733	12.745	12.758	12.724	12.716	12.655	12.485
L	306	WP 25	12.714	12.685	12.607	12.610	12.322	12.104	12.083	11.778	11.321
L	324	WP 26	12.703	12.680	12.582	12.352	12.166	11.904	11.901	11.638	11.323
L	342	WP 27	12.699	12.703	12.702	12.682	12.726	12.715	12.707	12.706	12.704
R	0	WP 6	12.708	12.710	12.711	12.704	12.731	12.742	12.713	12.718	12.720
R	18	WP 7	12.700	12.703	12.703	12.703	12.721	12.714	12.704	12.711	12.715
R	36	WP 8	12.698	12.699	12.697	12.693	12.714	12.705	12.697	12.705	12.707
R	54	WP 9	12.715	12.697	12.698	12.696	12.541	12.489	12.471	11.910	11.523
R	72	WP 10	12.711	12.712	12.699	12.433	12.015	11.766	11.760	11.110	10.413
R	90	WP 11	12.732	12.731	12.726	12.596	12.576	12.390	12.371	11.815	10.864
R	108	WP 52	12.708	12.704	12.707	12.700	12.713	12.707	12.706	12.716	12.272
R	126	WP 53	12.731	12.733	12.727	12.718	12.715	12.723	12.727	12.729	12.726
R	144	WP 54	12.734	12.730	12.734	12.731	12.714	12.724	12.730	12.731	12.730
R	162	WP 55	12.759	12.759	12.760	12.751	12.737	12.747	12.757	12.752	12.750
R	180	WP 56	12.774	12.772	12.770	12.777	12.749	12.762	12.766	12.763	12.759
R	198	WP 57	12.788	12.783	12.784	12.789	12.762	12.772	12.779	12.769	12.770
R	216	WP 58	12.796	12.789	12.791	12.798	12.773	12.781	12.788	12.778	12.776
R	234	WP 59	12.795	12.792	12.772	12.801	12.780	12.790	12.789	12.778	12.779
R	252	WP 60	12.788	12.789	12.795	12.793	12.781	12.787	12.785	12.773	12.774
R	270	WP 1	12.755	12.756	12.754	12.766	12.829	12.790	12.755	12.751	12.751
R	288	WP 2	12.740	12.744	12.745	12.754	12.785	12.749	12.742	12.717	12.706
R	306	WP 3	12.726	12.728	12.673	12.719	12.509	12.434	12.414	12.128	11.921
R	324	WP 4	12.714	12.720	12.609	12.513	12.404	12.265	12.259	11.980	11.783
R	342	WP 5	12.712	12.714	12.712	12.713	12.737	12.688	12.683	12.689	12.663

Appendix C
EDEM simulated force and velocity data

The following tables are taken from the data obtained from the EDEM simulations. The 20 data points taken for each simulation are summarized into a single average for force and velocity at each of the segments of the bar.

Table C.1. Average simulation predicted force (N) and simulation predicted relative velocity (m/s) for bar AA1.

Segment	Initial		50 km		100 km		150 km	
	Force	Velocity	Force	Velocity	Force	Velocity	Force	Velocity
0	0	0	0	0	0	0	0	0
18	0	0	0	0	0	0	0	0
36	0.1157	0.6969	0.0478	0.8625	0.0949	0.8029	0.1020	0.8424
54	0.1257	0.8667	0.0851	0.9707	0.0805	0.8305	0.0579	0.9176
72	0.0231	0.8879	0.0476	1.0781	0.0599	1.1427	0.0352	1.1617
90	0.0008	0.8344	0.0031	0.9956	0.0090	1.0581	0.0258	1.1203
270	0	0	0	0.1515	0	0	0	0
288	0	0.1733	0	0.1515	0	0.0491	0.0000	0.1237
306	0.0021	0.8893	0.0007	0.7550	0.0007	0.8861	0.0015	1.0858
324	0.0462	0.9354	0.0378	0.9483	0.0438	1.0151	0.0455	1.0383
342	0.0332	0.7058	0.0308	0.8441	0.0243	0.9404	0.0320	0.9629

Segment	200 km		250 km		300 km		350 km	
	Force	Velocity	Force	Velocity	Force	Velocity	Force	Velocity
0	0	0	0	0	0	0	0	0
18	0	0	0	0	0	0	0	0
36	0.0735	0.7304	0.7456	0.8950	0.0844	1.0131	0.0718	0.7881
54	0.0743	0.9782	0.7977	0.8560	0.0702	0.9814	0.0693	0.9039
72	0.0445	1.0637	0.9890	0.9081	0.0142	1.2307	0.0295	1.1202
90	0.0265	1.1458	0.8429	0.8614	0.0398	1.1655	0.0747	1.2846
270	0	0	0	0	0	0	0	0
288	0.0000	0.3439	0.6769	0.4572	0.0000	0.6195	0.0006	0.9280
306	0.0063	1.0052	1.0409	1.1230	0.0254	1.0882	0.0304	1.1819
324	0.0281	1.1030	0.7664	1.0331	0.0342	0.9855	0.0235	1.1740
342	0.0215	1.0028	0.7460	1.0311	0.0162	0.9854	0.0193	0.9754

Table C.2. Average simulation predicted force (N) and simulation predicted relative velocity (m/s) for bar AA2.

Segment	Initial		50 km		100 km		150 km	
	Force	Velocity	Force	Velocity	Force	Velocity	Force	Velocity
0	0	0	0	0	0	0	0	0
18	0	0	0	0	0	0	0	0
36	0.1157	0.6969	0.0839	0.8945	0.0817	0.7105	0.1013	0.7734
54	0.1257	0.8667	0.1020	0.8532	0.0920	0.8661	0.0843	0.8945
72	0.0231	0.8879	0.0747	1.0287	0.0643	1.0869	0.0420	1.1919
90	0.0008	0.8344	0.0051	1.0989	0.0111	0.9171	0.0071	1.0808
270	0	0	0	0	0	0	0	0
288	0	0.1733	0	0.0706	0	0.1729	0	0.1527
306	0.0021	0.8893	0.0025	0.8445	0.0024	0.8874	0.0026	0.8941
324	0.0462	0.9354	0.0516	1.0600	0.0333	1.0184	0.0508	0.9983
342	0.0332	0.7058	0.0275	1.0593	0.0291	0.9828	0.0250	1.0007

Segment	200 km		250 km		300 km		350 km	
	Force	Velocity	Force	Velocity	Force	Velocity	Force	Velocity
0	0	0	0	0	0	0	0	0
18	0	0	0	0	0	0	0	0
36	0.0731	0.7988	0.0909	0.8181	0.0774	0.8609	0.1015	1.0490
54	0.0748	0.9157	0.0565	0.9716	0.0616	0.8100	0.0487	0.9348
72	0.0467	1.0751	0.0229	1.0703	0.0653	1.0675	0.0435	1.1857
90	0.0171	1.0042	0.0441	1.1647	0.0243	1.1091	0.0454	1.3136
270	0	0	0	0	0	0	0	0.0375
288	0.0000	0.2383	0.0006	0.3179	0.0007	0.4869	0.0015	0.8756
306	0.0020	0.9222	0.0048	1.0767	0.0178	1.1596	0.0218	1.0604
324	0.0471	1.1013	0.0450	1.1565	0.0203	1.0669	0.0300	1.0928
342	0.0416	0.9874	0.0277	1.0050	0.0278	1.0085	0.0142	0.9466

Table C.3. Average simulation predicted force (N) and simulation predicted relative velocity (m/s) for bar AA3.

Segment	Initial		50 km		100 km		150 km	
	Force	Velocity	Force	Velocity	Force	Velocity	Force	Velocity
0	0	0	0	0	0	0	0	0
18	0	0	0	0	0	0	0	0
36	0.1157	0.6969	0.0559	0.8352	0.0931	0.9708	0.0703	0.8590
54	0.1257	0.8667	0.1160	0.8740	0.0977	0.9349	0.0938	0.9304
72	0.0231	0.8879	0.0036	0.8802	0.0230	1.1769	0.0188	1.1975
90	0.0008	0.8344	0.0036	0.8802	0.0049	0.9304	0.0081	1.1104
270	0	0	0	0	0	0	0	0
288	0	0.1733	0	0.0847	0	0.0605	0	0.0780
306	0.0021	0.8893	0.0022	0.7727	0.0019	0.8182	0.0017	1.0080
324	0.0462	0.9354	0.0364	1.0430	0.0247	1.0321	0.0531	1.1228
342	0.0332	0.7058	0.0508	0.9899	0.0294	1.0293	0.0371	1.0842

Segment	200 km		250 km		300 km		350 km	
	Force	Velocity	Force	Velocity	Force	Velocity	Force	Velocity
0	0	0	0	0	0	0	0	0
18	0	0	0	0	0	0	0	0
36	0.0845	0.8904	0.0812	0.6836	0.0989	0.8465	0.0950	1.0054
54	0.0912	0.8856	0.0758	0.8119	0.1041	0.9062	0.0698	0.8764
72	0.0423	1.0963	0.0494	0.9271	0.0567	1.1049	0.0315	1.0627
90	0.0184	1.0291	0.0248	0.9453	0.0180	1.0754	0.0598	1.2309
270	0	0	0	0	0	0	0	0
288	0	0.2381	0.0000	0.2074	0	0.2489	0.0001	0.8212
306	0.0063	1.0708	0.0052	1.0689	0.0117	1.0604	0.0163	1.1015
324	0.0491	1.1729	0.0320	1.0019	0.0224	1.0260	0.0206	1.0325
342	0.0199	1.0777	0.0202	0.9349	0.0182	0.9537	0.0154	0.9698

Appendix D
Attempted models and equation fitting output

Linear Models

The initial linear model is described in Section 5.3.1 (Figure 5.16)

The second attempt at a linear model ($W = kFv$) excluded data from the 36 and 342-degree segments.

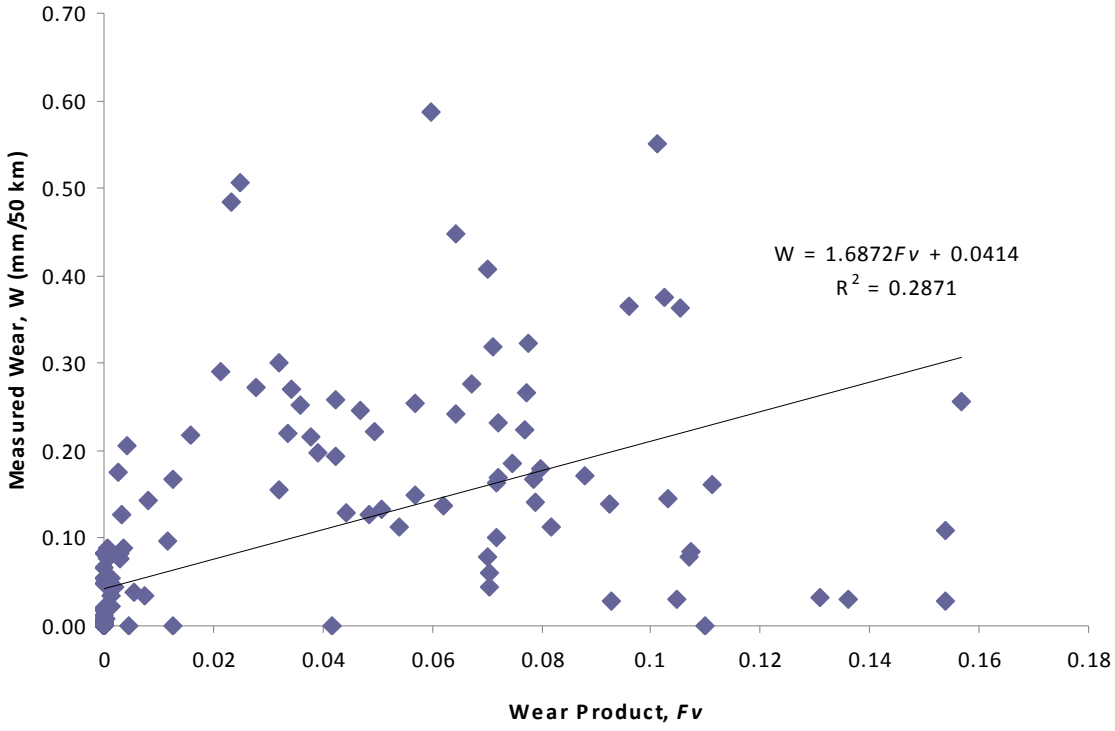

Figure D.1. Regression of wear product (Fv) and measured wear, W, excluding 36 and 342-degree segment data.

Non-Linear Models

The initial attempt at a non-linear model (also excluding 36 and 342-degree segment data) is described in Section 5.3.1 (Figure 5.17). The following is the output from SAS which determined the coefficients in the non-linear equation ($W = kF^b v^c$).

```
The SAS System                          13:04 Wednesday, November 18, 2009   1

The NLIN Procedure
Dependent Variable wear
Method: Gauss-Newton

                  Iterative Phase
                                                    Sum of
 Iter           k           b           c          Squares

    0      1.0000      1.0000      1.0000           8.2144
    1      0.0558      0.2678      1.2037           2.8595
    2      0.0719      0.0489      3.0481           1.6131
    3      0.0853      0.1205      2.6655           1.0517
    4      0.0996      0.1533      2.4220           1.0248
    5      0.1050      0.1557      2.3439           1.0242
    6      0.1058      0.1562      2.3345           1.0242
    7      0.1059      0.1563      2.3331           1.0242
    8      0.1059      0.1563      2.3329           1.0242

NOTE: Convergence criterion met.

         Estimation Summary

Method                     Gauss-Newton
Iterations                            8
Subiterations                         1
Average Subiterations             0.125
R                              7.531E-6
PPC(k)                         0.000018
RPC(k)                         0.000129
Object                         3.198E-9
Objective                      1.024207
Observations Read                   144
Observations Used                    89
Observations Missing                 55

NOTE: An intercept was not specified for this model.

                                  Sum of        Mean                Approx
Source                      DF    Squares      Square    F Value    Pr > F

Model                        3     2.9986      0.9995      83.93    <.0001
Error                       86     1.0242      0.0119
Uncorrected Total           89     4.0228
```

Parameter	Estimate	Approx Std Error	Approximate 95% Confidence Limits	
k	0.1059	0.0287	0.0489	0.1630
b	0.1563	0.0436	0.0696	0.2430
c	2.3329	0.4788	1.3810	3.2847

Approximate Correlation Matrix

	k	b	c
k	1.0000000	0.3854380	-0.8458048
b	0.3854380	1.0000000	0.1085819
c	-0.8458048	0.1085819	1.0000000

The second attempt at the non-linear model and all subsequent models were performed on bar AA1 and bar AA2 was used for verification. As described in Section 5.3.1 (Figure 5.18), the model was much improved. The following is the output from SAS for the non-linear equation ($W = kF^b v^c$) for bar AA1.

The SAS System 13:04 Wednesday, November 18, 2009 1

The NLIN Procedure
Dependent Variable wear
Method: Gauss-Newton

Iterative Phase

Iter	k	b	c	Sum of Squares
0	1.0000	1.0000	1.0000	7.1041
1	0.1314	0.3278	1.0413	1.1418
2	0.1317	0.1510	1.5390	0.6699
3	0.1265	0.1580	1.9537	0.6387
4	0.1300	0.1514	1.8702	0.6384
5	0.1288	0.1528	1.8987	0.6384
6	0.1291	0.1523	1.8909	0.6384
7	0.1290	0.1525	1.8933	0.6384
8	0.1290	0.1524	1.8926	0.6384
9	0.1290	0.1524	1.8928	0.6384
10	0.1290	0.1524	1.8928	0.6384

NOTE: Convergence criterion met.

Estimation Summary

Method	Gauss-Newton
Iterations	10
Subiterations	1
Average Subiterations	0.1
R	4.582E-6
PPC(c)	0.000011
RPC(c)	0.000035
Object	1.61E-10
Objective	0.638388
Observations Read	72
Observations Used	45
Observations Missing	27

NOTE: An intercept was not specified for this model.

Source	DF	Sum of Squares	Mean Square	F Value	Approx Pr > F
Model	3	1.5853	0.5284	34.77	<.0001
Error	42	0.6384	0.0152		
Uncorrected Total	45	2.2237			

Parameter	Estimate	Approx Std Error	Approximate 95% Confidence Limits	
k	0.1290	0.0520	0.0241	0.2339
b	0.1524	0.0576	0.0362	0.2687
c	1.8928	0.8055	0.2671	3.5184

Approximate Correlation Matrix

	k	b	c
k	1.0000000	0.2092608	-0.8987361
b	0.2092608	1.0000000	0.1675437
c	-0.8987361	0.1675437	1.0000000

The next attempt at improving the non-linear model was to include an intercept ($W = kF^b v^c + y$).

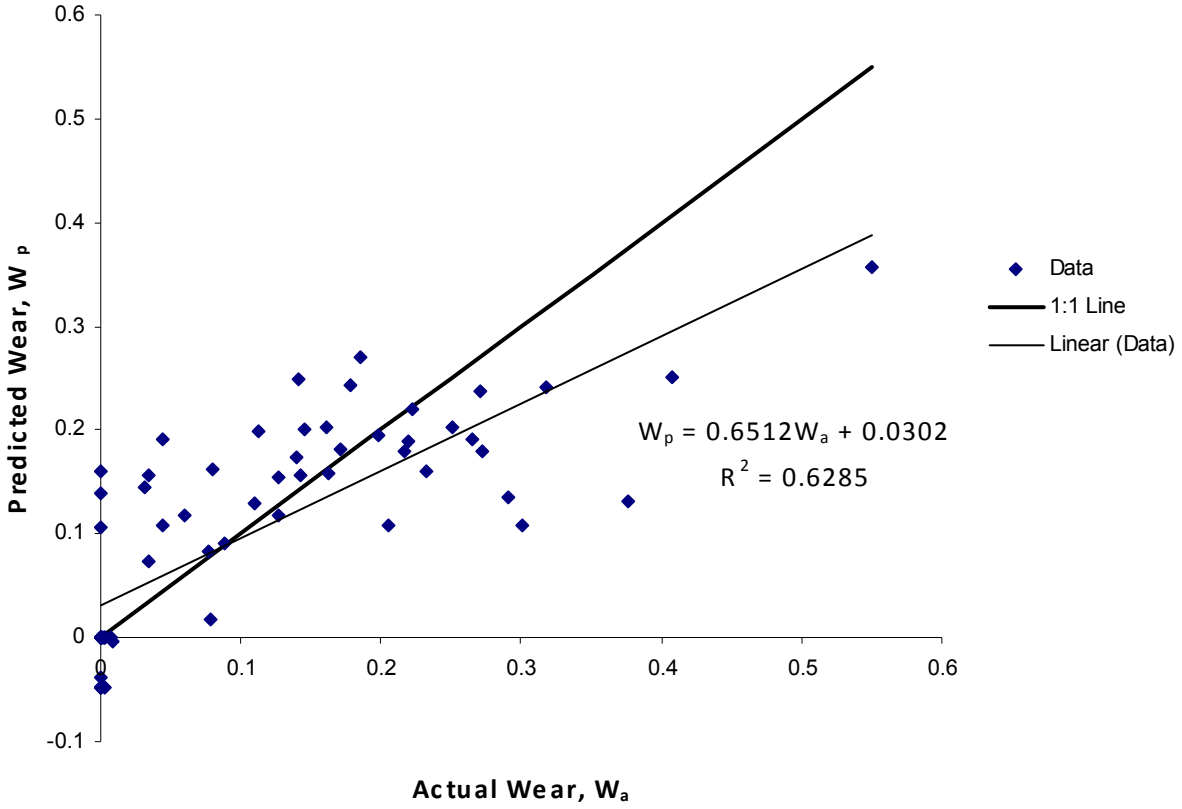

Figure D.2. Correlation of predicted wear, W_p, and actual wear, W_a, with inclusion of intercept in the non-linear model.

The following is the SAS output to determine the coefficients in the non-linear model with intercept ($W = kF^b v^c + y$).

The NLIN Procedure
Dependent Variable wear
Method: Gauss-Newton

Iterative Phase

Iter	k	b	c	y	Sum of Squares
0	1.0000	1.0000	1.0000	0	7.1041
1	0.1053	0.7320	1.0142	0.1045	0.8718
2	0.1070	0.2906	1.1582	0.0955	0.7393
3	0.1228	0.1719	1.3910	0.0582	0.6838
4	0.1607	0.1153	1.5322	-0.0169	0.6504
5	0.1676	0.1251	1.6038	-0.0426	0.6333
6	0.1743	0.1221	1.5494	-0.0494	0.6332
7	0.1713	0.1240	1.5770	-0.0469	0.6332
8	0.1730	0.1230	1.5620	-0.0483	0.6332
9	0.1721	0.1236	1.5702	-0.0476	0.6331
10	0.1726	0.1233	1.5658	-0.0480	0.6331
11	0.1723	0.1234	1.5682	-0.0478	0.6331
12	0.1725	0.1233	1.5669	-0.0479	0.6331
13	0.1724	0.1234	1.5676	-0.0478	0.6331
14	0.1724	0.1234	1.5672	-0.0479	0.6331
15	0.1724	0.1234	1.5674	-0.0478	0.6331
16	0.1724	0.1234	1.5673	-0.0478	0.6331
17	0.1724	0.1234	1.5674	-0.0478	0.6331

NOTE: Convergence criterion met.

Estimation Summary

Method	Gauss-Newton
Iterations	17
Subiterations	1
Average Subiterations	0.058824
R	5.683E-6
PPC(y)	0.000066
RPC(y)	0.00012
Object	4.96E-11
Objective	0.63315
Observations Read	49
Observations Used	45
Observations Missing	4

Source	DF	Sum of Squares	Mean Square	F Value	Approx Pr > F
Model	3	0.2918	0.0973	6.30	0.0013
Error	41	0.6331	0.0154		
Corrected Total	44	0.9250			

Parameter	Estimate	Approx Std Error	Approximate 95% Confidence Limits	
k	0.1724	0.1185	-0.0669	0.4117
b	0.1234	0.0748	-0.0278	0.2745
c	1.5674	0.9891	-0.4301	3.5648
y	-0.0478	0.1025	-0.2549	0.1592

Approximate Correlation Matrix

	k	b	c	y
k	1.0000000	-0.6287516	-0.9422994	-0.8855374
b	-0.6287516	1.0000000	0.6626427	0.7915281
c	-0.9422994	0.6626427	1.0000000	0.7638800
y	-0.8855374	0.7915281	0.7638800	1.0000000

Another analysis was performed on a limited selection of data that would be assumed unaffected by the dynamic processes occurring around the soil wedge; in particular, excluding the data for the 54-degree segment.

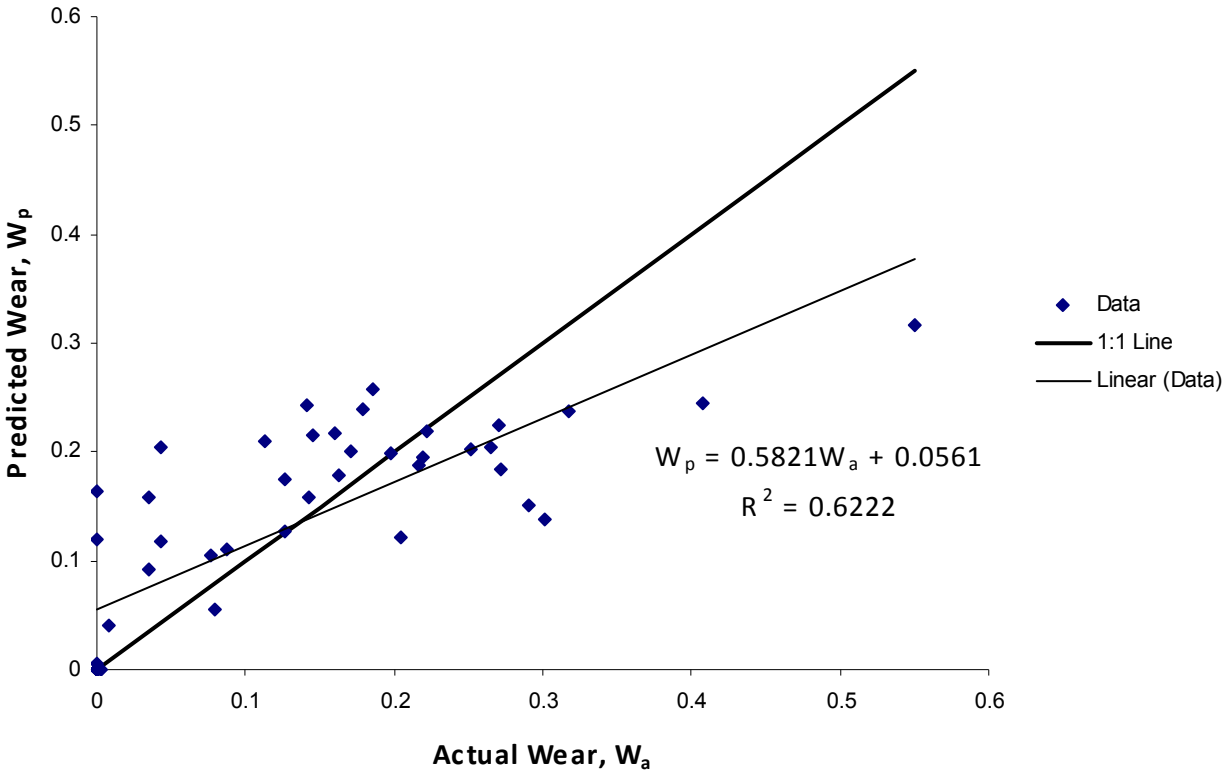

Figure D.3. Correlation of predicted wear, W_p, and actual wear, W_a, excluding also 54-degree segment data from the non-linear model.

The following is the output from SAS for the non-linear equation ($W = kF^b v^c$) without 54-degree segment data.

```
The SAS System                          11:42 Monday, November 23, 2009   1

The NLIN Procedure
Dependent Variable wear
Method: Gauss-Newton

                  Iterative Phase
                                                    Sum of
 Iter           k           b           c          Squares

    0      1.0000      1.0000      1.0000           6.2434
    1      0.1610      0.1289      0.9646           0.5818
    2      0.1739      0.1717      1.5488           0.5223
    3      0.1869      0.1529      1.2409           0.5187
    4      0.1804      0.1588      1.3459           0.5184
    5      0.1826      0.1567      1.3114           0.5184
    6      0.1819      0.1574      1.3233           0.5184
    7      0.1821      0.1572      1.3192           0.5184
    8      0.1820      0.1573      1.3206           0.5184
    9      0.1820      0.1573      1.3201           0.5184
   10      0.1820      0.1573      1.3203           0.5184
   11      0.1820      0.1573      1.3202           0.5184

NOTE: Convergence criterion met.

         Estimation Summary

Method                  Gauss-Newton
Iterations                        11
R                           4.688E-6
PPC(c)                      0.000014
RPC(c)                      0.000041
Object                      1.26E-10
Objective                   0.518378
Observations Read                 48
Observations Used                 37
Observations Missing              11

The NLIN Procedure

NOTE: An intercept was not specified for this model.

                                 Sum of        Mean                Approx
Source                     DF    Squares      Square    F Value    Pr > F

Model                       3     1.4751      0.4917      32.25    <.0001
Error                      34     0.5184      0.0152
Uncorrected Total          37     1.9934
```

Parameter	Estimate	Approx Std Error	Approximate 95% Confidence Limits	
k	0.1820	0.0758	0.0281	0.3360
b	0.1573	0.0552	0.0451	0.2694
c	1.3202	0.8176	-0.3412	2.9817

Approximate Correlation Matrix

	k	b	c
k	1.0000000	0.1976353	-0.9068717
b	0.1976353	1.0000000	0.1560662
c	-0.9068717	0.1560662	1.0000000

Finally, a model was created without the 54-degree segment data and with an intercept included in the non-linear model ($W = kF^b v^c + y$).

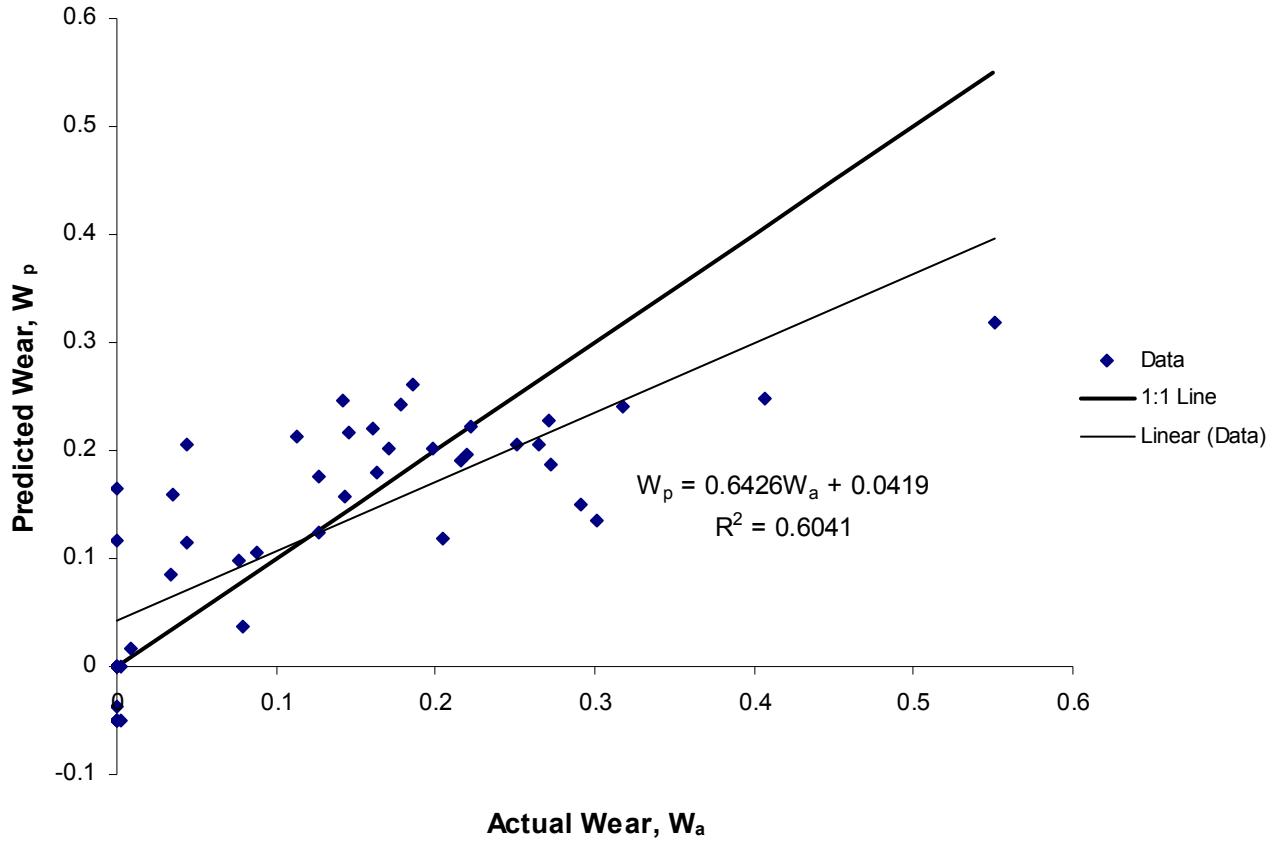

Figure D.4. Correlation of predicted wear, Wp, and actual wear, Wa, excluding also 54-degree segment data from the non-linear model with intercept.

The following is the output from SAS for the non-linear model with intercept for bar AA1 without 54-degree segment data.

The SAS System 11:42 Monday, November 23, 2009 1

The NLIN Procedure
Dependent Variable wear
Method: Gauss-Newton

Iterative Phase

Iter	k	b	c	y	Sum of Squares
0	1.0000	1.0000	1.0000	0	6.2434
1	0.1280	0.5103	0.9585	0.0926	0.7142
2	0.1490	0.2147	0.8278	0.0738	0.5772
3	0.1768	0.1531	0.9169	0.0350	0.5418
4	0.2167	0.1247	1.0740	-0.0261	0.5186
5	0.2289	0.1277	1.0987	-0.0476	0.5136
6	0.2324	0.1264	1.0828	-0.0511	0.5136
7	0.2311	0.1271	1.0912	-0.0502	0.5136
8	0.2319	0.1267	1.0866	-0.0507	0.5136
9	0.2315	0.1269	1.0891	-0.0504	0.5136
10	0.2317	0.1268	1.0878	-0.0506	0.5136
11	0.2316	0.1269	1.0885	-0.0505	0.5136
12	0.2316	0.1268	1.0881	-0.0505	0.5136
13	0.2316	0.1268	1.0883	-0.0505	0.5136
14	0.2316	0.1268	1.0882	-0.0505	0.5136
15	0.2316	0.1268	1.0883	-0.0505	0.5136

Estimation Summary

Method	Gauss-Newton
Iterations	15
Subiterations	1
Average Subiterations	0.066667
R	7.819E-6
PPC(y)	0.000086
RPC(y)	0.000156
Object	9.2E-11
Objective	0.51361
Observations Read	41
Observations Used	37
Observations Missing	4

Source	DF	Sum of Squares	Mean Square	F Value	Approx Pr > F
Model	3	0.2774	0.0925	5.94	0.0023
Error	33	0.5136	0.0156		
Corrected Total	36	0.7910			

Parameter	Estimate	Approx Std Error	Approximate 95% Confidence Limits	
k	0.2316	0.1500	-0.0736	0.5368
b	0.1268	0.0787	-0.0332	0.2869
c	1.0883	0.9001	-0.7430	2.9195
y	-0.0505	0.1151	-0.2848	0.1837

Approximate Correlation Matrix

	k	b	c	y
k	1.0000000	-0.6359378	-0.9275871	-0.8563035
b	-0.6359378	1.0000000	0.6211673	0.8316128
c	-0.9275871	0.6211673	1.0000000	0.6939047
y	-0.8563035	0.8316128	0.6939047	1.0000000